INTERPRETING THE 3D ORIENTATION OF VASCULAR CANALS IN CORTICAL BONE IN BIRDS AND BATS

A Thesis Submitted to the College of

Graduate and Postdoctoral Studies

In Partial Fulfillment of the Requirements

For the Degree of Doctor of Philosophy

In the Department of Anatomy & Cell Biology

University of Saskatchewan

Saskatoon

By

ISAAC PRATT

Permission to use

In presenting this thesis/dissertation in partial fulfillment of the requirements for a Postgraduate degree from the University of Saskatchewan, I agree that the Libraries of this University may make it freely available for inspection. I further agree that permission for copying of this thesis/dissertation in any manner, in whole or in part, for scholarly purposes may be granted by the professor or professors who supervised my thesis/dissertation work or, in their absence, by the Head of the Department or the Dean of the College in which my thesis work was done. It is understood that any copying or publication or use of this thesis/dissertation or parts thereof for financial gain shall not be allowed without my written permission. It is also understood that due recognition shall be given to me and to the University of Saskatchewan in any scholarly use which may be made of any material in my thesis/dissertation.

Requests for permission to copy or to make other uses of materials in this thesis/dissertation in whole or part should be addressed to:

Head of the Department of Anatomy & Cell Biology
Health Sciences Building
107 Wiggins Rd
University of Saskatchewan
Saskatoon, Saskatchewan S7N 5E5
Canada

OR

Dean
College of Graduate and Postdoctoral Studies
University of Saskatchewan
116 Thorvaldson Building, 110 Science Place
Saskatoon, Saskatchewan, S7N 5C9
Canada

Abstract

Vascular canals in cortical bone during growth and development typically show an anisotropic pattern with canals falling into three main categories: circumferential, radial, and longitudinal. Two major hypotheses attempt to explain the preferred orientations in bone: that vascular canal orientation is optimized to resist a predominant strain direction from functional loading, or that it reflects growth requirements and velocity. This thesis presents a novel method to measure the three dimensional (3D) orientation of vascular canals. Image data are obtained from micro-CT scans and two angles are measured: phi, determining how longitudinal a canal is; and theta, determining whether a canal is radial or circumferential. This method offers a direct (3D) method for quantifying features of canal orientation and can be applied easily and non-destructively to multiple species and bones. This thesis describes two major studies to examine the orientation of vascular canals in birds and bats, the two extant groups of flying vertebrates. The first study examined the vascular canal network in the humerus and femur of a comparative sample of 31 bird and 24 bat species to look for a connection between canal orientation and functional loading. In addition to canal orientation several cross-sectional geometric parameters and strength indices were measured. The results indicated that the bat cortices are relatively thicker and poorly vascularized, whereas those of birds are thinner and more highly vascularized, and that bird bones have a greater resistance to torsional stress than the bats; in particular, the humerus in birds is more adapted to resist torsional stresses than the femur. Our results show that birds have a significantly higher laminarity index than bats. Counter to expectation, the birds had a significantly higher laminarity index in the femur than in the humerus. We conducted a comparison between our 3D method and an analogue to 2D histological measurements. This comparison revealed that 2D methods significantly underestimate the amount of longitudinal canals by an average of 20% and significantly overestimate the laminarity index by an average of 7.7%, systematically mis-estimating indices of vascular canal orientations. The second study was a controlled growth experiment using broiler chickens to investigate the effect of growth rate on vascular canal orientation. Using feed restriction we set up a fast growing control group and a slow growing restricted group. We found consistent patterns in the comparison between the humerus and the femur in both groups, with the humerus having higher laminar and longitudinal indices and a lower radial index than the femur. The faster growing group had higher radial indices and lower laminar and longitudinal indices in both the humerus and the femur than the restricted group. The higher radial indices in our control group point to a link between radial canals and faster growth, and laminar canals and slower growth, while the higher laminar indices in the humerus contradict the results of the first study and point to a link between circumferential canals and torsional loading. We believe this difference is due to differences in femoral loading between chickens and other birds. Overall our results indicate that the orientation of the cortical canal network in a bone is the consequence of a complex interaction between that bone's growth rate and functional loading environment.

Acknowledgments

I would like to first acknowledge and thank my supervisor Dr. David Cooper. Without his support and dedication this work would not have been possible. He provided an example of what a great researcher should be. I would also like to thank the other members of my advisory committee, Dr. J.D. Johnston, Dr. Ernie Walker, Dr. Gregg Adams, and Dr. Dean Chapman, for their support, advice, and for continually pushing me to make this project better.

I would also like to thank Kim Harrison, Dani Kabatoff, and Dr. Janna Andronowski and the beamline team at BMIT for assistance with beamtime, Brittney Lins for assistance with statistics and SPSS, and Centaine Raginski, Robert Gonda, Heather Barnett and Brandee Pastoor for assistance with animal husbandry. I would like to thank Dr. Ashton Reimer for assistance with figures in Chapter 2, and Dr. Janna Andronowski for providing feedback on the manuscript for Chapter 2.

Support for this research was provided by the Natural Sciences and Engineering Research Council (NSERC) of Canada via a Discovery Grant (RGPIN-2014-05563) to Dr. David Cooper. Dr. Cooper and this research were further supported by the Canada Foundation for Innovation and Canada Research Chairs program. IVP was supported by an NSERC PGS and a SIOGS Scholarship, and was a CIHR-THRUST PhD Fellow. Research described in this thesis was performed at the Canadian Light Source, which is funded by the Canada Foundation for Innovation, the Natural Sciences and Engineering Research Council of Canada, the National Research Council Canada, the Canadian Institutes of Health Research, the Government of Saskatchewan, Western Economic Diversification Canada, and the University of Saskatchewan.

On a personal note, my life has been touched by many people over the years of this project. There are too many friends and family to name each here but I need to thank all those have been there to lift me up and support me. One special person deserves special thanks though, and that is Mylyne Tham, who brings light and laughter to my life.

Dedication

"If I have seen further it is by standing on the shoulders of giants."
- Isaac Newton

Table of contents

List of tables

List of figures

List of Equations

List of abbreviations

°	-	Degree
Φ	-	Phi
θ	-	Theta
%	-	Percent
2D	-	Two dimensional
3D	-	Three dimensional
a_{cort}	-	Cortical area
BM	-	Bend magnet
BMIT	-	BioMedical Imaging and Therapy
BMU	-	Basic multicellular unit
BR	-	Buckling ratio
CFO	-	Collagen fiber orientation
CLSM	-	Confocal laser scanning microscopy
CLS	-	Canadian Light Source
cm	-	Centimeter
CT	-	Computed tomography
FOV	-	Field of view
g	-	Gram
I	-	Principal area moment of inertia
I_{max}	-	Maximum principal area moment of inertia
I_{min}	-	Minimum principal area moment of inertia
I_p	-	Polar area moment of inertia
I_2KI	-	Lugol's solution
ID	-	Insertion device
keV	-	Kilo electron volt
LAG	-	Line of arrested growth
mA	-	Milliampere
Micro-CT	-	Micro computed tomography
mm	-	Millimeter
s	-	Second
Sig.	-	Significant
Std. error	-	Standard error
Std. D	-	Standard deviation
SR Micro-CT	-	Synchrotron micro computed tomography
t_c	-	Cortical thickness
μm	-	Micron
Z	-	Principal section modulus
Z_{max}	-	Principal minimum section modulus
Z_{min}	-	Principal maximum section modulus
Z_p	-	Polar section modulus

Chapter 1. Introduction

1.1. Specific aims

This thesis explores the orientation of vascular canals in cortical bone in the two extant groups of flying vertebrates: birds and bats. Bone disorders such as osteoarthritis and osteoporosis are common and have a large toll on society. At a more fundamental level, bone is an important tissue with biological significance for behaviour and locomotion. Within bone, cortical bone and the cortical canals within play an important part of bone's strength and resistance to failure during loading. In cortical bone, vascular canal orientation has been linked to the growth and development of cortical bone and it's response to functional loading, and may therefore be a useful parameter for reconstructing the life history of extinct vertebrates. Vascular canal orientation is a cortical bone parameter that remains relatively unexamined and may reveal new information for understanding bone growth and development pathways and how they interact with the effects of functional loading on bone. Untangling these associations is important for a complete understanding of cortical bone development and for future analytical use of this parameter. Most previous work on canal orientation used histology, with the exception being work in the Cooper lab by Hayley Britz (2012), a previous student in the lab. This work, the first to use micro-CT to measure the orientation of canals, was limited to analyzing orientation in the plane of section.

The first goal of this thesis was to extend the method used by Ms. Britz to measure orientation in both the plane of section and orthogonal to the plane of section, to obtain the full 3D orientation of the canal network, something that had not previously been done. We chose to use synchrotron micro-CT at the Canadian Light Source BMIT beamline due to several significant advantages over conventional desktop micro-CT. The BMIT micro-CT setup uses phase contrast and has a high resolution (4.3 μm) high field of view (18-19 mm) camera system allowing for imaging of whole cortical bone cross-sections.

The second goal of the thesis is to test the following two hypotheses: first, that the orientation of vascular canals is connected to the loading a bone experiences; and second, that the orientation of vascular canals is affected by the growth rate of a bone. We used birds as our target species to investigate canal orientation and test our hypotheses. Several previous studies on canal orientation have focused on birds (de Margerie, 2002; de Margerie, Cubo & Castanet, 2002; de Margerie et al., 2004; Skedros & Hunt, 2004; de Margerie et al., 2005; de Margerie, Tafforeau & Rakotomanana, 2006; de Margerie & Rakotomanana, 2007; Simons & O'Connor, 2012; Marelli & Simons, 2014; Lee & Simons, 2015) as flight is a behavioural locomotor mode with strong forces and presents the opportunity to look for a connection between canal orientation and functional loading. This thesis exclusively uses micro-CT to measure canal orientation, and the 3D results presented here are a significant advance over previous results in the field.

1.2. Organization of the thesis

This, the first chapter of the thesis, presents a broad introduction to bone microstructure, especially cortical bone, the common methods used to study it, and an introduction to the goals of the thesis. The body of this thesis (Chapters 2-4) is organized as three research projects, presented as complete research articles. Chapter 2, entitled "*A method for measuring the three-dimensional orientation of cortical canals with implications for comparative analysis of bone microstructure in vertebrates*", was published in 2017 in the journal Micron and has been reprinted here with the permission of the publisher (see appendix). This chapter discusses in depth the 3D method used to measure vascular canal orientation. Chapter 3, entitled "*Interpreting the three-dimensional orientation of vascular canals and cross-sectional geometry of cortical bone in birds and bats*.", was published in early 2018 in the Journal of Anatomy. This paper was published with collaborators Dr. JD Johnston from the department of mechanical engineering and Dr. Ernie Walker from the department of archaeology and anthropology, both at the University of Saskatchewan and committee members for this thesis. Dr. Johnston performed the cross-sectional geometry measurements and helped with review of the paper, and Dr. Walker provided bird samples and insight into the early path this research would take. This chapter uses a comparative sample of birds and bats to attempt to link canal orientation and cross sectional geometric parameters with the specific functional loading resulting from flight. It compares the canal orientation in the humerus and femur and in the two groups. Chapter 4, entitled "*The effect of growth on the three dimensional orientation of vascular canals in the cortical bone of broiler chickens.*", is a study of vascular canal orientation in a controlled growth experiment using broiler chickens. It presents a comparison between fast growing and slow growing groups to investigate the effect of growth rate on canal orientation. Chapter 5 then concludes the thesis with a general overview of the research studies in the previous chapters and thoughts on future paths this research may go down.

1.3. Bone macrostructure and microstructure

As a material bone is composed mainly of hydroxyapatite, a hard calcium-phosphate mineral providing stiffness and compressive strength, and collagen fibers forming a soft organic component providing flexibility and tensile strength (Currey, 2002). The combination of these two components allows for bone to be both rigid and flexible. Bone is divided into two major macroscopic tissue types: cortical bone and trabecular bone. Cortical bone forms the dense outer shell surrounding the marrow cavity in the diaphysis of long bones. Trabecular bone, also called cancellous or spongy bone, is made of a mesh-like network of struts and plates. Trabecular bone is found in flat bones and in long bones at the ends in the epiphyses and metaphyses (Currey, 2002). Towards the ends of a long bone the cortical shell starts to blend with trabecular bone and the boundary between the two tissue types becomes less distinct and forms a transition zone. Cortical and trabecular bone are shown in figure 1.1.

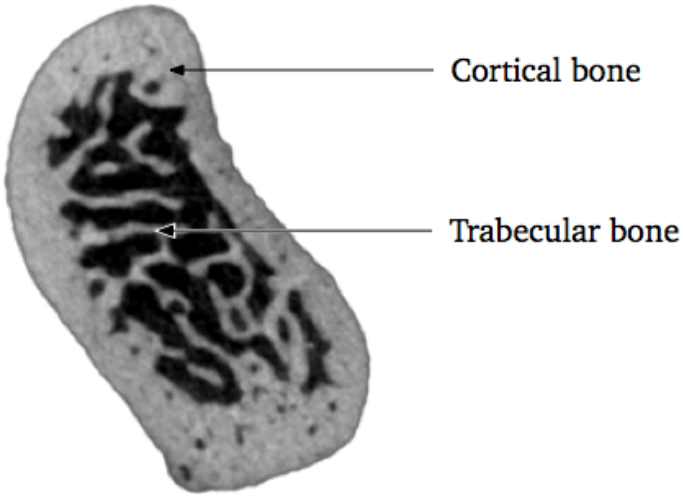

Figure 1.1: Cortical and trabecular bone shown in a micro-CT scan of the proximal region of a rat ulna. Cortical bone forms the solid shell surrounding the marrow cavity and the mesh of trabecular bone struts.

Bones are formed through two initial processes: endochondral and intramembranous ossification (Hall, 2005). Intramembranous ossification is simpler and results directly from mesenchymal condensation of osteoblasts, while endochondral ossification is more complex. Bones formed by endochondral ossification such as long bones are first laid down as a cartilage precursor. From this structure, bone is laid down longitudinally around centres of ossification extending the bone into its full length. During this process bone is also laid down diametrically by direct deposition at the periosteum. Bone formed during these processes is called primary bone. During life, bone is constantly adapting to the constantly changing biological and loading environment it is experiencing. The processes that govern bone's responses during life are grouped into two main categories: modeling and remodeling (Frost, 1963). Modeling changes the geometry of the bone, including its shape and size, through bone formation and resorption at the periosteal and endosteal bone surfaces and on the surfaces of vascular canals (Maggiano, 2012). Bone formed during modeling is also classified as primary bone. Primary bone can be laid down either as woven bone, with irregularly oriented collagen fibres, or as lamellar bone, in concentric layers forming circumferential rings in the diaphysis (Currey, 2002). Woven bone is mostly found during the early development of a bone or during fracture repair. As lamellar bone forms layers on the periphery of the bone it encompasses vascular canals in the bone which then form primary canals/osteons. Modeling and remodeling are illustrated in figure 1.2.

Remodeling is a targeted process of renewal and repair that occurs throughout life. This process is driven by coordinated groups of bone cells known as basic multicellular units (BMUs) (Frost, 1963). These BMUs operate with osteoclasts at the head forming a leading or cutting cone which removes existing bone to form a resorption space, followed by osteoblasts in a closing cone which fill in the space, initially with osteoid material and later with mineralized bone, leaving a new vascular canal. This canal is formed around the

central blood vessel in the BMU, and surrounded by concentric rings of new bone called lamellae (Robling, Castillo & Turner, 2006). Remodeling is thought to be a targeted process driven by strain gradients in the lacuno-canalicular network where BMUs are initiated to respond to loading and microdamage in the bone (Burr et al., 1985; Martin, 2007). These canals and the surrounding lamellae are known as Haversian systems or secondary osteons (Frost, 1963). The result of remodelling is the continual creation of new osteons and vascular canals in the tissue and the formation of secondary bone. Remodeling occurs in most but not all large vertebrates and is found in all major groups of vertebrates from dinosaurs and other extinct vertebrates to modern animals including birds, reptiles, fish, and mammals (Enlow & Brown, 1958; Witten & Huysseune, 2009). The presence of remodeling has been proposed to increase the strength of a bone (Currey & Alexander, 1985) and may be linked to body size, with smaller bones having fewer Haversian systems (de Ricqlès et al., 1991).

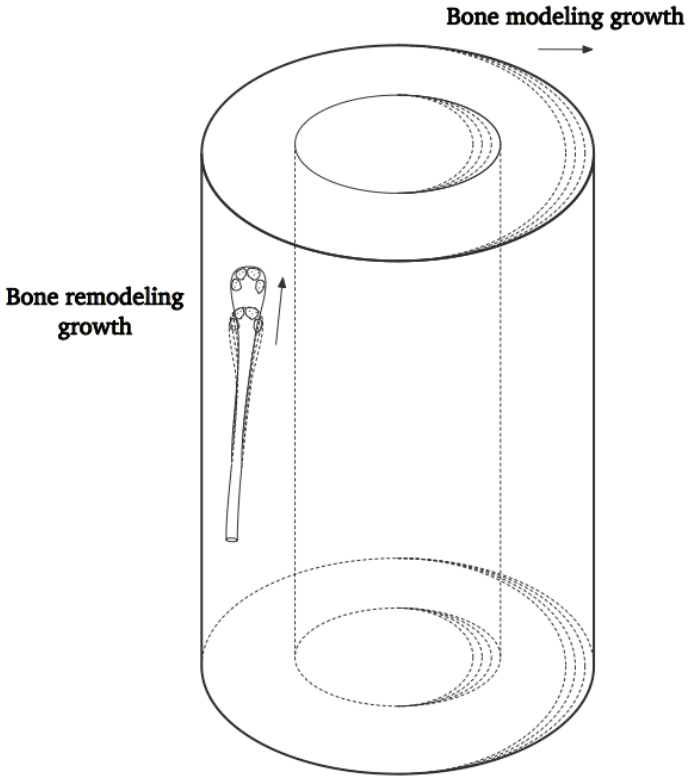

Figure 1.2: Modeling and Remodeling. Modeling growth acts on bone surfaces and affects the dimensions of the bone, while remodeling acts through BMUs and replaces existing bone tissue for repair or optimization of cortical bone.

Cortical bone, and cortical porosity are important components of whole bone mechanical strength (Carter, 1984; Ammann & Rizzoli, 2003; Augat & Schorlemmer, 2006; Cooper et

al., 2016). This thesis is focused on cortical bone morphology and microstructure, a developing area of active research. Studies in humans and animals (Pearson & Lieberman, 2004) have shown that behavioural differences in locomotion and upper limb activity cause differences in cortical bone diaphyseal cross sectional morphology. Measurements of cortical area, trabecular/marrow area, cortical thickness, trabecular/marrow thickness, and calculated parameters based on these measures reflect bone attributes such as strength and resistance to loading (Lieberman, Polk & Demes, 2004; Shaw & Stock, 2009; Johnston et al., 2014). Measures such as the principal area moment of inertia (I) and the principal section modulus (Z) reflect the resistance of a bone to bending around a chosen axis, with the maximum and minimum measures (I_{max} vs I_{min}, Z_{max} vs Z_{min}) reflecting the highest and lowest resistances of the bone being most commonly used. The polar area moment of inertia (I_p) and polar section modulus (Z_p) reflect the bone resistance to torsional loading (Marelli & Simons, 2014). Cortical area is a measure of the resistance of a bone to axial compression (Lieberman, Polk & Demes, 2004), while cortical thickness and outer cortical diameter reflect resistance to bending (Ammann & Rizzoli, 2003). The circularity of a bone also reflects loading direction, with elliptical bones interpreted as having higher resistance to bending along the major axis, whereas more circular bones have more even bending resistance in every direction and are more resistant to torsional loading (de Margerie et al., 2005). See figure 1.3 for illustration of the maximum and minimum axes and chapter 3 for more detail on cross sectional parameters and their calculation.

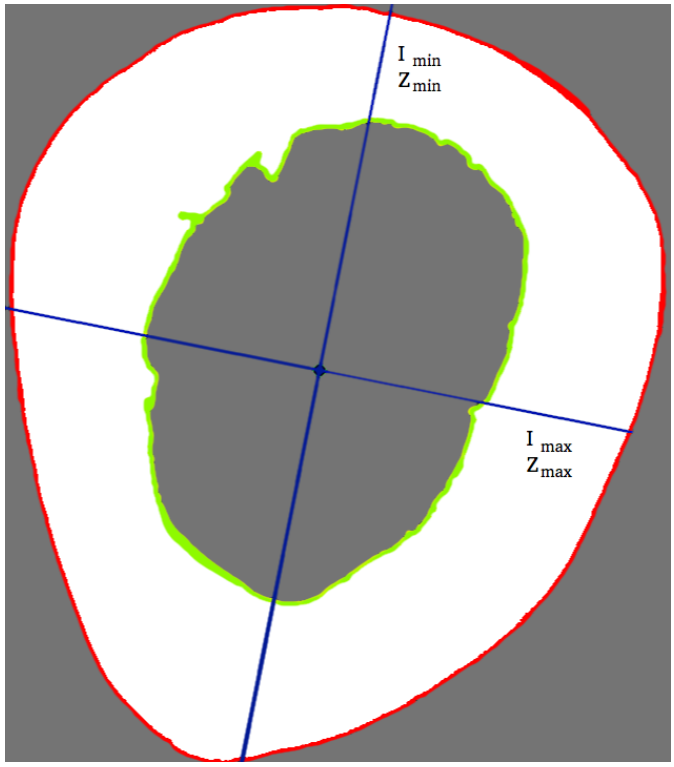

Figure 1.3: Representative cross sectional image used for Chapter 3 analysis. This image is of a Common loon humerus taken at mid-shaft. The white region is the cortical area,

the red outer line and the green inner line represent the periosteal and endosteal surfaces respectively. Maximum and minimum principal axes are shown in blue and labelled. These axes represent the axes across which the bone's resistance to bending is highest and lowest. The intersection of the axes is the bone centroid.

In cortical bone microstructure, cortical porosity has been tied to mechanical properties including fracture resistance (Yeni & Norman, 2000) and has been linked with age related degeneration of bone and osteoporosis (Nishiyama et al., 2010). A number of parameters exist to quantify the morphology and distribution of vascular canals in the cortex (Cooper et al., 2003). These include canal volume, canal surface area, cortical porosity (also called percent porosity), and the number, diameter, separation of canals. Another parameter of interest has been vascular canal orientation, which has been linked to functional loading history (Hert, Fiala & Petrtyl, 1994; Petrtyl, Hert & Fiala, 1996; de Margerie, 2002). This last parameter, canal orientation, is the overarching focus of this thesis, and it is described further in detail in chapters 2, 3, and 4.

1.4. Bone imaging

1.4.1. Histology

The first visualization of bone microstructure was done by ground section undecalcified bone histology, and histology remains to be a useful method and the most accessible method of imaging bone tissue (Crowder & Stout, 2012; Padian, 2013). Specimens are cut into thin sections using a diamond wafer saw and then ground to a thickness of 50-100 μm and imaged using visible light microscopy. Additional microscopy enhancements such as linearly or circularly polarized light can help to visualize additional features in bone microstructure (Cho, 2012). Histology has excellent resolution - with proper components an optical light microscope has resolution close to the wavelength of visible light, close to 200 nm. Histology can visualize osteon systems including BMUs and resorption spaces, the lacuno-canalicular network, collagen fiber orientation, micro-cracks, and cortical bone tissue type (see figure 1.4). Importantly, histology can distinguish primary bone and primary canals from secondary bone and secondary canals by visualizing features created during remodeling like osteon boundaries. Histology has two significant weaknesses – by its nature it is limited to analyzing bone in only two dimensions, while bone is a fundamentally 3D tissue, and a single histological section is an inherently small sample. Bone parameters often vary significantly at different sampling sites in a bone, so the choice of where to take a section is critical when using histological methods. Both trabecular and cortical bone exhibit significant anisotropy in their structure, which limits the effectiveness of histological measurements. For example, the use of histology in measuring lacunar parameters is limited to measuring lacunar density in the small numbers present in a single histological section, and measurements of lacunar morphology are inherently limited by the missing third dimension (Carter et al., 2013). Some attempts have been made to expand the method into three dimensions with serial sectioning, a challenging method which attempts to analyze consecutive histology sections (Cohen & Harris, 1958; Tappen,

1977; Dehoff, 1983a; Stout et al., 1999), but most attempts at serial sectioning were abandoned with the advent of newer 3D methods such as confocal laser scanning microscopy and x-ray imaging combined with computer visualization. The necessity of using 3D methods for studying cortical bone morphology was especially emphasized by Stout (1999), who showed that osteons previously described as "dumbbell-shaped" were actually the result of sectioning through a branching point in the osteon network.

1.4.2. Confocal laser scanning microscopy

An important development in bone imaging was the maturation and use of confocal laser scanning microscopy (CLSM) in the 1980s (Amos & White, 2003) alongside the use of fluorescent labels. CLSM uses a laser light source and a pinhole to focus light onto a small area of a sample and isolate only the focal area. The light beam is then rastered across the sample to create the image. CLSM offers a higher resolution than conventional optical microscopy by using a laser source, and has better depth sensitivity allowing for imaging at multiple points along the z dimension. By changing the focal length the microscope can take images at different depths in the sample. While this allows for the creation of image stacks allowing for 3D visualization of biological targets, the depth penetration is low, providing only a small allowable sample thickness around 1 mm (Paddock, 2000). CLSM is limited to a very small sample size, which limits the imaging of larger samples. CLSM is an excellent technique for imaging the lacuno-canalicular network (Ciani, Doty & Fritton, 2009; Ashique et al., 2017) and bone tissue but isn't efficient for imaging the cortical canal system as the 'height' of the sample is extremely limited and the sample size is small.

1.4.3. Micro computed tomography

The most important tool for observing and assessing trabecular and cortical bone morphology and microstructure is micro computed tomography (micro-CT). Micro-CT is high resolution computed tomography (CT) with a generally accepted range from around 1-100 μm and was first used to image trabecular bone microstructure by Feldkamp (1989). Micro-CT quickly became the gold standard for 3D analysis of bone microstructure (see figure 1.4). The two main micro-CT systems are synchrotron x-ray sources and 'desktop' or 'laboratory' based commercial systems using polychromatic microfocus x-ray tubes. Computed tomography was initially developed in 1973 (Hounsfield, 1973) and was rapidly adopted in radiology on the basis of its revolutionary 3D imaging power, with G. N. Hounsfield and A.M. Cormack sharing the 1979 Nobel Prize in Physiology or Medicine for its development. Computed tomography uses differential x-ray absorption across materials or tissue types to construct a 3D image from 2D x-ray projection images. These projection x-ray images are taken in series of an object rotated at defined angles through 180 or 360 degrees. Each pixel in the projection images represents a line integral of the x-ray energy absorption coefficients in the path through the scanned object so the denser a material is to x-rays, the darker the resulting pixel will be. From the series of projections, the line integrals can then be solved to obtain the absorption coefficients of the different materials in the object, and create a 2D map of the absorption coefficients in the plane of

the x-ray beam. In this way 2D projection images are turned into image slices that can be compiled to form a 3D volume that accurately represents the original sample. In the reconstruction image the gray levels are inverted so that the background is dark and areas of higher absorption are bright.

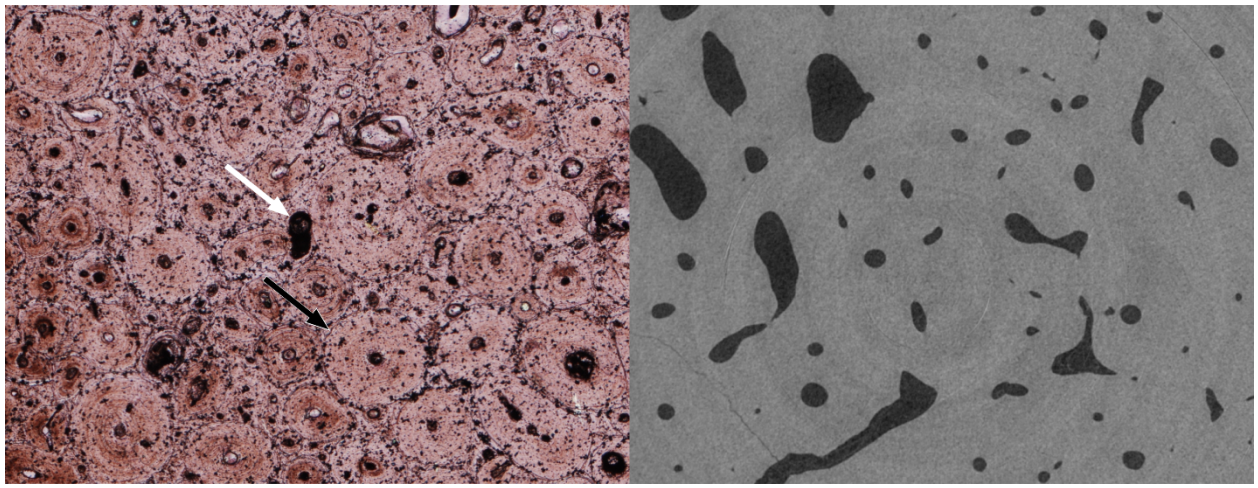

Figure 1.4: Comparison between histology and micro-CT techniques. On the left is a ground bone section histology image of an unidentified dinosaur bone, showing bone full of Haverisan systems (see black arrow for an example) with a few leftover primary canals (see white arrow for an example). In the histology image osteocyte lacunae, osteon boundaries, and osteon lamellar rings are all visible. On the right is a micro-CT image of human femoral bone. In this image differentiators of primary and secondary canal systems are noticeably absent.

Absorption contrast has difficulty with differentiating soft tissue, and this has led to the development of techniques to enhance contrast through the use of stains and the use of phase contrast. Contrast-enhanced micro-CT relies on absorption contrast but uses stains based on heavy elements to increase the absorption of x-rays in targeted soft tissue (Metscher, 2009a,b). The most common stains used include phosphotungstic acid, phosphomolybdic acid, osmium tetroxide, potassium iodide, and Lugol's solution (I_2KI) (Pauwels et al., 2013) and are selected for solubility in tissue and the ability to bind to the tissue of interest. Examples of the use of contrast-enhanced imaging include imaging the jaw musculature in rodents (Cox & Jeffery, 2011) and imaging the development of early tooth formation (Raj et al., 2014).

Phase contrast imaging produces excellent image quality, and enhanced contrast which helps with tissue (especially soft tissue) discrimination. Phase contrast also has a resolution enhancing effect that can help with imaging small targets (Lewis, 2004). A phase shift is produced as photons pass through a sample and scatter and is capable of generating significantly enhanced contrast (Zhou & Brahme, 2008). The resulting phase contrast in the image decreases less rapidly with increasing x-ray energy than absorption contrast, and is more tolerant to noise. While phase contrast imaging can be done using a

polychromatic source (Wilkins et al., 1996) and a few commercial phase contrast systems exist such as the Bruker SkyScan 1294 phase-contrast micro-CT, most phase contrast imaging is done at synchrotron beamline facilities.

Several methods of exploiting the phase shift exist and have been incorporated into synchrotron techniques, and use a monochromatic beam produced by a perfect crystal. Most of these methods, including diffraction enhanced imaging (Chapman et al., 1997), and interferometry or diffraction grating phase contrast (Bravin, Coan & Suortti, 2013), use further crystal optics to refine the x-ray beam and are not discussed here. The simplest form of phase contrast imaging is called propagation or in-line phase contrast (Zhou & Brahme, 2008). In-line phase contrast is does not require any additional crystal optic devices and is based solely on manipulation of the x-ray imaging geometry. Instead placing the sample very close to the detector the sample is placed at an increased distance from the detector (see figure 1.5). As the x-ray beam passes through material interfaces it is bent slightly, causing changes in the x-ray wavefront that propagate over the distance between the object and the detector (Snigirev et al., 1995). This creates highlighted bright and dark fringes at the interfaces between materials of different x-ray refractive index. The width of these fringes depends on the propagation distance between the object and the detector, and by varying this distance the width of these lines can be optimized to show an easily distinguishable border, while preserving relatively accurate dimensions of the highlighted structures in the near field where most imaging is performed (Britz, Carter, et al., 2012). This leads to excellent contrast in soft tissue compared to absorption imaging, where the different soft tissue types are often unable to be differentiated from each other and water due to their similar absorption coefficients (Momose, Takeda & Itai, 2000). Phase contrast imaging in cortical bone produces a 'halo' effect around the periosteal and endosteal borders, as well as the edges of cortical canals and osteocyte lacunae (Britz, Carter, et al., 2012; Carter et al., 2013). These halos make segmentation of the cortical bone microstructure easier and more reliable during data analysis and help to capture the smaller canals in cortical bone. Phase contrast at high resolution (0.5-1 μm) is able to delineate osteons boundaries in cortical bone (Cooper et al., 2011).

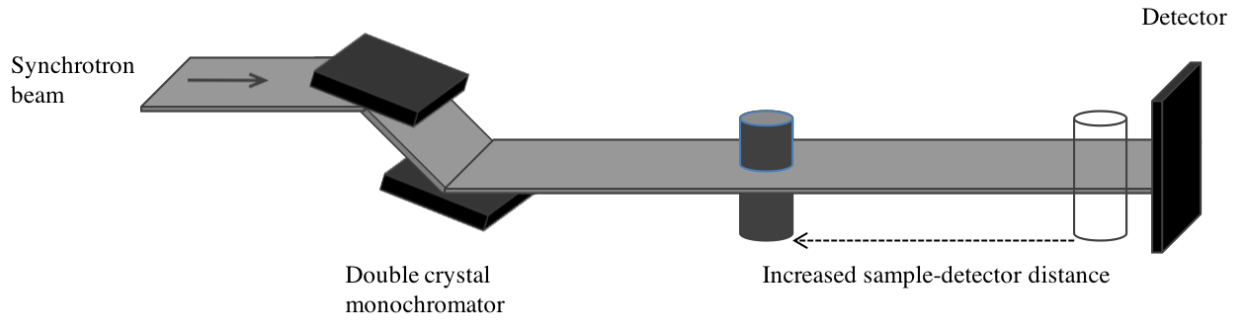

Figure 1.5: In line phase contrast set-up. The main aspect of an in line phase contrast imaging set-up is the increased sample to detector distance. Image adapted from Pratt (2013).

Desktop micro-CT systems are primarily based on cone beam x-ray sources, which create geometric magnification to increase resolution but also increase blurring compared to parallel beam sources. The imaging capabilities of desktop systems are dictated by a few important characteristics of the x-ray tube used. The spot size of the x-ray tube limits the resolution, the voltage of the tube dictates the energy and thus penetration of the x-ray beam, and the current of the tube determines the x-ray flux produced. All of these factors are generally lower than in synchrotron sources, limiting the size/density of the samples they can image. Newer systems with focused x-ray sources and nanometer spot sizes have also been developed which allow imaging with pixel sizes around 400-700nm. While these 'nano-CT' systems have extremely high resolution, they also have extremely limited fields of view (van Hove et al., 2009; Peyrin et al., 2014). Nano-CT systems exist using both desktop and synchrotron sources, with desktop systems further limited by lower flux resulting in extremely long scan times and low signal to noise.

Synchrotron micro-CT uses x-rays produced by the passage of an electron beam traveling through strong electromagnets. These magnets come in several varieties, with the most common being bending magnets and insertion devices such as wigglers and undulators. The produced x-ray beam travels down a 'beamline' where it is collimated and filtered creating a near parallel x-ray source with a very small spot size and low divergence. The biggest advantage of using a synchrotron source is the increased flux, which is several orders of magnitude greater than that produced by desktop sources (Kinney & Ladd, 1998). This allows for the use of optical instruments on the beamline including monochromators and other crystal optics for phase contrast imaging. A monochromatic beam has a narrow x-ray bandwidth of less than a hundred eV (Kinney & Nichols, 1992), which is important in bone imaging to avoid "beam hardening" artifacts. These artifacts result from x-rays of different energies being differentially absorbed by tissue. Lower energy x-rays in the beam are absorbed faster than higher energy x-rays which penetrate more easily. As a result, tissue density is artificially lower in the interior of the sample and higher in the exterior. Avoiding beam hardening is important for taking accurate measurements of bone mineral density (Peyrin et al., 1998). Synchrotron sources also offer higher resolutions than typical desktop x-ray sources, with submicron level imaging becoming more common at these institutions (Schneider et al., 2007). Synchrotron micro-CT systems are well positioned to take advantage of phase contrast techniques to provide improved visualization of smaller targets or samples with low x-ray absorption like soft tissue. Synchrotron micro-CT is limited by cost, limited imaging time often requiring peer-reviewed access proposals, and higher difficulty of use compared to common commercial systems.

The 3D nature of bone's microstructural network means using a 3D technique to study it is inherently more appropriate. Measuring morphology and structural parameters in 2D requires assumptions about the unseen third dimension which may turn out to be inaccurate. Faulty assumptions made in parameter calculations can undermine results. CT is the most versatile 3D imaging technique currently available to be applied to bone, with methods available for both ex vivo and in vivo scanning at resolution ranges that can scan

everything from full bodies in large animals to lacunar spaces and canaliculi in rodents. However, the breadth of CT systems makes choosing the appropriate system important. Desktop micro-CT is limited in field of view and resolution, nano-CT is high resolution but extremely limited in field of view, and synchrotron systems have high flexibility and can achieve high resolutions with larger fields of view but are complicated to set up and access is limited. Compared to histology, micro-CT has lower resolution but provides important 3D information. Several studies have combined the two methods, using micro-CT for 3D information and histology for high resolution of bone features of interest (Hennig et al., 2015).

Chapter 2. A method for measuring the three-dimensional orientation of cortical canals with implications for comparative analysis of bone microstructure in vertebrates

This chapter has previously been published as: Pratt, I.V. & Cooper, D.M.L., 2017. A method for measuring the three-dimensional orientation of cortical canals with implications for comparative analysis of bone microstructure in vertebrates. *Micron*, 92, pp.32–38 and is reprinted here with permission from the publisher (see appendix).

2.1. Introduction

The importance of cortical porosity on bone strength has been increasingly studied over the last decade as three dimensional (3D) x-ray imaging techniques have become able to quantify porosity *in vivo* in animals and humans (Buie et al., 2007; Burghardt et al., 2010; Nishiyama et al., 2010; Zebaze et al., 2010; 2013; Harrison & Cooper, 2015; Pratt et al., 2015; Kawalilak et al., 2016; Vilayphiou et al., 2016). One aspect of cortical porosity that remains relatively unexplored is the orientation of the cortical canals. The orientation of primary and secondary canals has been proposed to reflect mechanical loading of the bone in humans (Hert, Fiala & Petrtyl, 1994; Petrtyl, Hert & Fiala, 1996) and animals (de Margerie, 2002; de Margerie et al., 2005; de Margerie & Rakotomanana, 2007; Simons & O'Connor, 2012; Marelli & Simons, 2014), or the growth rate of a bone (de Margerie, Cubo & Castanet, 2002; de Margerie et al., 2004; Lee & Simons, 2015). de Margerie (2002) proposed that a cortex containing predominantly circumferential canals in birds was a functional response to a torsional load from active flight. Primary canals are formed during the initial growth and development of the bone through modeling (Maggiano, 2012), while secondary canals are bored in cortical bone throughout life during remodeling. In most mammals and birds, the cortical bone is lamellar and contains many primary canals incorporated into the bone during development (Mitchell & van Heteren, 2015). It is predominantly these primary canals that we examine in this paper. In mature human tissue the predominant canal type is secondary. de Margerie (2002) measured the orientation of canals in histological slices by classifying canals into four categories: radial, longitudinal, oblique, or circumferential. A radial canal appears to extend from the centroid of the bone, like the spokes on a bicycle wheel. A longitudinal canal is aligned with the long axis of the bone. A circumferential canal is parallel to the contour of the diaphysis. An oblique canal is intermediate between a radial and a circumferential canal. They calculated a 'laminarity' index, the ratio of the area of the circumferential canals to the total area of all canals. Measuring the 3D orientation of cortical canals has historically used histology, a primarily two dimensional method. Two dimensional methods are inherently weaker as a result of the measurement being taken only in one plane. The method used by de Margerie (2002) misses the fact that many canals are oblique (sometimes referred to as 'reticular'), and as a result overestimate the number of true radial, longitudinal, and circumferential canals. Attempts to create more accurate indices (de Boef & Larsson, 2007b) remain limited by

the histological method used, as the longitudinal angle can only be estimated from the cross-section, and not directly measured. This estimation is based on how circular the canal's cross-section appears in a histological section, with circular canal cross-sections interpreted to be longitudinal, and more oval canal cross-sections are interpreted to represent canals that are more transverse. Estimating measurements of the 3D orientation of a canal or osteon from a cross-sectional image can be misleading. Osteons tend to be more oval than circular in cross-section (Hennig et al., 2015), leading to difficulty in analysis. Canal shapes are also not always circular and therefore the orientation that is estimated may differ significantly from the actual orientation. Prior to the development of micro-CT, the 3D methods available were difficult, tedious, and destructive (Dehoff, 1983b; Odgaard et al., 1990). However, micro-CT offers easy access to the canal network, and computer technology allows automated methods which can measure many canals in short order. Micro-CT is an x-ray imaging method that uses successive images of a rotating object to reconstruct a 3D volume. Micro-CT typically relies on contrast created by differences in absorption of x-rays by different materials, although phase information is increasingly used (Pratt et al., 2015). Micro-CT was first used to study bone in late 1980s (Feldkamp et al., 1989), and has proliferated explosively since then due to the high quality of the data it produces. It is now used extensively to study both trabecular and cortical microstructure (Holdsworth & Thornton, 2002; Cooper et al., 2003; Bouxsein et al., 2010). Micro-CT allows for direct visualization of cortical porosity, and quantification of the canal network. The limitation of micro-CT is that commercial systems are often unable to differentiate primary and secondary canals. Dechow et al (2008) used confocal microscopy and micro-CT to examine cortical structure, including some analysis of canal orientations. They imaged rectangular cut bone samples and compared the canal orientation with the axes of mechanical stiffness. They found that in the human femur average canal orientation tends to align with the axis of maximum stiffness in the plane of the cortical bone plate, suggesting a link between function and canal orientation as well. However, their work was limited to analysis of cut samples, and they did not identify the morphological axes of the bone. Previous work in Cooper's bone imaging group has measured the orientation of canals with respect to bone's long axis (Britz, Jokihaara, et al., 2012), showing the ability to differentiate between radial and longitudinal canals, and significant differences in orientation between normal and immobilized rats. The currently described method builds on that work, by adding the ability to measure orientation in the orthogonal plane, thus providing the full 3D orientations of each canal in the cortical network. Adding this angle allows differentiation not only between radial and longitudinal canals, but also between radial and circumferential canals. It also provides the ability to identify the different types of oblique canals. These 3D orientations allow for a more accurate calculation. This method provides the ability to investigate questions about how canal orientations are built-in during growth (primary), and how the remodeling process alters the (secondary) canal network in humans and in comparative animal studies. An improved understanding of the processes by which canals develop and how their direction is determined will add to our ability to interpret cortical microstructure and infer behaviour in both extant and extinct animals.

2.2. Methods

2.2.1. Micro-CT

We used two micro-CT systems for this study. The first is a SkyScan 1172 desktop microtomograph (Kontich, Belgium) with a <5 μm x-ray source size and an 8.83 μm camera pixel size. The second is a Hamamatsu C9300-124 optical camera paired with a Hamamatsu A40 x-ray converter at the BioMedical Imaging and Therapy (BMIT) facility at the Canadian Light Source Synchrotron. This set-up provides a 4.3 μm pixel size, from a <5 μm source size. The BMIT synchrotron micro-CT set-up has an open gantry, and a field of view of 15mm that is wider than that of the desktop system. Offset scanning methods can also be used to increase the field of view further to 30 mm. As a result, synchrotron micro-CT is ideal for imaging whole bones from larger animals/humans. The BMIT facility offers a number of different camera set-ups, with pixel sizes ranging from 0.9-100 μm. Any micro-CT system may be used with this method, although resolutions of < 10 μm are needed to accurately capture the morphology of the canal network (Matsumoto et al., 2006; Cooper et al., 2007). Frame averaging is typically used to improve the signal-noise ratio, and aluminum filtration of the beam and beam-hardening correction algorithms are used to minimize beam hardening. While the method is constructed with micro-CT in mind, other imaging methods that produce 3D data sets could potentially be used.

2.2.2. Reconstruction & Skeletonization

We use NRecon 1.6.10.5, a commercial reconstruction software package (Bruker SkyScan, Kontich, Belgium) to reconstruct micro-CT data for analysis. The reconstructed micro-CT slices are then imported into Amira 6.0 (FEI Company, USA), where the canals are segmented and skeletonized. The canals are segmented using a global threshold to separate bone from soft tissue and air in the Amira Segmentation Editor. The value of the threshold was chosen to maximize the canal structure visible and minimize noise. The exact value of the threshold will vary depending on the imaging set-up used. They are then skeletonized using the Auto Skeleton module. The skeletonization process in Amira calculates a distance map of the segmented canals and then performs a thinning of the canals which preserves the topology of the canal network, including the length and orientation of the canals. The end result of the skeletonization process is a lineset which contains a set of co-ordinates for each canal. This lineset file is then simplified using a custom ImageJ (NIH; http:// rsb.info.nih.gov/ij/) macro. This process identifies the branch points in the canal network and breaks each canal down into a series of shorter canal segments. Simplification of the canals into canal segments better captures the variability in orientation of the canals and provides a more accurate representation of the canal network. In particular, curved canals need to be broken up to capture the detail of their orientations. The length of the canal segments is a user choice, but it is recommended to keep the canal length at approximately 100-150 μm, the thickness of a typical histological ground section. Using shorter canal segments provides a more robust estimate

of the orientation of curved canal sections, though with diminishing returns (Britz, Jokihaara, et al., 2012). This lineset will form the basis for the orientation measurements (see Figure 2.1). Other architectural parameters such as canal length and canal connectivity density can be measured from the skeleton as well (Cooper et al., 2003). For a scan of a whole bone as in the examples provided here, the micro-CT slices are also used to create a lineset of co-ordinates of the centroid of the bone, producing a lineset with one centroid (x,y) co-ordinate for each integer z value. If the scan is only of a section of the bone, the centroid position can be reconstructed from the endosteal profile of the bone or defined manually. Using the micro-CT data, the co-ordinates of the bone's centroid in each micro-CT slice can be identified. The series of centroid co-ordinates over the whole data set then acts as a proxy for the long axis of the bone. The limitation of this method is that if the bone's shaft is curved, the long axis of the bone will be much more difficult to define. This analysis is then most applicable to the analysis of relatively straight long bones.

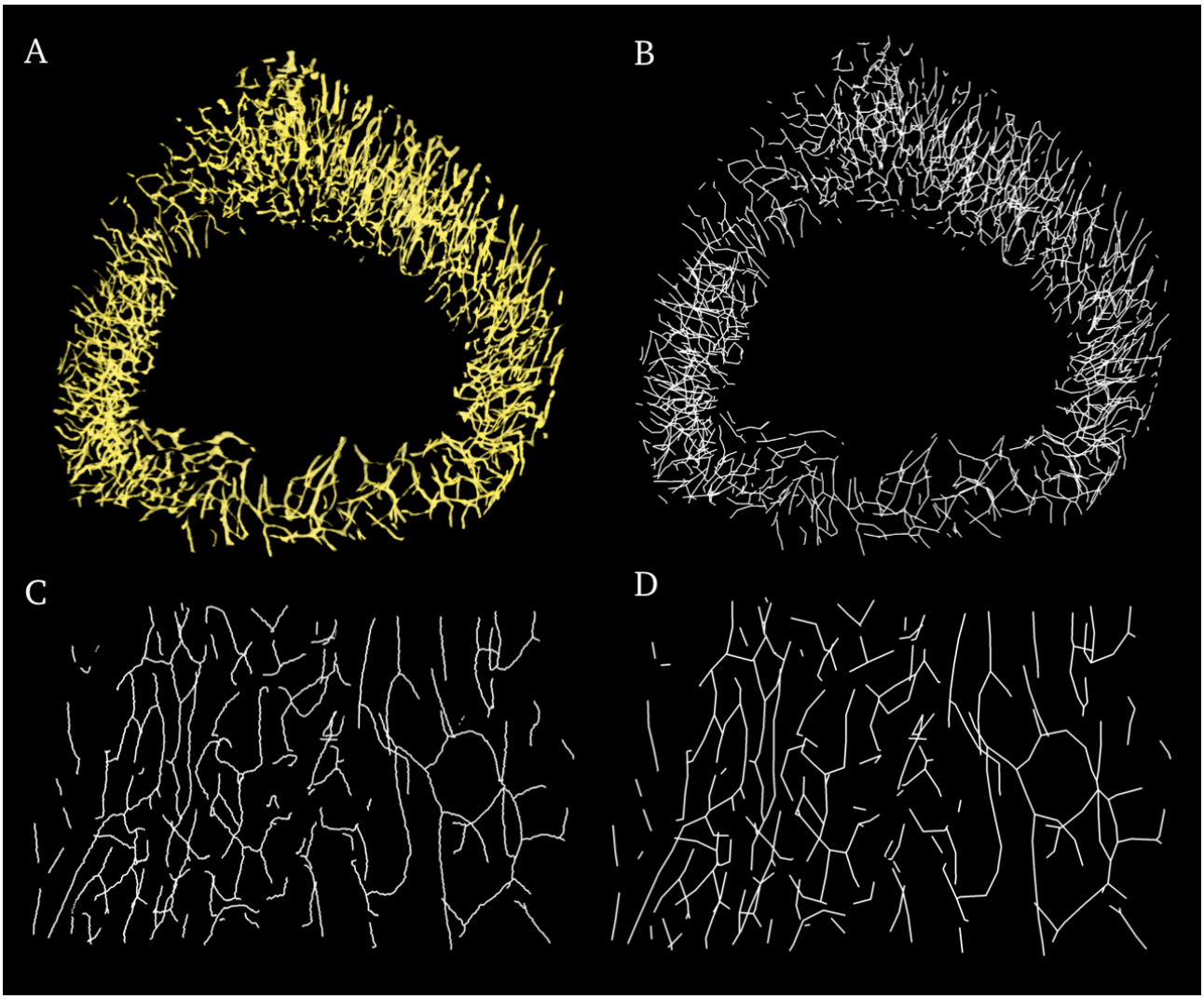

Figure 2.1: Skeletonization Process in the rat (*Rattus norvegicus*) tibia – A shows the initial canal render; B shows the skeletonized canal network; C is a zoom in of the skeletonized canal network; and D shows the simplified canal network.

2.2.3. ImageJ Orientation Macro

We use a custom ImageJ macro to measure the orientation of the canals in the network. The macro first simplifies the skeleton into short canal segments. Once the canal segments are obtained, the macro calculates intermediary values for each segment using the centroid lineset and the simplified skeleton lineset. The values calculated are the midpoint of each segment, the distance between each segment endpoint and the segment midpoint, the distance between the centroid and the segment midpoint, and the distance between each segment endpoint and the centroid. From the intermediary values we measure two angles to capture the full 3D orientation.

Phi (ϕ) measures the angle between a canal segment and the long axis of the bone, where an angle of 0° indicates a canal segment is perpendicular to the long axis (transverse), and 90° indicates it is parallel to the long axis (longitudinal). Phi on its own can only differentiate between longitudinal and transverse canals. Phi is measured as the arctangent of the distance between a canal segment endpoint and a longitudinal line over the longitudinal (z) length of the canal segment (see equation 2.1 and figure 2.2).

$$\emptyset = \tan^{-1}\left(\frac{\sqrt{(x_2 - x_1)^2 + (y_2 - y_1)^2}}{z_2 - z_1}\right)$$

Equation 2.1: Phi

Theta (θ) measures the angle between a canal segment and the line from the centroid of the bone through the mid-point of the canal segment. Theta is measured in the plane of the section, perpendicular to the long axis. For theta, an angle of 0° means a canal segment is radial, and one of 90° means the canal segment is circumferential. Theta is measured for a canal segment using the law of cosines, by taking the arccosine of the angle between the centroid of the medullary cavity, the midpoint of the canal segment, and an endpoint of the segment (see equation 2.2 and figure 2.2).

$$\theta = \cos^{-1}\left(\frac{(x_c - x_1)^2 + (y_c - y_1)^2 - (x_m - x_1)^2 - (y_m - y_1)^2 - (x_c - x_m)^2 - (y_c - y_m)^2}{2\sqrt{(x_m - x_1)^2 + (y_m - y_1)^2}\sqrt{(x_c - x_m)^2 + (y_c - y_m)^2}}\right)$$

Equation 2.2: Theta

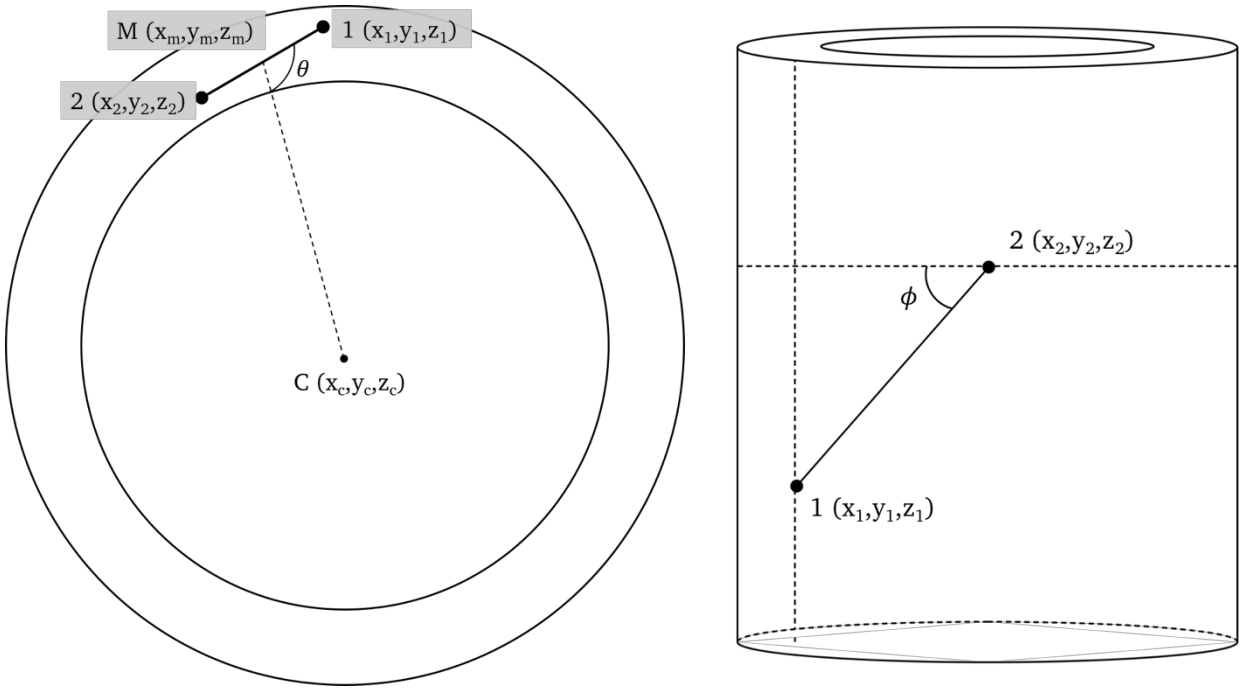

1. Theta (top down view)

2. Phi (side view)

Figure 2.2: 1 and 2 are the endpoints of the canal segment, M is the midpoint of the canal segment, C is the centroid of the medullary cavity

The macro outputs an identifying segment number, co-ordinates for each endpoint and the midpoint in the segment, co-ordinates for the centroid position at the height of the midpoint of the segment, the intermediary values described above, and the measures of phi and theta. The segment numbers can be used in Amira to link the orientation of canal segments to measures of canal morphology such as canal diameter and length. The speed of the macro depends on the speed of the CPU used and the number of canals in the data set. Since the files created by the skeletonization process are text files, the resolution of the scan is not a factor in the time it takes to run the macro.

2.2.4. Analysis

We bin the canals into nine groups, separating each axis into 22.5° increments to define radial, oblique, longitudinal, and circumferential canals. The range of the increment matches the work done by de Margerie (2002). Each increment group can be assigned a 'type' for the orientation of the canals as shown in Table 2.1. From these groups we can calculate indices of laminarity, or any other category of interest. To calculate the laminarity index, we simply take the proportion of circumferential canals of the total number of canals and report it as a percentage. We have two options on how to measure the index: we can calculate a more conservative index, which captures only the transverse circumferential, the canals which are truly circumferential (they are flat in the plane of

section); or we can calculate a more liberal index, which captures all canals with a theta of 67.5-90.

Table 2.1: Orientation type

	Theta 0-22.5	**Theta 22.5-67.5**	**Theta 67.5-90**
Phi 0-22.5	Transverse radial	Transverse oblique	Transverse circumferential
Phi 22.5-67.5	Oblique radial	Oblique	Oblique circumferential
Phi 67.5-90	Longitudinal radial	Longitudinal oblique	Longitudinal circumferential

Canal orientation can be visualized as rosette charts in two dimensions with each angle shown separately (see (Dechow, Chung & Bolouri, 2008) for an example of this), or in 3D with the angles visualized together. Using a custom python script implemented using MatPlotLib (Hunter, 2007) we can create a 3D heatmap (see Figure 2.3) of the 3D orientations of each canal segment. In these plots each canal segment is visualized as a point on the surface of a quarter sphere. We used the viridis colourmap, with dark blue representing a lower density of canals with those orientations and bright yellow a higher density. Sections of these 3D plots correspond to the different orientation types, allowing for visualization of the data presented in Table 2.2 and 2.3.

2.2.5. Examples

Animal ethics approval was granted under protocol 20130114 by the University of Saskatchewan Animal Research Ethics Board of the University Committee on Animal Care and Supply and by the Canadian Light Source. Samples were obtained from the Zooarchaeology collection in the department of Archaeology and Anthropology at the University of Saskatchewan. Bones in the collection are all defleshed and cleaned. Whole bone cross-section micro-CT data was obtained for two bones, a *Rattus norvegicus* (rat) tibia and a *Buteo jamaicensis* (red-tailed hawk) humerus. Both scans were taken at mid-shaft. These specimens are chosen to illustrate different canal patterns - rats are typically thought to contain predominantly longitudinal and radial canals (Britz et al., 2010), while larger birds tend towards a mix of longitudinal and circumferential canals (de Margerie et al., 2005). The rat tibia was scanned using a SkyScan 1172 (details above) with an effective pixel size of 1.4 μm, 4 frame averaging and a step size of 0.07° over 180° for a dataset 1.7 mm tall in the z-axis. The red-tailed hawk humerus was scanned at the BMIT synchrotron facility (details above) with a 4.3μm effective pixel size. This scan used 4 frame averaging and a step size of 0.096° over 180° for a dataset 2.8 mm tall in the z-axis.. The hawk humerus was run through the macro with a segment length of 30 pixels, while the rat tibia was run with a segment length of 90 pixels. As a result, each has a similar canal segment length of about 130 μm.

2.3. Results and Discussion

The macro was able to quantify observable differences between the two specimens. Results are shown in Tables 2.1 and 2.2, and in Figures 2.3 and 2.4. The rat (Table 2.1) has a cortical network that contains a higher number of radial canals than circumferential in the theta axis, with 32.5% of the canals falling in the 0-22.5° range, and only 16.9% falling in the 67.5-90° range. For phi, a higher number of longitudinal canals than radial canals were found, with 24.4% of the canal segments in the 67.5-90° range, compared to 18.9% in the 0-22.5° range. Overall, the network tends to be radial-longitudinal in nature (see Figures 2.3 and 2.4), with many oblique canals. The category with the highest proportion of canals was the oblique category (phi 22.5-67.5°, theta 22.5-67.5°) at 28.2%. The category with the lowest proportion of canals was the phi 0-22.5°, theta 67.5-90° group at 3.2%, which is circumferential in the plane and horizontal in the long axis. Overall the rat's cortical network is a combination of radial and longitudinal canals, with mostly oblique radial/longitudinal canals, corroborating the previous phi measurements by Britz (2012).

By contrast, the hawk (Table 2.2) has a higher number of circumferential than radial canals on the theta axis, with 47.4% falling in the 67.5-90° range, and 14.3% in the 0-22.5° range. For phi, there were a higher number of longitudinal canal segments, with 44.0% falling in the 67.5-90° range, than radial canals, with 11.1% of the canal segments in the 0-22.5° range. The category with the highest proportion of canals was the phi 22.5-67.5°, theta 67.5-90° group, at 24.7%. This category represents canals which are circumferential and oblique. The category with the lowest proportion of canals was the phi 0-22.5°, theta 0-22.5° group at 2.5%. This group represents canal segments which are radial in the plane of section. Overall, the hawk's network is heavily focused towards circumferential, longitudinal, and oblique circumferential/longitudinal canals. This fits with the laminar pattern proposed by de Margerie (2002) for wing bones in birds.

Table 2.2: Rat orientations

%	Theta 0-22.5	Theta 22.5-67.5	Theta 67.5-90	Theta total
Phi 0-22.5	6.7%	9.0%	3.2%	18.9%
Phi 22.5-67.5	19.8%	28.2%	8.7%	56.7%
Phi 67.5-90	6.0%	13.4%	5.0%	24.4%
Phi total	32.5%	50.5%	16.9%	100.0%

Table 2.3: Hawk orientations

%	Theta 0-22.5	Theta 22.5-67.5	Theta 67.5-90	Theta total
Phi 0-22.5	2.5%	3.8%	4.9%	11.1%
Phi 22.5-67.5	4.2%	16.0%	24.7%	44.9%
Phi 67.5-90	7.6%	18.6%	17.8%	44.0%
Phi Total	14.3%	38.3%	47.4%	100.0%

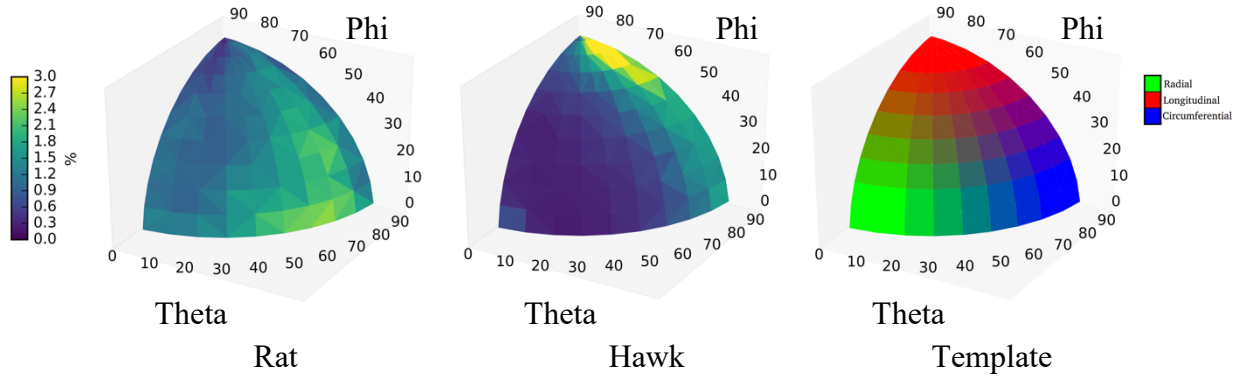

Figure 2.3: 3D maps of canal segment orientation in each specimen, with each canal's orientation visualized as a point on a quarter sphere. The left (Rat) and middle (Hawk) images are 3D heatmaps of the canal orientation in each specimen. Phi runs from 0° (transverse) to 90° (longitudinal). Theta runs from 0° (radial) to 90° (circumferential). On the right is a template showing which region represents which orientation type.

Image visualization of the lineset data serves two purposes - it helps communicate results and it helps verify that the macro has classified canals accurately. Figure 2.3 shows 3D heatmaps of the canal orientation in each specimen. Heatmaps like this allow for visualization of how the two angles vary together. Using the linesets produced by the macro, we can render each of the nine 22.5° categories of canals separately and assign them separate colours (shown in figure 2.4).

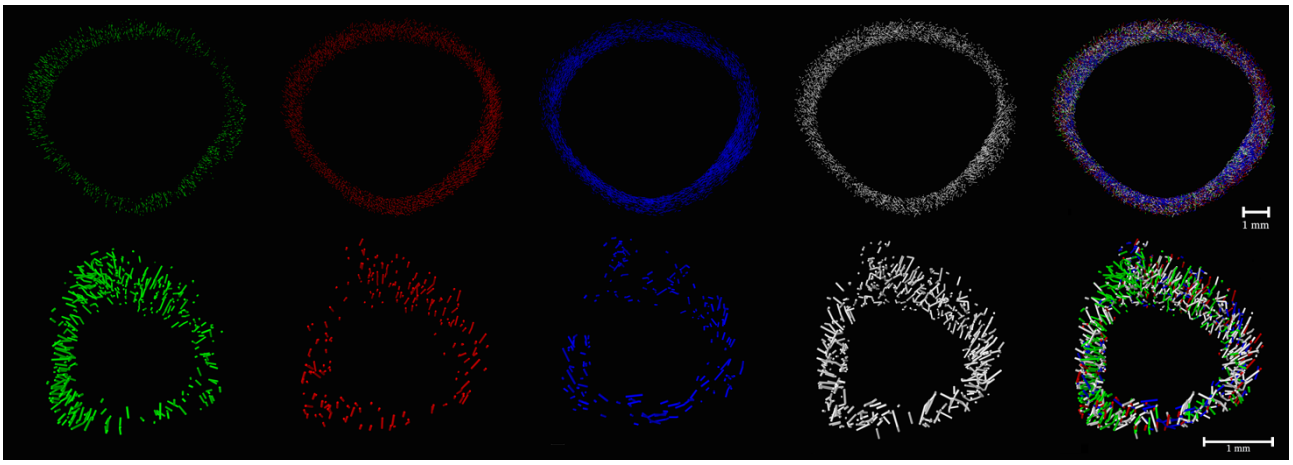

Figure 2.4: Canal network render – top row shows the hawk; bottom row shows the rat. Radial canals are rendered in green, longitudinal canals in red, circumferential canals in blue, oblique canals in white. The first four panels show only a single category, while the fifth (rightmost) shows all the canals.

This method has the potential for applications to numerus problems in cortical bone biology. The orientation of cortical canals may play a significant mechanical role in cortical bone, but more research is needed to clarify its role. This method offers the chance to do new experiments on the relationship between bone strength, bone stiffness, and canal orientation in both human and animal bone. Gocha and Agnew (in press) found that the spatial distribution of osteons was different throughout the human femur, and that this may be linked to the differential patterns of strain on the bone. Similarly, this method could be used in the future to identify patterns of different canal orientations in bones. Using micro-CT, small animals such as rats can be scanned *in vivo* (Pratt et al., 2015) and their canal networks examined. This offers the possibility of longitudinal experiments studying the development of the canal network and the orientation of the canals within it across the lifespan of an animal. Animal models in rats that affect cortical bone canals include immobilization, calcium restriction, and fatigue loading (Harrison & Cooper, 2015); as well as large numbers of different pharmacological treatments (Weinstein et al., 2011). The origin and potential functional nature of laminar bone in birds remains unproven (Lee & Simons, 2015), and open to new studies and evidence. Lee and Simons (2015) showed that small bat species below 100g in body size tend to be poorly vascularized, however they were only able to examine one larger bat specimen. They also note that knowledge of the cortical bone properties of bats and many other vertebrate species is sparse, and more work in this area is needed. Comparative studies are made easier by the non-destructive nature of our technique, allowing for easier access to specimens and museum loans. Comparisons between multiple bones of the same species and across many species are necessary if a connection between cortical canal orientation and mechanical loading is to be conclusively shown in birds. Comparisons with terrestrial and other flying vertebrates would be informative as well. Results from this avenue of research could also have applicability to the study of the origins of birds in the fossil record, and the interpretation of dinosaur activity (Padian, Werning & Horner, 2016).

2.4 Conclusions

Using micro-CT, we have shown that it is possible to measure the orientation of cortical vascular canals in a bone non-destructively. Our method has several advantages compared to histology: it is non-destructive; it is less labour intensive; it can capture information for a much greater number of canals; and it is a true measure of the 3D orientation of a canal. The nature of micro-CT imaging means that whole bones can be imaged without sectioning. This makes obtaining rare samples much easier as there is no risk of damage to the tissue, and no loss of tissue during preparatory procedures. Preparing samples for micro-CT involves no more than positioning them on the stage in the imaging apparatus, although proper capture and reconstruction of the micro-CT data does require some expertise. Because of the 3D field of view of the imaging system, we capture canals through multiple slices, as compared to a single or series of histological section(s). There are two main consequences of this - first, we can collect data for a much greater number of canals, since we capture data for a block of bone, rather than a single section; and second, we

measure the true orientation of each canal, rather than an interpreted angle measured based on the intersection between a canal and the histological section.

The growth and development of cortical bone porosity and its impact on factors such as bone strength and bone quality are relatively unexplored areas in the study of bone. Our method provides a new tool to examine the impact of the orientation of cortical bone canals on bone strength and explore the origins of cortical canals formed during modelling and remodeling.

Chapter 3. Interpreting the three dimensional orientation of vascular canals and cross-sectional geometry of cortical bone in birds and bats.

This chapter has previously been published as: Pratt, I.V. et al., 2018. Interpreting the three-dimensional orientation of vascular canals and cross-sectional geometry of cortical bone in birds and bats. J Anat, 14(Pt 5), p.S13 and is reprinted here with permission from the publisher (see appendix).

3.1. Introduction

Bone is a complex tissue, with many functions in the body. In particular, cortical bone and the porosity inside it are important factors in the overall strength of a bone (Ammann & Rizzoli, 2003; Cooper et al., 2016). In cortical bone microstructure, the pattern seen in the arrangement of the vascular canal network is thought to occur in response to growth as a juvenile, functional adaptation to use during life, and maintenance and metabolic needs throughout life. These signals are of great interest in using bone as a tool for analyzing the life history of vertebrates (de Ricqlès et al., 2000; Cubo et al., 2008; Marelli & Simons, 2014; Mitchell & van Heteren, 2015), and for reconstructing behaviour of extinct vertebrates (Seymour et al., 2012; Padian, Werning & Horner, 2016). As a biological system, the overlap of distinct factors on the same tissue creates confounding effects that interfere with a clear analysis. This presents challenges in deciphering what any given pattern may mean.

The vascular canal network in cortical bone initially develops during the primary formation of bone. During this process bone is either rapidly deposited as woven bone or more slowly as lamellar bone. In lamellar bone, large vascular spaces are present during the initial development of the bone. As the tissue ossifies it surrounds the spaces, filling them in to become primary osteons. (Maggiano, 2012) In humans and many other larger animal species, bone undergoes a controlled process of renewal called remodeling, This process creates secondary osteons and the canals within them later in life.

Canals can be classified as having four main orientations: longitudinal - where the canals are parallel to the long axis of the bone, radial – where the canals are perpendicular to the tangent at the periosteal boundary, circumferential – where the canals lie parallel to the tangent at the periosteal boundary, and oblique - which fall in between the other categories. Since canals exist in three dimensions, they often do not fall exactly in each category. For example a canal can be radial in the plane of section but at an angle in the longitudinal plane. Here we followed the classification in (Pratt & Cooper, 2017), shown below in table 3.2. de Margerie (2002) created a new measurement, the index of laminarity, based on the proportion of the circumferential canal area to the total canal area examined. They looked at the orientation of vascular canals in bones of mallard ducks and found a difference between wing bones and hindlimb bones, with the wing bones

being significantly more laminar. They noted a dichotomy in the bones they studied at around 50% circumferential canals and called bones at or higher than that level 'laminar'. They proposed that this laminar arrangement was an adaptation to better resist torsional loading, the predominant loading regime in active flight (Pennycuick, 1967; Swartz, Bennett & Carrier, 1992; de Boef, 2008). Other evidence for canal orientation responding to loading patterns exists in humans (Hert, Fiala & Petrtyl, 1994; Petrtyl, Hert & Fiala, 1996) where slight deviations to longitudinal orientations of canals are thought to reflect bending as the dominant loading force, and in rats where a six month period of paralysis of a limb (removing all loading) dramatically alters the orientation of vascular canals (Britz, Jokihaara, et al., 2012). Following these lines, (Rothschild & Panza, 2007) investigated whether the degree of laminarity was a possible risk factor in bird lower limb bones with osteoarthritis, although they found no link present. If canal orientation is driven by the forces of functional loading we would expect to find similar orientation patterns in both bats and birds, with a higher laminar index in the humerus than in the femur.

The other factor which is potentially responsible for a laminar pattern in cortical bone is growth rate during development (Lee & Simons, 2015). However, a study by de Margerie (2002) showed that the orientation of primary canals in mallards was independent of growth rate. Other studies (de Margerie et al., 2004; de Boef & Larsson, 2007a) suggest that laminar bone grows more slowly, and bone with radial canals grows the fastest. De Margerie (2004) suggests that radial canals have the most detrimental effect on mechanical resistance of shear stress of all the canal orientations. Kuehn and colleagues (2017) showed that laminarity in the emu hindlimb increased with age, and they proposed that this was due to biomechanical loading as the animal increased in size. Most birds experience very rapid growth as they need to quickly acquire flight to feed themselves (Erickson, Rogers & Yerby, 2001), whereas bats experience slower growth (Kunz & Stern, 1995; Lee & Simons, 2015). Skedros & Hunt (2004) found a significantly higher laminarity index in adult turkey ulnae compared to sub-adult bones. They suggest that the change in laminarity from sub-adult to adult may be caused by loading history or by ontogenetic changes in growth rate, and that the changes in growth rate may be the stronger factor. Skedros & Hunt (2004) also measured the collagen fiber orientation (CFO) throughout the cortex and found a strong correlation between the laminar index and predominant CFO ($r = 0.735$ in subadults, $r = 0.866$ in adults, $p < 0.01$). They suggest that CFO is more closely linked to the strain distributions which can differentiate torsion from bending, and that the vascular orientation is more strongly influenced by the rate of osteogenesis. If this is the case then we would then expect to find different patterns of canal orientation between birds and bats, with bats presenting more circumferential canals as they experience slower bone growth.

Cross sectional geometric parameters describe the shape, distribution, and amount of bone present in a cross section. Measured parameters and calculated indices are known to reflect a bone's resistance to mechanical loading including torsion, bending, axial compression and tension, and local buckling (Turner & Burr, 1993). Analysis of cross

sectional geometry is a common technique in cortical bone assessment (Johnston et al., 2014) and has been used to analyze both human and non-human bone (Lieberman, Polk & Demes, 2004; Pearson & Lieberman, 2004; de Margerie et al., 2005; Marelli & Simons, 2014; Cosman, Sparrow & Rolian, in press). The principal area moment of inertia (I) reflects a bone's resistance to bending around a chosen axis. In particular, we calculated maximum and minimum principal area moments of inertia (I_{max}, I_{min}), which reflect the highest and lowest resistances of the bone. The ratio of I_{max}/I_{min} can be used to infer how even the bones experience loads in different directions, with a value of 1 representing equal loads, and values farther away from 1 reflecting more asymmetrical loading. The polar area moment of inertia (I_p) is calculated as the sum of I_{max} and I_{min}, and reflects the bone's resistance to torsional loading (Marelli & Simons, 2014). The principal section modulus is a direct measure of the strength of a bone and its resistance to bending in a specified axis. Similar to the polar area moment of inertia, we calculated the maximum and minimum (Z_{max}/Z_{min}) section moduli and a polar section modulus (Z_p), which reflects torsional strength (Johnston et al., 2014). We also calculated the buckling ratio, a measure of the instability of a bone, reflecting its ability to resist local fractures. Cortical area can be used as a measure of a bone's resistance to axial compression (Lieberman, Polk & Demes, 2004). We also quantified cortical thickness relative to the cortical area to get a measure of thickness independent of the size of the bone. Higher cortical thickness increases a bone's resistance to bending but is a less important factor than the outer diameter of a bone (Ammann & Rizzoli, 2003). However, the size of a bone is primarily driven by the size of the animal, so a comparison of a weighted cortical thickness may be more informative for determining what forces a bone is responding to. The shape of a bone is also important in mechanical strength. Elliptical bones are interpreted as having higher resistance to bending along the major axis, while more circular bones have more even bending resistance in every direction and are more resistant to torsional loading (de Margerie et al., 2005).

We hypothesized that loading environment is the most important factor in bone vascular canal orientation. We set out to test this by comparing the orientation of vascular canals in the humerus - the main bone in the wing, and the femur – the main bone in the hindlimb in active flying birds and bats. We used synchrotron computed tomography (SR Micro-CT) to produce 3D maps of the cortical networks in both groups and measure the orientation of the canals within the networks. We followed the method laid out in (Pratt & Cooper, 2017) with minor adjustments. By comparing the canal networks between wing bones and hindlimb bones we sought to determine whether the presence or absence of a pattern is related to the action of the limb. By comparing between birds and bats, the two extant actively flying vertebrate groups, we looked to see if there is a common orientation pattern present in the bones of both groups that could be a response to the shared loading pattern created by flight. If loading environment does determine canal orientation, we expected to find similar orientation patterns between the groups, and a higher laminarity index in the humerus than the femur. We also expected the humeri to be more circular, and to have higher polar section moduli than the femora. Based on this we expected to see correlations between the laminarity index and geometric parameters representing torsional resistance,

and between the longitudinal index and geometric parameters representing bending resistance.

3.2. Materials

The study incorporated 9 bat species and 22 bird species with isolated bones from 54 individuals scanned in total (see table 3.1). A scan was taken of the right humerus and right femur of each individual. The sampled bat taxa represent both of the major bat clades Yinpterochiroptera and Yangochiroptera. The bird species were chosen to cover the major groups of large birds as best as possible and include 10 orders - Accipitriformes, Anseriformes, Falconiformes, Galliformes, Gaviiformes, Gruiformes, Pelecaniformes, Psittaciformes, Strigiformes, and Suliformes. We chose the largest locally accessible species of bats and birds because bones below a certain size often have fewer canals (de Buffrénil, Houssaye & Böhme, 2008; Lee & Simons, 2015). The bat specimens were borrowed from the Department of Natural History - Mammology at the Royal Ontario Museum (Toronto, Canada). The bird specimens were borrowed from the Zooarchaeology collection in the Department of Archaeology and Anthropology at the University of Saskatchewan (Saskatoon, Canada). The bone specimens were all professionally skeletonized by boiling or dermestids and were either wild collected, obtained from local zoo collections, or donated by hunters or conservation officers. The specimens were well-preserved and there was no evidence of deterioration visible in the microarchitecture or macroarchitecture. Animal ethics approval was granted by the University of Saskatchewan Animal Research Ethics Board of the University Committee on Animal Care and Supply (protocol 2013-0114) and by the Canadian Light Source.

Table 3.1: List of specimens used. N=1 if not otherwise noted

Birds	Bats
Mallard (*Anas platyrhynchos*)	Egyptian Fruit Bat (*Rousettus aegyptiacus*) (n=4)
White-fronted goose (*Anser albifrons*)	Great Fruit-eating Bat (*Artibeus literatus*) (n=4)
Snow goose (*Anser caerulescens*)	Grey-headed Flying Fox (*Pteroptus policephalus*)
Golden eagle (*Aquila chrysaetos*)	Hairless Bat (*Cheiromles torquatus*) (n=4)
Yellow-blue Macaw (*Ara ararauna*)	Indian Flying Fox (*Pteroptus giganteus*) (n=4)
Great Blue Heron (*Ardea Herodias*) (n=2)	Large Flying Fox (*Pteroptus vampyrus*)
Short-eared Owl (*Asio flammeus*)	Lyle's Flying Fox (*Pteroptus lylei*) (n=3)
Ruffed Grouse (*Bonasa umbellus*)	Spectral Bat (*Vampyrum spectrum*) (n=4)
American Bittern (*Botaurus lentiginosus*)	Straw-coloured fruit bat (*Eidolon helvum*)
Great Horned Owl (*Bubo virginiana*) (n=3)	
Red-tailed Hawk (*Buteo jamaicensis*) (n=2)	
Rough-legged Hawk (*Buteo lagopus*)	
Swainson's Hawk (*Buteo swainsoni*)	
Turkey Vulture (*Cathartes aura*)	
Greater Sage-grouse (*Centrocercus urophasianus*)	
Common loon (*Gavia immer*)	
Whooping crane (*Grus americana*)	
Sandhill crane (*Grus canadensis*)	
Bald eagle (*Haliaeetus leucocephalus*)	
Snowy owl (*Nyctea scandiaca*) (n=2)	
American white pelican (*Pelecanus erythrorhynchos*) (n=2)	
Double-crested cormorant (*Phalacrocorax auritus*)	
Total N = 30	Total N = 24

3.3. Methods

3.3.1. Micro-CT

We used phase contrast enhanced synchrotron micro computed tomography to image our samples (Tafforeau et al., 2006; Arhatari et al., 2011). We scanned the humerus and femur at midshaft of each individual (see figure 3.1). Micro-CT imaging was performed at the BioMedical Imaging and Therapy (BMIT) beamlines(Wysokinski et al., 2007; 2015), part of the Canadian Light Source (CLS) synchrotron facility. We used both the bend magnet (BM) and insertion device (ID) beamlines which comprise the BMIT facility, depending on availability. Imaging quality was comparable between the two beamlines, however scanning using the ID beamline was much faster due to its higher X-ray flux, and the ID beamline has a taller field of view. Both beamlines were used with the same camera/detector set-up. We used a Hamamatsu C9300-124 optical camera paired with the

Hamamatsu A40 x-ray converter to take projection images with an effective pixel size of 4.3 μm at 32 keV. This camera gives a field of view (FOV) of 11 mm in width. Many of the bones in the sample have a shaft diameter greater than 11 mm requiring a larger FOV. We used two methods to overcome this limitation. By moving the center of rotation of the scan and rotating through 360° the FOV can be increased up to 18-19 mm. Alternatively, the camera can be offset so that two projection images are taken and stitched together for each rotation step. Because of the wide FOV provided by the open gantry micro-CT system at BMIT, we were able to scan our specimens completely non-destructively. The height of the FOV was 2 mm on the BM and 4 mm on the ID beamline. Each specimen was scanned with exposure times ranging from 0.5–1.5 s per projection. The exact exposure time depended on the synchrotron beam ring current, which decays from a peak of 250 mA over time. Flat and dark frames were collected before each scan to correct for noise in the detector and the x-ray beam. An Aluminum filter with an effective thickness of 1.1 mm was used to eliminate any stray low energy harmonics. Our scans were optimized for in line phase contrast using a propagation distance of 50 cm.

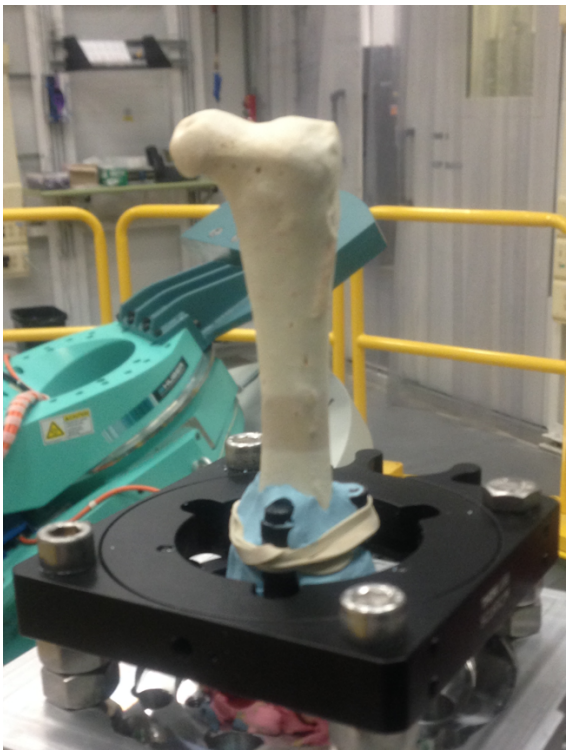

Figure 3.1: This image shows an example of sample mounting at the beamline. Pictured here is an American white pelican femur. Each specimen was mounted using a self-centering mount and secured with modeling clay so that the shaft of the bone was stable in the field of view of the detector. On this sample discoloration on the surface of the cortex is visible from the area scanned.

3.3.2. Image Processing

The main steps in the image processing are illustrated in figure 3.2. A custom software package was developed using the ImageJ (ImageJ, NIH) scripting platform to perform most of the data processing. The micro-CT projections were initially processed to correct for detector and beam noise using flat and dark projections, and reconstructed using NRecon (Bruker SkyScan, Kontich BE), a commercial software package. NRecon provides graphics card acceleration, allowing for rapid reconstruction of large data sets. We used Amira (FEI Company, USA) to perform the main data processing – thresholding, segmenting, and skeletonizing the reconstructed micro-CT slices to extract the canal network from the bone as a lineset. Our analysis closely follows the method described in (Pratt & Cooper, 2017).

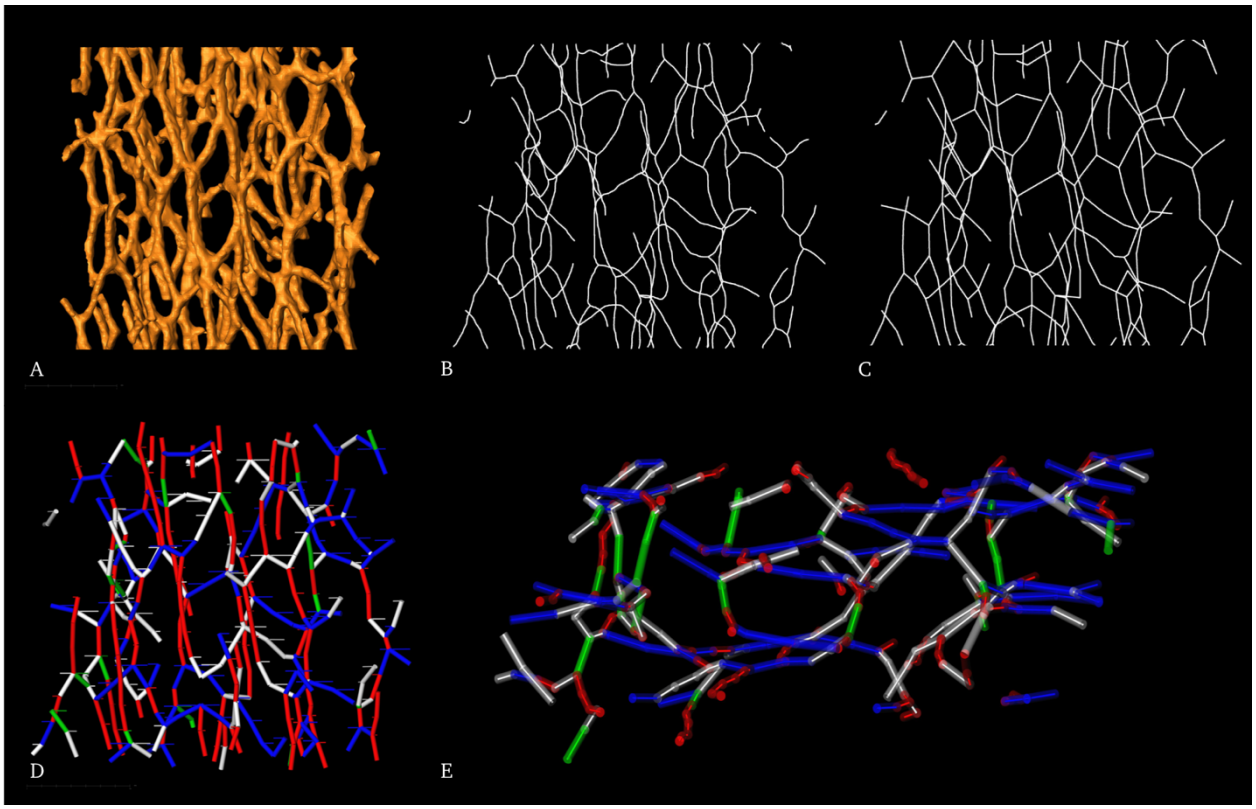

Figure 3.2: Processing steps for data analysis using a small ROI selected from the humerus scan of a Swainson's hawk. Images A, B, C, and D are longitudinal sections parallel to the endosteal surface. The initial canal render is shown in A, followed by the skeleton in B, and the subsampled network in C, clearly illustrating the close preservation of the original orientation of the canal segments. The images in D and E show the measured 3D orientation categories of the canal segments (thick lines) and their projected 2D analogues (thin lines). Here red represents longitudinal canals, green represents radial canals, blue represents circumferential canals, and white represents oblique canals. Image E is a transverse section, looking top down, and shows that the 2D analogues have the same orientation in the transverse section as the original 3D canal segments.

Each canal lineset was initially processed to identify branch points in the canal network and subsample the network into a series of line segments of a defined length. This allows for better measurement of the variability of orientation in the network, especially of curved canals. We used a distance of 23 pixels (100 μm), roughly the equivalent of a standard histological slice. We measured the position of the bone's centroid in each slice, and measure the three dimensional orientation of each line segment in the subsampled network relative to the position of the centroid. Two angles are measured, theta and phi. Phi measures the angle between a canal segment and the long axis of the bone, and is used to determine whether a canal is longitudinal. Theta measures the angle between a canal and a line from the bone centroid to midpoint of that canal. Theta is used to differentiate between radial and circumferential canals. By using both angles we were able to fully

differentiate between all four bone categories, including oblique canals. This allows us to classify whether each line segment is longitudinal, radial, or circumferential. We classified canal segments following the criteria in (de Margerie, 2002; Pratt & Cooper, 2017) as shown in table 3.2. In contrast to the method shown earlier in (Pratt & Cooper, 2017), we weighted the orientation measure by the three dimensional length of each line segment, so that shorter line segments (those segments under 100 μm) that are less than the separation distance have less effect on the overall measures of the scan. We then calculated the laminar, radial, and longitudinal indices as the ratio of the sum of the length of all the circumferential, radial, or longitudinal canal segments over the total length of all canal segments (see equation 3.1). We use canal length instead of the canal area measure used by de Margerie (2002) since the length more accurately reflects the proportions of canals in the network than area, which underestimates longitudinal canals. Canal length is a 3D measure that we can measure with micro-CT but cannot be measured in histology. In order to see how the 3D measure performs against traditional two dimensional methods such as histology we performed a kind of pseudo two dimensional measurement on the same micro-CT scans. In the orientation measurement, instead of using the full canal segment length we used the projected 2D length in the cross sectional plane.

Table 3.2: Canal categories

Canal category	Phi	Theta
Longitudinal	67.5 - 90	0 – 90
Circumferential	0 – 67.5	67.5 – 90
Radial	0 – 67.5	0 – 22.5
Oblique	[0 – 22.5, 67.5 – 90],[22.5-67.5]	[22.5 – 67.5],[0 – 90]

$$Laminar\ index = \frac{\sum CanalSegmentLength_{circumferential}}{\sum CanalSegmentLength_{all}}$$

Equation 3.1: Laminar index calculation. Calculations for radial and longitudinal indices are analogous.

3.3.3. Cross-sectional geometry

The middle slice of each scan was selected for analysis using cross sectional geometry metrics. The slices were masked and the porosity filled in. Custom algorithms (Matlab, MathWorks, Natick, MA, USA) were used to measure the geometric parameters and strength indices. The metrics measured included the ratio of principal maximum and minimum area moments of inertia (I_{max}/I_{min}), polar area moment of inertia (I_p), the ratio of principal maximum and minimum section moduli (Z_{max}/Z_{min}), polar section modulus

(Z_p), buckling ratio (BR), cortical thickness (t_c), cortical area (a_{cort}), and circularity. In order to account for differences in size we created a cortical thickness index defined as the ratio of cortical thickness over cortical area.

Principal area moments of inertia were calculated based on traditional methods, with the polar area moment of inertia calculated as the sum of the minimum and maximum area moments of inertia. Principal section moduli were calculated by dividing the equivalent principal area moment of inertia by the corresponding maximum distances to the outer periosteal edges from the principal neutral axes. The polar section modulus was defined following (Johnston et al., 2014) by dividing the polar area moment of inertia by the maximum outer radius of the bone. The buckling ratio was calculated as the ratio of total area to cortical area (Sievänen et al., 2016). Cortical thickness was measured using the unrolling approach (Johnston et al., 2014). Circularity was defined as the ratio of the total bone area to the area of the smallest inscribing circle (Zebaze et al., 2005).

Statistical analysis was performed with SPSS version 24 (IBM, USA). We used repeated measures two-way MANOVAs to compare the three orientation indices, the geometric parameters, and the strength indices between the two taxonomic groups and the two bones for both the 3D and the pseudo-2D data. A one-way repeated measures ANOVA was used to compare the pseudo-2D and 3D results. Linear regression analysis was used to look for correlations between geometric and strength parameters and orientation indices.

3.4. Results

Descriptive statistics are shown in table 3.3 for the 3D measurements. The comparison between birds and bats is shown in table 3.4 and the comparison between humerus and femur is shown in table 3.5 for both the 3D and pseudo-2D methods. We consider a p-value of less than 0.05 as statistically significant, and all p-values are shown in the tables. The comparison between the two measurement methods is shown in table 3.6. For the main 3D analysis, we found that birds have a higher laminar index than bats in the humerus and femur. The birds also had a lower radial index in the humerus and a lower longitudinal index in the femur. The results for the pseudo-2D analysis mirrored these findings.

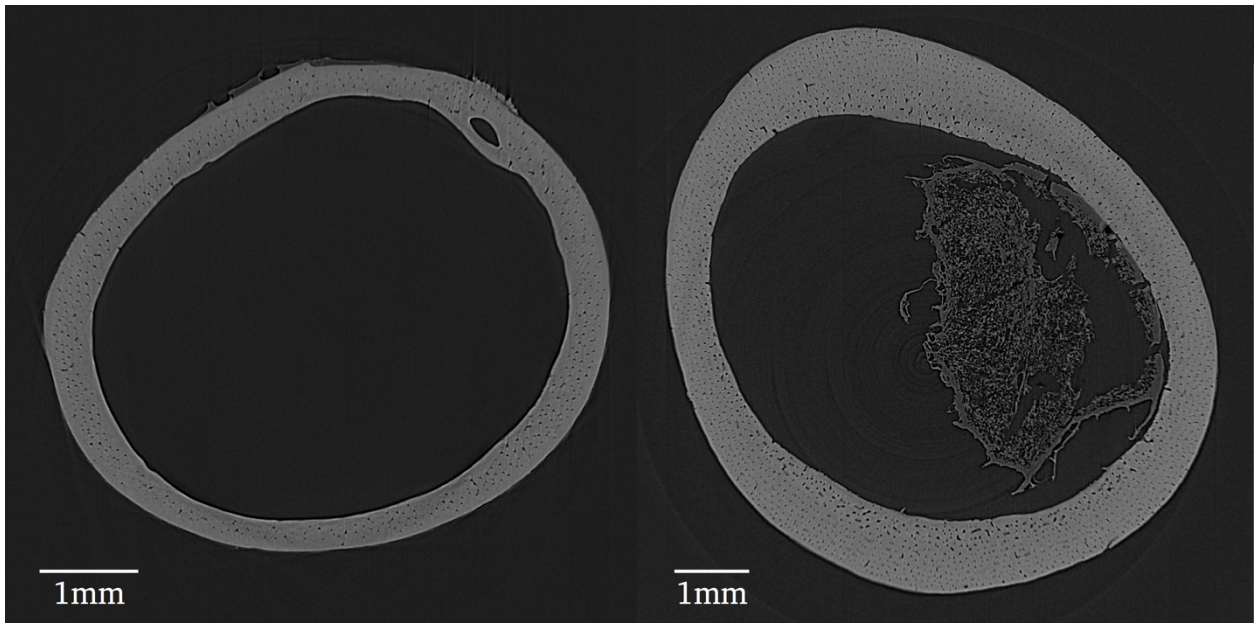

Figure 3.3: Bird micro-CT scans. Both images show relatively thin cortices with full vascularization. Right side is a Swainson's hawk Humerus, left side is a Snowy owl humerus.

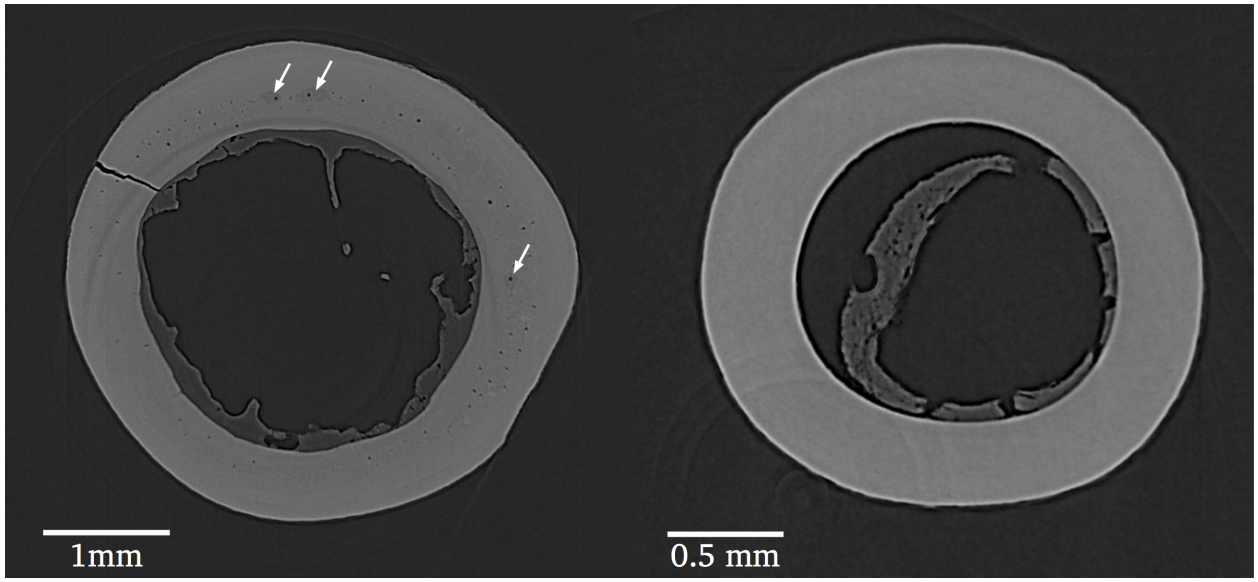

Figure 3.4: Bat micro-CT scans. Note the relatively thick cortices with typical low vascularization. Complete absence of vascularization can be seen in the right cortex. Some evidence of secondary remodeling can be seen in the cortex on the left (white arrows). Right side is a Grey-headed flying fox femur, left side is a Spectral bat femur.

Table 3.3: Descriptive statistics for the 3D measurement style.

Variable	*Tax group*	*Bone*	*Mean*	*Std. D.*
3D Laminar Index	Birds	Humerus	0.183	0.057
		Femur	0.232	0.075
	Bats	Humerus	0.118	0.115
		Femur	0.119	0.118
3D Radial Index	Birds	Humerus	0.218	0.064
		Femur	0.243	0.080
	Bats	Humerus	0.309	0.185
		Femur	0.273	0.196
3D Longitudinal Index	Birds	Humerus	0.471	0.093
		Femur	0.383	0.094
	Bats	Humerus	0.507	0.201
		Femur	0.537	0.239
Z_p	Birds	Humerus	94.321	80.976
		Femur	10.211	49.33
	Bats	Humerus	57.499	10.126
		Femur	3.499	3.955
I_p	Birds	Humerus	589.053	696.29
		Femur	27.734	348.78
	Bats	Humerus	307.387	36.561
		Femur	6.951	10.558
Buckling ratio	Birds	Humerus	6.545	1.646
		Femur	3.722	1.1822
	Bats	Humerus	6.993	0.4745
		Femur	3.464	0.4723
I_{max}/I_{min}	Birds	Humerus	1.434	0.1627
		Femur	1.277	0.1646
	Bats	Humerus	1.218	0.1858
		Femur	1.314	0.1805
Z_{max}/Z_{min}	Birds	Humerus	1.241	0.093
		Femur	1.145	0.0866
	Bats	Humerus	1.097	0.0974
		Femur	1.149	0.0757
Cortical thickness index	Birds	Humerus	0.039	0.014
		Femur	0.104	0.0181
	Bats	Humerus	0.046	0.0296
		Femur	0.163	0.0568
Circularity	Birds	Humerus	0.811	0.0491
		Femur	0.828	0.0623
	Bats	Humerus	0.828	0.0557
		Femur	0.812	0.0782

Table 3.4: Comparison between birds and bats. A positive mean difference means the birds are have a higher value than the bats.

Variable	*Bone*	*Mean difference*	*Std error*	*sig*
3D Laminar Index	Humerus	0.059	0.027	0.031
	Femur	0.121	0.028	0.000
3D Radial Index	Humerus	-0.113	0.034	0.002
	Femur	-0.049	0.043	0.267
3D Longitudinal Index	Humerus	-0.010	0.039	0.791
	Femur	-0.147	0.052	0.007
Pseudo-2D Laminar Index	Humerus	0.090	0.037	0.018
	Femur	0.148	0.038	0.000
Pseudo-2D Radial Index	Humerus	-0.166	0.038	0.000
	Femur	-0.079	0.045	0.091
Pseudo-2D Longitudinal Index	Humerus	-0.024	0.030	0.421
	Femur	-0.165	0.046	0.001
Z_p	Humerus	80.577	18.391	0.000
	Femur	50.861	10.871	0.000
I_p	Humerus	544.293	158.423	0.001
	Femur	280.055	75.549	0.001
Buckling ratio	Humerus	2.912	0.368	0.000
	Femur	3.477	0.252	0.000
I_{max}/I_{min}	Humerus	0.195	0.042	0.000
	Femur	-0.085	0.051	0.105
Z_{max}/Z_{min}	Humerus	0.126	0.023	0.000
	Femur	-0.048	0.025	0.059
Cortical thickness index	Humerus	-0.060	0.007	0.000
	Femur	-0.109	0.012	0.000
Circularity	Humerus	-0.018	0.014	0.190
	Femur	0.012	0.019	0.525

Table 3.5: Comparison between humerus and femur. A positive mean difference means the humerus has a higher value than the femur.

Variable	*Tax group*	*Mean Difference*	*Std. Error*	*Sig.*
3D Laminar Index	Birds	-0.040	0.018	0.035
	Bats	0.022	0.022	0.304
3D Radial Index	Birds	-0.032	0.027	0.255
	Bats	0.033	0.032	0.315
3D Longitudinal Index	Birds	0.085	0.033	0.013
	Bats	-0.051	0.039	0.196
Pseudo-2D Laminar Index	Birds	-0.034	0.027	0.211
	Bats	0.024	0.032	0.445
Pseudo-2D Radial Index	Birds	-0.026	0.031	0.400
	Bats	0.062	0.036	0.095
Pseudo-2D Longitudinal Index	Birds	0.062	0.029	0.037
	Bats	-0.079	0.034	0.024
Z_p	Birds	37.217	5.821	0.000
	Bats	7.501	6.888	0.282
I_p	Birds	288.068	60.160	0.000
	Bats	23.829	71.182	0.739
Buckling ratio	Birds	-0.341	0.228	0.141
	Bats	0.224	0.269	0.409
I_{max}/I_{min}	Birds	0.213	0.042	0.000
	Bats	-0.068	0.050	0.180
Z_{max}/Z_{min}	Birds	0.146	0.023	0.000
	Bats	-0.028	0.027	0.301
Cortical thickness index	Birds	-0.007	0.004	0.078
	Bats	-0.055	0.004	0.000
Circularity	Birds	-0.012	0.014	0.387
	Bats	0.018	0.017	0.274

Table 3.6: Comparison between pseudo-2D method and 3D method.

Measure	*Mean Difference*	*Std. Error*	*Sig.*
Laminar Index	0.077	0.004	0.000
Radial Index	0.094	0.005	0.000
Longitudinal Index	-0.209	0.005	0.000

We also found that in birds the humerus had a lower laminarity index than the femur and a higher longitudinal index. In contrast, the pseudo-2D method found only significant differences in the longitudinal index, with the humerus higher than the femur in the birds and lower in the bats. We found differences between the two methods for all three measures, with the laminar and radial indices higher in the pseudo-2D measure, and the longitudinal index lower. In both the birds and the bats, the overall highest category of canals was longitudinal, then radial, and lowest was laminar.

In the cortical bone geometrical parameters we found several differences. Both the Z_p and I_p were higher in birds compared to bats in both the humerus and the femur, and higher in the humerus than the femur in birds. The buckling ratio was higher in birds than in bats in both the humerus and the femur. We found that I_{max}/I_{min} and Z_{max}/Z_{min} were both higher in birds than in bats in the humerus. I_{max}/I_{min} and Z_{max}/Z_{min} were also both higher in the humerus than in the femur in birds. Using the cortical thickness index we found that bats were thicker than birds in both the humerus and the femur, and that the femur was thicker than the humerus in bats. We found no correlations between the geometric parameters representing torsional resistance and the laminarity index, and no correlations between the geometric parameters representing bending resistance and the longitudinal index.

3.5. Discussion

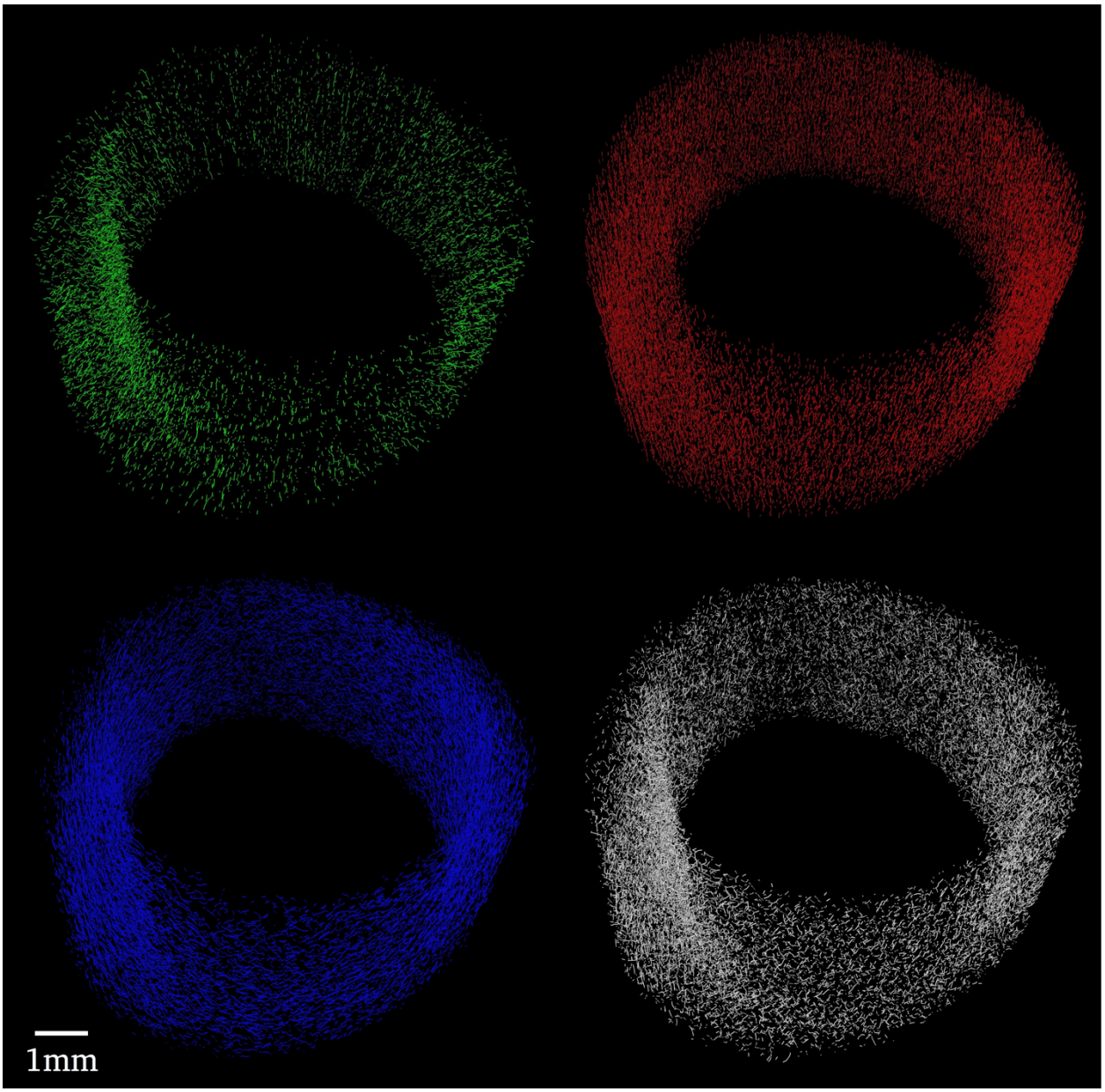

Figure 3.5: 3D renders of canal segments in a Swainson's hawk humerus with circumferential shown in blue, longitudinal shown in red, radial shown in green, and oblique shown in white.

The traditional method for studying cortical bone porosity has been undecalcified bone histology. Micro-CT is a relatively new technique (Feldkamp et al., 1989) that has increasingly been applied to cortical bone microstructure. In comparison to histology, micro-CT is "less destructive" – depending on the system and sample it can be completely non-destructive, as in our case. Non-destructive imaging methods preserve the specimens

for future analysis and make obtaining access to rare materials much easier. Micro-CT is typically lower resolution than histology – only the highest resolution scans are able to capture osteon boundaries (Arhatari et al., 2011; Cooper et al., 2011; Maggiano et al., 2015; Andronowski, Pratt & Cooper, 2017). This means most micro-CT scans are not able to differentiate primary from secondary canals. Scan quality varies drastically between micro-CT systems, and the best systems are available only at synchrotron research facilities, where research time is limited; However, the fundamental advantage of micro-CT is it is able to capture the full 3D vascular canal network in a complete bone, and the ability to capture many more canals than are present in a single histological slice. This study is the first to use micro-CT to test hypotheses about canal orientation in 3D. Previous studies on canal orientation using micro-CT have only been able to differentiate between longitudinal canals and transverse canals (Britz, Jokihaara, et al., 2012; Jast & Jasiuk, 2013), and have not had the ability to differentiate between radial and circumferential canals until (Pratt & Cooper, 2017). Our study relied on the synchrotron system to provide a wider field of view than most laboratory based micro-CT systems, allowing the imaging of the full bone cross section non-destructively. Previous studies have used histology and attempted to infer a 3D orientation (de Boef & Larsson, 2007a), but this approach is flawed by the assumptions required to generate the measurement. They fit an ellipse into each canal space and if the minor axis is equal to or greater than 95% of the major axis assume the canal is longitudinal. This relies on the assumption that canals are very circular in cross-section, an assumption that is not always true (Hennig et al., 2015). A more fundamental problem in the histological method of analysis is the underestimation of longitudinal canals. The method used by most studies (Rensberger & Watabe, 2000; de Margerie, 2002; Skedros & Hunt, 2004; Cubo et al., 2005; de Margerie et al., 2005; de Boef, Larsson & Horner, 2007; Marelli & Simons, 2014; Lee & Simons, 2015) creates a laminarity index based on the proportion of circumferential canal area out of total canal area. In a histological slice, the area of longitudinal canals measured is underestimated as only a small cross section of the canal is measured, as opposed to a transverse section of circumferential or radial canals. This affects the accuracy of any calculations relying on a 'total canal area' metric.

We found that the bat species typically have thick cortices with inconsistent vascularization containing few canals typically concentrated into clusters. The birds have thin cortices tightly packed with canals (see figure 3.3). The bats had a significantly higher cortical thickness index than the birds in both the humerus and the femur. The bats had thicker cortices in the femur than in the humerus, while there were no differences in cortical thickness between the bones in the birds. Our results indicated that both the birds and the bats were both very circular (close to 1), with no differences between the groups or the bones. This indicates that both bones are adapted to torsional loading. We found a significantly higher buckling ratio in the birds than in the bats, and no differences between the humerus and the femur. This indicates a higher resistance to local fractures in the bird's bones. This may be due to the thinner cortices in these animals. We found a significantly higher I_p and Z_p in the birds than in the bats, and a significantly higher I_p and Z_p in the bird humeri than in the bird femora. These results suggest that the birds have a

greater torsional resistance than the bats, and that the humeri in birds have greater torsional resistance than the femora. I_{max}/I_{min} and Z_{max}/Z_{min} were significantly higher in bird humeri than in bat humeri. I_{max}/I_{min} and Z_{max}/Z_{min} were also higher in the humerus than the femur in birds. These differences indicate that the birds and the bats are experiencing different loads across the major and minor axes. Overall these data reinforce the idea that the humerus is more adapted to torsional stresses, and suggest that the bird bones have a greater resistance to torsional stress than the bats.

In four bat bones (3 femora and 1 humerus), the cortices were found to be completely absent of vascular canals in the area of the scan (see figure 3.4). Previous studies have noted that bats tend to be poorly vascularized or avascular (Foote & Hrdlicka, 1916; Enlow & Brown, 1958; Bennett & Forwood, 2010; Lee & Simons, 2015). Monitor lizards are also known to have inconsistent vascularization, with cortices that can be completely free of vascular canals. de Buffrenil & colleagues (2008) examined the canal orientation and cortical porosity density in these animals. They found that the presence of canals requires a certain body size, and that canal orientation was a variable feature independent of growth rate. Lee & Simons [2015] propose that the absence of fully vascularized tissue indicates that bats do not have laminar bone and that bone shape is more important in determining torsional resistance. They gave a laminar index of 0 or N/A for all the bats in their sample. We had one specimen in our sample (*Pteroptus vampyrus*) of a species present in their sample, and we measured a laminar index of 0.049 in its humerus. Part of the reason for this may be due to the problems with the histology measurement method used. Since the bats have few canals, any single plane of section may not accurately reflect the full pattern present in the whole bone. Our results show that although the bats have fewer canals overall and they have a significantly lower laminar index than the birds, they do still contain circumferential canals. The clear differences found between the more laminar birds and the bats is in line with the results found by Lee & Simons (2015). The bats do not have enough circumferential canals to call the bone 'laminar'.

While de Margerie (2002) set a value of 0.5 for the laminar index as a determinant of laminar bone, none of the bones we scanned had a value that high. Our laminarity index values are much lower than those found by de Margerie (2005) who measured laminarity indices of 0.625 for the humerus and 0.563 for the femur in a sample of 22 birds. Lee & Simons (2015) measured laminarity indices averaging 0.331 overall for humeri of 15 birds, much closer to the values reported here. We found that the bird humeri had an average laminarity index of 0.183, the bird femora an average of 0.232, the bat humeri an average of 0.118, and the bat femora an average of 0.119. In our previous article (Pratt & Cooper, 2017) we measured a laminar index of 0.119 in a rat tibia, well below the mean laminar index for the birds in both humeri and femora. In our comparison, the laminar and radial indices were higher by 0.077 and 0.093 in the pseudo-2D measures ($p < 0.001$) while the longitudinal index was significantly lower by 0.210 ($p < 0.001$). This indicates that traditional methods are underestimating the amount of longitudinal canals by 21%, and that previously reported values for laminarity indices may not be reliable.

Several studies have shown that the growth rate of bone differs between the long bones, (Castanet et al., 2000; Starck & Chinsamy, 2002; de Margerie et al., 2004) with higher growth rates in the hindlimb, and between species, with bats growing slower than birds. De Margerie (de Margerie et al., 2004) suggests that laminar bone is the slowest growing. Skedros & Hunt (2004) found a significantly higher laminar index in adult turkey ulnae compared to sub-adults. They attributed part of this difference to changes in growth rate throughout the lifespan of the animal. We found a significantly higher laminar index in the femur than in the humerus, which could indicate a prioritization of laminar bone over growth rate in the femur or a prioritization of growth rate over laminar bone in the humerus. Our findings contradict what we expected based on the literature. Previous studies (de Margerie, Cubo & Castanet, 2002; de Margerie et al., 2005; de Margerie & Rakotomanana, 2007; Lee & Simons, 2015) have all shown a higher laminar index in the humerus than in the femur. While our 3D results show the opposite of this, a higher laminar index in the femur than in the humerus, the pseudo-2D measurement shows no difference in the laminar index between the two bones. The pseudo-2D measure found differences in the longitudinal index between the bones in both groups, while the 3D comparison also found a significant difference in the longitudinal index between the humerus and femur in the birds. This indicates that at least part of the disparity between our results and those in the literature originate in the analysis method, with not enough canals measured in the bones and the underestimation of longitudinal canals. Another potential explanation for the differences could be high variance in canal orientation between individuals of the same species and between species. The orientation measurements in the bats have relatively high standard deviations (on the same order of magnitude as the means for each group). Our sample contains many different species but few (1-4) individuals per species. The sample contains both female and male individuals, and there is no research on sex differences in cortical canal orientation. Overall our orientation results run counter to expectations and taken together with the cortical geometry data which shows higher torsional strength in the humerus than in the femur, our results do not support the hypothesis that laminar bone is a response to torsional loading in the wing bones.

In our study we were unable to determine when the patterns seen in the microstructure develop. The micro-CT scans we used are unable to differentiate between primary and secondary canals, so we were unable to say whether the patterns developed early in life during development or later in life through remodeling. Several of the bat scans show large voids in the cortex which are likely remodeling events, and some of the scans show mineralization differences indicating osteon boundaries which are typical of secondary canals (See Figure 3.4 for an example in bats). Birds are known to go through remodeling in maturity and we found some evidence of osteon boundaries in our scans as well. If higher laminarity appears only after flight behaviour manifests, that would be evidence supporting the hypothesis that laminar bone is a response to functional loading. If laminar canals appear during early development, it would require more insight to determine if they were a response to growth or to an evolutionary pressure for increased resistance to torsional loading. The best avenue for determining this is by way of longitudinal studies

on canal orientation, which to the best of our knowledge have never been performed. Previous research in our lab has shown that *in vivo* micro-CT can be applied to image cortical canals in live rats (Pratt et al., 2015). It would be of great interest to apply this technique to a bird model, to determine how the microstructure develops in 3D during ontogeny, and especially across the point of acquisition of flight.

3.6. Conclusion

Highly vascularized bird cortices and poorly vascularized bat cortices showed clearly different patterns of vascular canal orientation. While both groups face similar mechanical loads on their wing bones, they seem to have found different strategies to adapt to them. Overall it remains difficult to fully assess whether a higher laminar index is a response to loading or growth rate, however, this study does not find support for the functional loading hypothesis. Studies seeking to interpret the behaviour of extinct species should be wary of the incomplete state of knowledge in this area and the limitations of histological analysis.

We recommend that any studies of vascular canal orientation use micro-CT rather than histology, to avoid the issue of underestimation of longitudinal canals and to measure instead of infer the theta angle. This study and our previous technical article (Pratt & Cooper, 2017) form a strong basis for how to proceed with micro-CT analysis of vascular canal orientation.

Future studies should investigate the development of canal orientation throughout the lifespan of the target species, with particular interest in the time period of the acquisition of adult locomotor behavior. *In vivo* micro-CT imaging provides an excellent opportunity for the acquisition of such data.

Chapter 4. The effect of growth rate on the three dimensional orientation of vascular canals in the cortical bone of broiler chickens.

This chapter has previously been published as: Pratt, I.V. and Cooper, D.M.L., 2018. The effect of growth rate on the three-dimensional orientation of vascular canals in the cortical bone of broiler chickens. J Anat. doi:10.1111/joa.12847 and is reprinted here with permission from the publisher (see appendix).

4.1. Introduction

Cortical bone is a major component of the strength of a bone. In particular, the porosity within cortical bone is important in developing the asymmetrical strength required by each bone's particular functional requirements (Currey, 2002; Ammann & Rizzoli, 2003; Cooper et al., 2016). The cortical canal network forms initially during the primary formation of a bone. In fibrolamellar bone, vascular spaces incorporated from the periosteum are closed in by deposition of layers of lamellar bone. Over time these spaces are filled in leaving a network of connected primary canals, or primary osteons (Maggiano, 2012). In humans and most larger animals, bone is continually renewed through the turnover of bone tissue in a process known as remodeling. Remodeling bores new canals through bone which are then filled in with new 'secondary' bone, creating the structures known as secondary osteons.

The orientation of cortical canals, both primary and secondary, is a useful signal in bone microstructure, but its full etiology is not clear. In a long bone, the orientation of a canal can be either longitudinal, meaning parallel to the long axis of the bone; radial, oriented like rays emanating from the centroid, like spokes on a bicycle wheel; circumferential, meaning parallel to the circumference, like the orbit of a planet; or oblique, falling between the other categories. Measuring the proportion of one category of canal orientations to all the canals gives indices, the most common of which is the laminar index popularized by de Margerie et al. (2002) after de Ricqles et al. (1991). de Margerie et al. (2002) defined the laminar index as the proportion of circumferential canal area to total canal area as measured in 2D histological sections. Canal orientation is thought to be related to both functional loading and growth, with primary canals reflecting the situation during the initial growth phase and secondary canals reflecting later life periods. Secondary canals can yield more mixed signals as the loading experienced by a bone may change in later life and the remodeling process may not overwrite all canals from earlier life so canals from a previous period can confound measurements.

A link between functional loading and canal orientation was proposed by Hert et al. (1994) and Petrtyl et al. (1996) who suggested that longitudinal canal orientations in the human femur optimized resistance to bending forces, and by de Margerie et al. (2002) who proposed that circumferential canals in mallard duck wing bones helped resist torsional

forces created by flight and showed that mallards had a significantly higher laminar index in the wing bones than in the hindlimb bones. Evidence from rats (Britz, Jokihaara, et al., 2012) showed that a 6 month period of paralysis-induced disuse in a rat hindlimb drastically changes the canal orientation pattern in the tibia. de Margerie et al. (2002) also found no significant relationship between canal orientation and bone growth rate in mallard long bones. de Margerie et al. (2004) suggested that radial canals have the lowest mechanical resistance to shear stress of all the canal orientations and circumferential canals the highest. We previously found a higher laminar index in the femur than the humerus in a comparative study of birds and bats (Pratt et al., 2018) a result that does not support a link between functional loading and canal orientation.

The other potentially significant factor relating to differences in canal orientation is growth rate. Studies in king penguin chicks (de Margerie et al., 2004) and in *Tyrannosaurus rex* (de Boef, Larsson & Horner, 2007) found relationships between growth rate and vascular canal orientation with bone with more radial canals growing faster and bone with more circumferential canals (corresponding to a higher laminar index) growing slower. Skedros & Hunt (2004) found a significantly higher laminar index in adult turkey ulnae compared to sub-adult bones. They suggested that the increase in laminarity from sub-adult to adult may be caused by a change in loading history from predominantly bending in the sub-adults to predominantly torsion in the adults or by ontogenetic changes in growth rate. They believed that the changes in growth rate may be the stronger factor, with lower growth rates in the adult bones linked to the higher laminar index.

The orientation of cortical canals has traditionally been measured using ground section histology but we here employ a more advanced method using micro computed tomography (micro-CT). Micro-CT is ideal for measuring canal orientation as it can visualize and measure the full 3D orientation of each canal in a bone's vascular network (Pratt & Cooper, 2017) and measures bone and canal morphology in three dimensions (Cooper et al., 2003). Compared to histology, micro-CT is also less destructive to the sample and enables analysis of a much larger number of canals.

In order to help shed more light on the relationship between growth rate and cortical canal orientation, we ran a controlled growth experiment using broiler chickens. Modern broiler chickens, including the strain used here, have undergone long-term selective breeding programs for faster growth and feed efficiency (Rawlinson et al., 2009) with modern broiler chicken growth rates 300% higher than ancestral birds (Knowles et al., 2008). These programs have been very successful resulting in animals with very high growth rates which can be easily controlled through their diet (Williams et al., 2004) by using feed restriction techniques. Broiler chickens are used extensively as meat poultry and their rapid growth rate results in skeletal issues including frequent bone defects and leg fractures (Knowles et al., 2008; Pines & Reshef, 2014). Extremely fast growth in these animals may lead to bones that are weaker with lower stiffness, resistance to fracture, and bones that may have lower ability to respond to mechanical loading (Rawlinson et al., 2009; Shim et al., 2012).

This study used two groups of broiler chickens: a control group fed ad libitum, and a feed restricted group. Following Williams et al. (2004) we predicted that the control group would have a significantly higher growth rate than the restricted group. We used micro-CT to scan a mid-diaphyseal portion of the right femur and humerus from each individual and measured the full 3D cortical canal orientation in each bone. We then calculated a laminar, radial, and longitudinal index for each bone. Based on the previous evidence suggesting a link between faster growth and radial canal orientation, we predicted that the restricted group would contain a lower radial index than the control group, and a higher laminar index. We also hypothesized that the humerus would have a higher laminar index than the femur. This would support the idea that bones involved in flight exhibit laminar bone as an adaptation to torsional loading.

4.2. Materials

We used 31 Ross 308 broiler chickens (Prairie Pride Natural Foods Ltd, Saskatoon, Canada) separated into two groups, an experimental group and a control group. The experimental group had a final N of 16 and the control group had a final N of 15. This is a commercial strain of chickens that has been bred extensively for fast growth. We used male chickens because they have a higher natural growth rate than females. The chicks were treated with Vaxxitek (Merial Canada). We started with day old chicks, which ensured control over the diet of the animals across their entire lifespan. We chose an endpoint of 42 days, a common end time point used in broiler chicken bone growth studies (Williams et al., 2000; 2004). By 37 days, areas of laminar bone have been observed in the tibiotarsus of broiler chickens (Leterrier & Nys, 1992), indicating that this time length is sufficient for laminar bone to develop. Micro-CT scans were taken of the mid humerus and femur of each individual. Animal ethics approval was granted by the University of Saskatchewan Animal Research Ethics Board of the University Committee on Animal Care and Supply (protocol 2015-0080) and by the Canadian Light Source.

4.3. Methods

4.3.1. Housing, Lighting

The two groups were placed in separate pens in a basic open floor chicken pen with Aspen shaving bedding. We used trough style feeders so that there was sufficient feeder space to ensure uniform access to the feed for each animal. During the first two days the pen had 24 hours of constant light. We followed a standard lighting schedule modified from (Schwean-Lardner, Fancher & Classen, 2012) with constant lighting until day 3 when the lighting was reduced to 23 hours of light and 1 hour dark, with the amount of light decreasing each day until day 8 when the pen had 18 hours of light and 6 hours of dark. This level of lighting was maintained until the end of the study.

4.3.2. Feed restriction

We used a feed restriction experimental design based on Williams et al. (2004) with a control group and a restricted group. The control group was fed ad libidum, using a commercial chicken feed. The experimental group had their feed restricted to 50% of that consumed by the control group. The restricted diet was based on the previous day's ad lib consumption, obtained by weighing the feed every morning. Following Williams et al. (2004), the restricted group was fed a custom feed with double the calcium and phosphorus content of the ad lib feed, to maintain similar calcium and phosphorus intake at the 50% feed level. Our feed was obtained from the Canadian Feed Research Centre in North Battleford, Canada. This degree of restriction has been shown to permit normal growth and health in the animals, while producing a noticeable effect on gross bone morphology (Williams et al., 2004). For the first four days, both groups were fed ad lib using a standard broiler starter feed. This ensured that feed restriction only occurred after the chicks were growing and developing normally

4.3.3. Growth measurement

Each animal was wing-banded on day 1 and individually weighed daily to establish growth rates for both the control and restricted feed groups. Final total weight was also measured for each bird. We used weight to measure growth because it correlates strongly with major physiological traits (Blueweiss et al., 1978) and is easy to measure consistently across the short lifespan of the animals (Lee et al., 2013).

4.3.4. Sample preparation

The animals were euthanized after 42 days using a T-61 euthanasia solution injected into the brachial (wing) vein. The humeri and femora were dissected out from each bird and macerated to clean the bones to create better quality micro-CT images. We used warm water enzyme maceration as it has been shown to be efficient while working on a short time scale while retaining good preservation. We used bromelain as our enzyme and Palmolive dish detergent as the active degreaser in an 80°C water bath (Steadman et al., 2006; Lee et al., 2010). Before maceration we removed as much soft tissue from the bones as possible. We also used a magnetic stirrer to help loosen the remaining soft tissue from the bone during maceration.

4.3.5. Micro-CT

We used in-line phase contrast synchrotron micro-CT (Tafforeau et al., 2006; Betz et al., 2007; Arhatari et al., 2011; Cooper et al., 2011) to image the right humerus and femur from each individual animal at midshaft. We defined midshaft as 50% of the bone's maximum length. Micro-CT imaging was performed at the BioMedical Imaging and Therapy (BMIT) insertion device beamline (Wysokinski et al., 2015), part of the Canadian Light Source (CLS) synchrotron facility. We used a Hamamatsu C9300-124 optical camera

paired with a Hamamatsu A40 x-ray converter to for an effective pixel size of 4.3 μm at 32 keV. Each bone was scanned with exposure times between 0.7–1 s per projection, with 1500 projections for each scan for a total individual scan time of 20-30 minutes. The exact exposure time was chosen based on the synchrotron beam ring current, which decays from a peak of 250 mA over time. Flat and dark images were collected before each scan to correct for noise in the x-ray beam and the detector. An Aluminum filter with an effective thickness of 1.1 mm was used to eliminate stray low energy harmonics in the x-ray beam. We used a propagation distance of 50 cm to optimize the phase in the scans (Pratt et al., 2015). Micro-CT at this resolution is able to distinguish canal microstructure (Cooper et al., 2007; Palacio-Mancheno et al., 2013), and phase contrast helps visualize microstructures and has a resolution enhancing effect (Pratt et al., 2015).

4.3.6. Image processing

We measured the orientation of the cortical network independently for each animal's humerus and femur scan following Pratt & Cooper (2017) and Pratt el al (2018). We used a custom image processing software package developed using the ImageJ (ImageJ, NIH) scripting platform to perform most of the data processing. The script suite is available at https://github.com/isaacpratt/canal-orientation. We did our correction for detector and beam noise using flat and dark projections, and reconstructed the micro-CT projections using NRecon (Bruker SkyScan, Kontich BE), a commercial software package. We used Amira (FEI Company, USA) to extract and skeletonize the canal network from the micro-CT bone scans into a lineset format. The produced lineset file contains a series of points representing the central axis of each canal. From this we simplified the series of points into a set of line segments which we can measure the orientation of and which preserve the variability of orientation in the network. This lineset is then simplified into a series of line segments with a branch length set by the macro. We measured two angles for each line segment: theta and phi. Phi is the angle between a canal segment and the long axis of the bone, and determines how longitudinal a canal is. Theta is the angle between a canal and a line from the bone centroid to the midpoint of that canal. The theta angle differentiates radial and circumferential canals. Using these two angles we can classify each line segment as longitudinal, radial, circumferential, or oblique. We classified canal segments following (de Margerie, 2002; Pratt & Cooper, 2017). We then calculate three indices, a laminar index, a longitudinal index, and a radial index, as the ratio of the sum of the length of all the circumferential, longitudinal, or radial canal segments over the total length of all canal segments.

4.3.7. Statistical Analysis

Statistical analysis was performed with SPSS version 24 (IBM, USA) using repeated measures two way ANOVAs to simultaneously compare the three orientation indices between the two groups (between-subjects factor) and the two bones (within-subjects factor). We used pairwise comparisons to obtain the mean differences of the indices between the two groups and the two bones. Body weight and growth rate were compared

using a repeated measures ANOVA. Sphericity was not rejected for our data. Shapiro wilks test was run on all variables and all were found to be normally distributed, and Levene's test was run for all variables and homogeneity was not rejected. We set our alpha level at $p = 0.05$.

4.4. Results

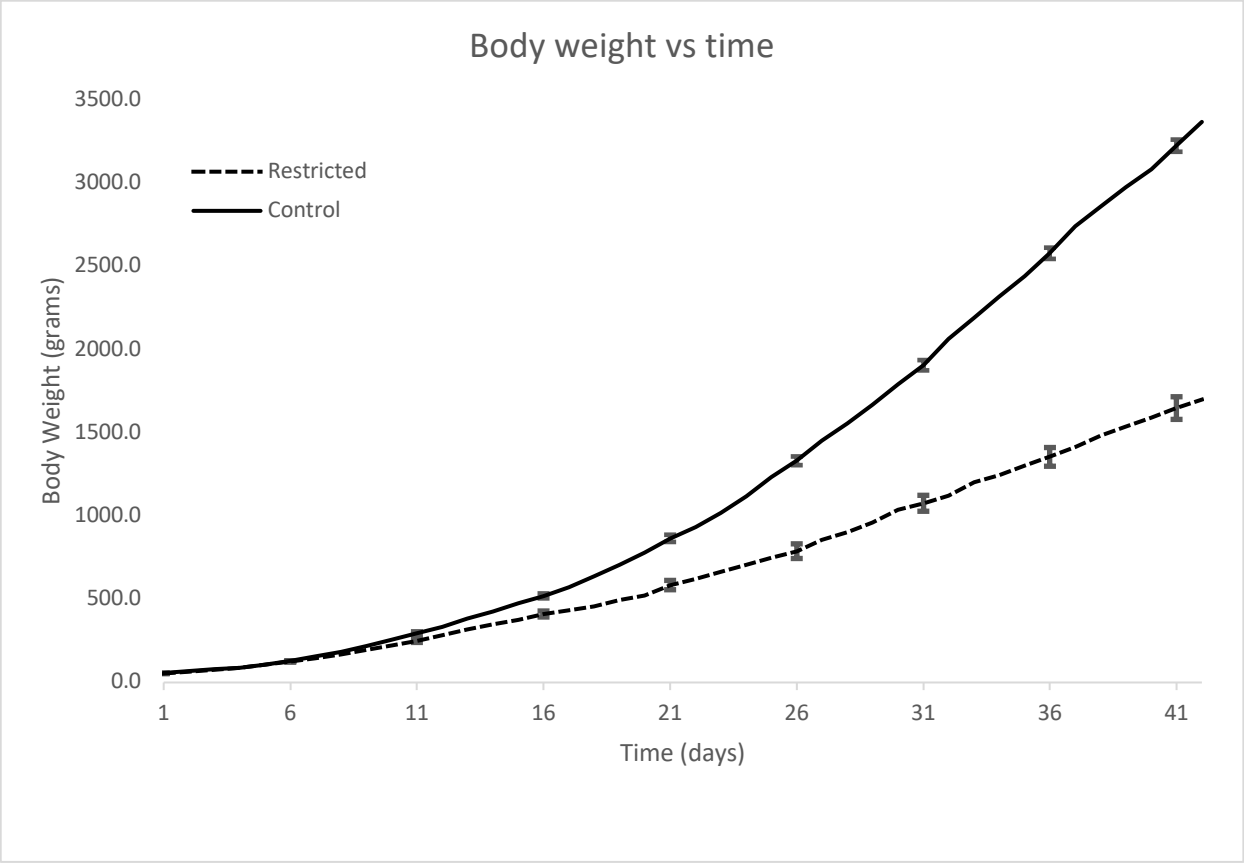

Figure 4.1: Mean body weight over time. The restricted group is shown with a dashed line and the control group is shown with a solid line. Error bars show the standard error every five data points.

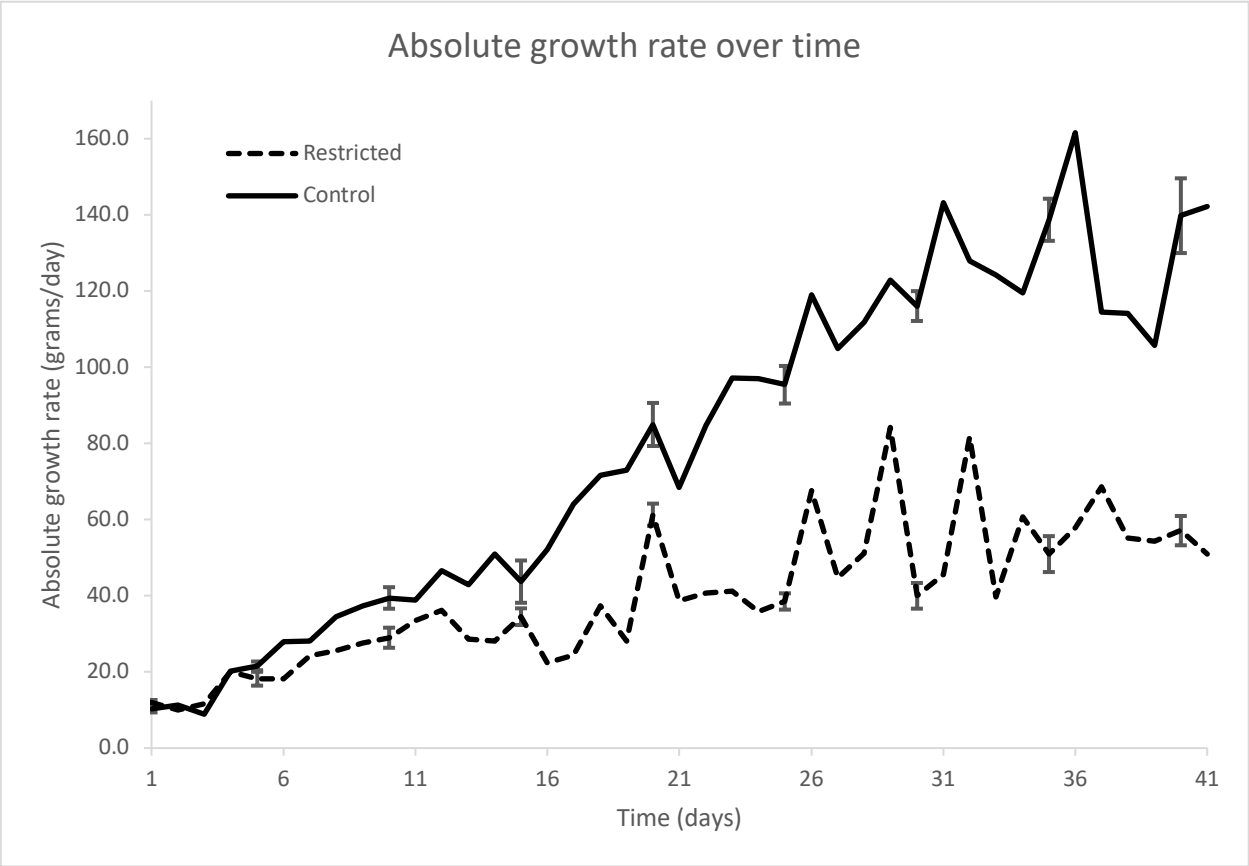

Figure 4.2: Mean growth rate over time. The restricted group is shown with a dashed line and the control group is shown with a solid line. Error bars show the standard error every five data points.

At the end of the study (42 days) the mean weight of the control group at 3366g was almost twice the mean weight of the restricted group at 1698g. The two groups started to diverge in weight at day 8 (restricted = 168.3g; control = 185.3g; p = 0.049) and the weight difference accelerated from there (see figure 4.1). Our broilers achieved higher final weights than those in (Williams et al., 2004), with their 'commercial' strain (equivalent to our control group) achieving a weight of 2556g and their restricted group achieving a weight of 1226g. The final absolute growth rate of the control group at 42 days was 142.9 g/day, almost three times that of the restricted group, at 47.9 g/day. The two groups started to differ in absolute growth rate at day 6 (restricted = 18.2 g/day, control = 21.6 g/day, p = 0.001), and continued to diverge from there (see figure 4.2) although there were still some days after that where the difference in absolute growth rate was not significant (7, 11, 15).

Table 4.1: Descriptive statistics for the cortical orientation indices.

Variable	*Study group*	*Bone*	*Mean (%)*	*Std. D. (%)*
Laminar Index	Control	Humerus	15.64	2.98
		Femur	10.02	2.56
	Restricted	Humerus	21.60	3.95
		Femur	14.54	2.92
Radial Index	Control	Humerus	38.71	5.46
		Femur	55.64	5.37
	Restricted	Humerus	28.75	3.81
		Femur	44.44	4.37
Longitudinal Index	Control	Humerus	33.46	3.46
		Femur	21.17	3.12
	Restricted	Humerus	36.21	2.98
		Femur	26.52	3.95

Table 4.2: Comparison between control and restricted chicken groups. A positive mean difference means the control group has a higher value than the restricted group. All variables were found to be statistically significant.

Variable	*Bone*	*Mean difference (%)*	*Std. error*	*Sig.*
Laminar Index	Humerus	-5.96	1.21	<0.001
	Femur	-4.51	0.95	<0.001
Radial Index	Humerus	9.96	1.65	<0.001
	Femur	11.21	1.71	<0.001
Longitudinal Index	Humerus	-2.75	1.13	0.021
	Femur	-5.35	1.23	<0.001

Table 4.3: Comparison between humerus and femur in the control and restricted chicken groups. A positive mean difference means the humerus has a higher average value than the femur. All variables were found to be statistically significant.

Variable	*Group*	*Mean difference (%)*	*Std. error*	*Sig.*
Laminar Index	Control	5.62	1.02	<0.001
	Restricted	7.06	1.05	<0.001
Radial Index	Control	-16.94	1.51	<0.001
	Restricted	-15.69	1.56	<0.001
Longitudinal Index	Control	12.29	1.07	<0.001
	Restricted	9.69	1.10	<0.001

Descriptive statistics for the laminar, radial, and longitudinal indices are shown in table 4.1. Comparisons between groups and bones are shown in tables 4.2 and 4.3, and P-values for all comparisons are shown in the tables. Statistics for the comparison between the restricted and control groups are shown in table 4.2, and for the comparison between the humerus and femur are shown in table 4.3. The comparisons are illustrated in figure 4.3. Micro-CT slices are shown in figure 4.4 to show the microstructure and 3D renders of canal segments are shown in figure 4.5 to illustrate the orientations discussed in the text.

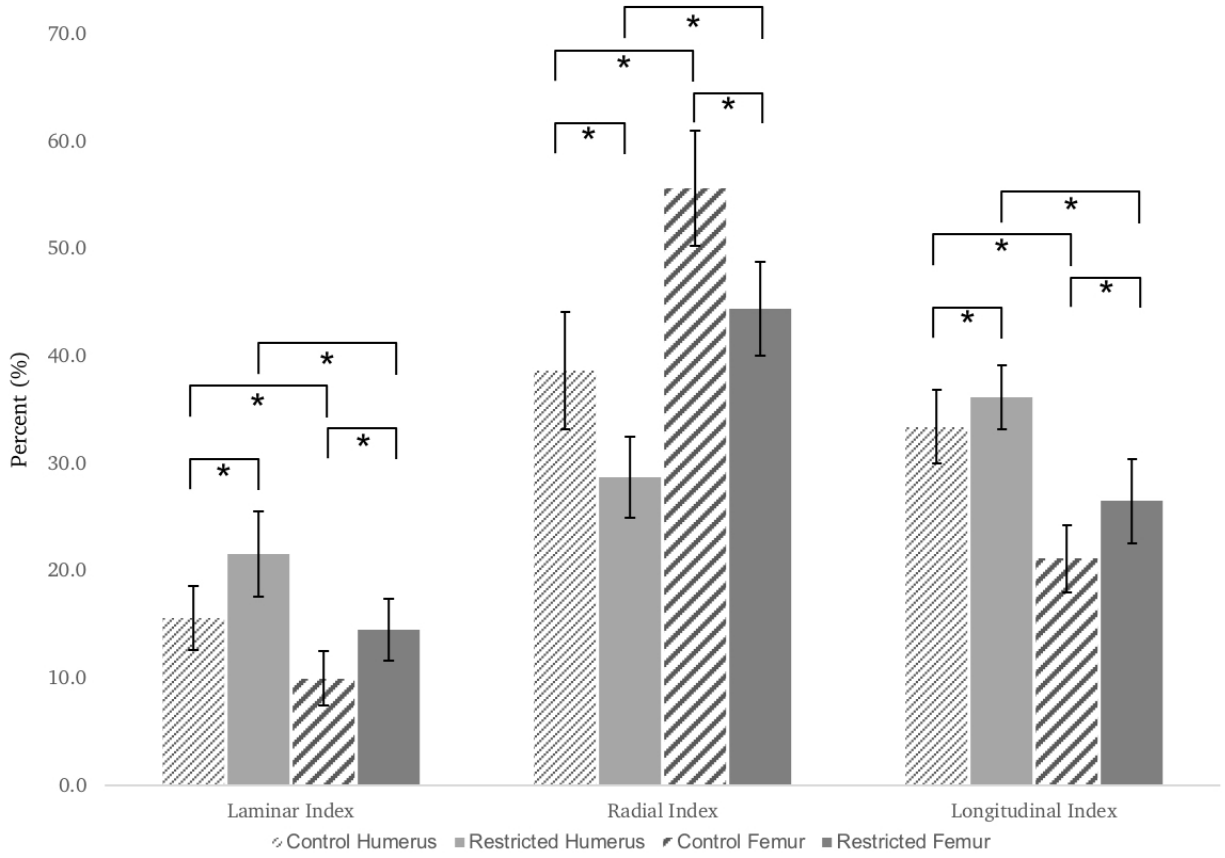

Figure 4.3: Graph showing the comparison of the laminar, radial, and longitudinal indices between the humerus and femur in the control and restricted groups. Error bars show the standard error and significant differences are marked with an asterisk.

Both groups had very highly vascularized bones (see figure 4.4) with sections of new bone growth at the periosteum and endosteum. Larger vascular spaces were often seen close to the endosteal border of the bones, and long radial canals were often seen reaching from far into the cortex from both the periosteal and endosteal borders. Typically the birds had larger femora than humeri. The most common canal type in the bones was radial for both groups' femora and the control humeri or longitudinal for the restricted humeri. Several bones had areas, especially close to the periosteum, with locally higher numbers of circumferential canals near the periosteum but overall circumferential was the least common canal type for both bones in both groups.

We found that the laminar index was higher in the restricted group than in the control group for both bones, and higher in the humerus than the femur for both groups. The radial index was lower in the restricted group than in the control group for both bones, and lower in the humerus than in the femur for both groups. The longitudinal index was higher in the restricted group than in the control group for both bones, and higher in the humerus than the femur for both groups. No interaction effect was found between bone and group.

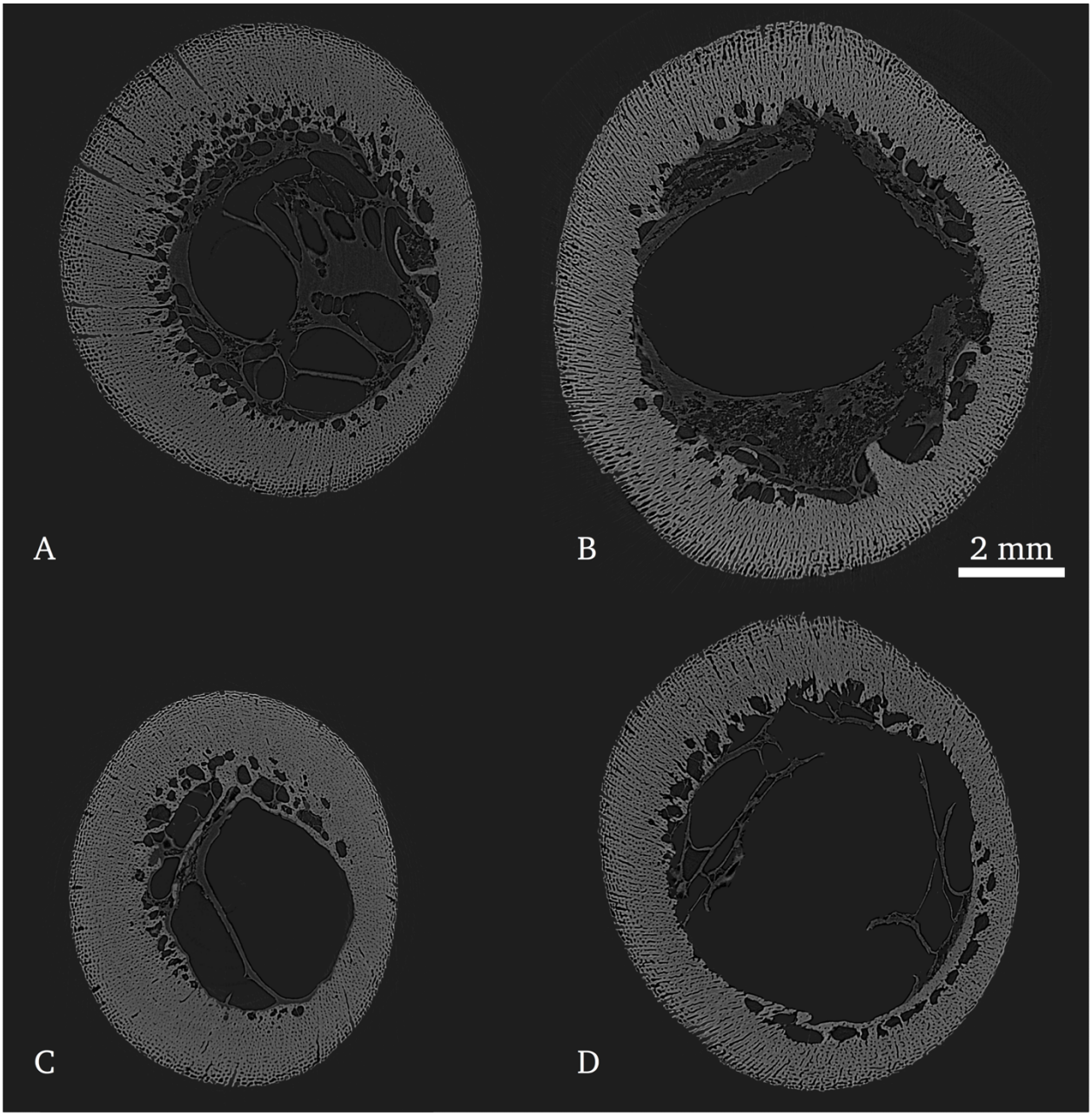

Figure 4.4: Micro-CT slices. Each image is created by averaging 5 consecutive micro-CT slices. **A** shows a control humerus, **B** shows a control femur, **C** shows a restricted humerus, and **D** shows a restricted femur. All the images are of mid-humerus 42 day old chickens post euthanization. Several radial canals are noticeable in the top left of **A**.

4.5. Discussion

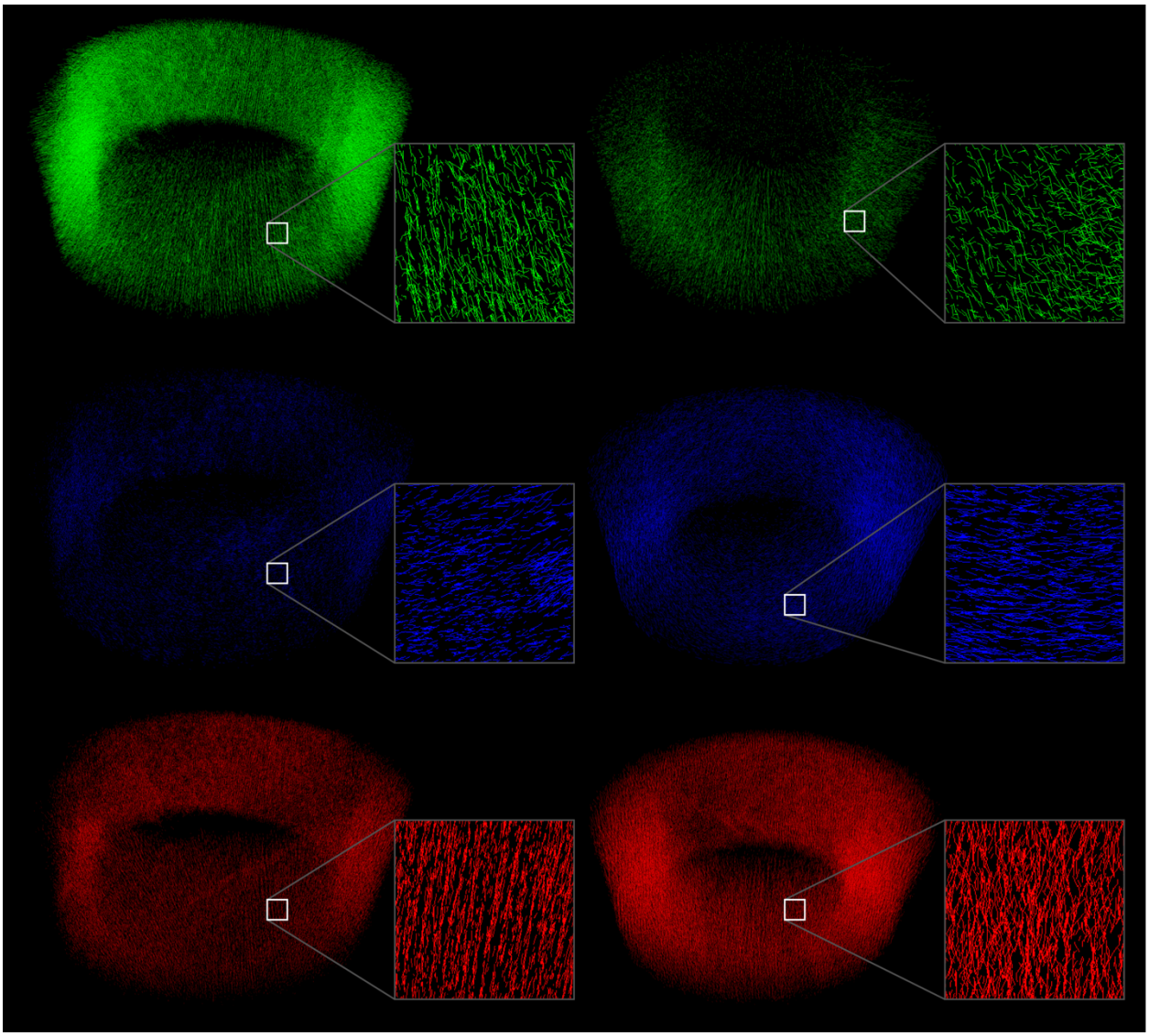

Figure 4.5: 3D renders of canal segments with circumferential shown in blue, longitudinal in red, and radial in green. The left side shows a control femur with a high radial index and a low laminar index, and the right side shows a restricted humerus with a low radial index and a high laminar index. Inset panes show close ups of the canals to better show the orientation. All the images are of 42 day old animals post euthanization.

Both the humerus and the femur in our study had areas of cortex with noticeably radial canals in both groups, although this was more evident in the femur and the control group. This was confirmed by the orientation index analysis, where the control group had a significantly higher radial index than the restricted group, and the femur had a significantly higher radial index than the humerus. This aligns with previous research indicating that bone with radial canals has a higher growth rate than bone with other canal

types (de Margerie et al., 2004). de Margerie et al. (2004) used fluorescent labeling in king penguin chicks and showed that bone with mainly radial vascularization had the fastest growth rate, followed by longitudinal and reticular (oblique) bone, then laminar bone with the slowest growth rate. Our results agree with this, our faster growing control group had a lower laminar index than the slower growing restricted group. Our results support the hypothesis that growth rate is linked with canal orientation, and specifically that there is a connection between radial canals and faster growing bone. While the restricted group had a higher longitudinal index, the mean difference between the groups was slight, only 2.75/5.35% in the humerus and femur respectively. The mean difference between the bones was much greater at 9.69/12.29% in the control and restricted groups respectively, with the longitudinal index significantly higher in the humerus than the femur. de Margerie et al. (2002) set 50% as the value of the laminar index required for calling a bone 'laminar' and none of our bones met that value, although that value was for measurements from traditional histological sections, an approach which tends to overestimate the laminar index (Pratt et al., 2018). We found a significantly higher laminar index in the humerus than in the femur for our groups, supporting the functional loading hypothesis. These results conflict with the results found in our previous study (Pratt et al., 2018), where we found that the femur had a higher laminar index than the humerus. In that study we measured orientation indices in a broad "comparative" sample of medium-large sized wild birds using the same method employed here.

A closer look at the data shows that the laminar index for the broiler groups' humeri here (15.64±2.98% control & 21.60±3.95% restricted) are in the same range as the laminar indices reported for the comparative bird group (18.3±5.3%) presented in (Pratt et al., 2018), while the laminar index for the broiler femora reported here (10.02±2.56% control & 14.54±2.92% restricted) are lower than the comparative birds' femora (23.2±7.5%). As a result, the reason for the difference between the results presented here and our previous study is likely to lie in biomechanical differences in the femur between broiler chickens and other bird species. Carrano (1998) measured a number of biomechanical properties in hindlimbs of birds including femur angle relative to the horizontal. They found that chickens had the most vertical orientation of all the extant birds they sampled. In a later study involving experimental alteration of limb posture, Carrano & Biewener (1999) found that chickens with more horizontal femur angles experienced less torsional force than chickens with more vertical femur angles. This suggests that the femora in our chickens likely experience lower torsional force than the femora of the comparative bird sample from (Pratt et al., 2018), explaining why we find different patterns in the laminar index in this study. Broiler chickens can fly only limited distances in short bursts and the restricted group exhibited more flying behaviour in the open pen than the control group, likely as a consequence of the control group's higher weight. The limited use of their wings means they are likely to experience less torsional stress on the bones than the more intensely flying birds in the (Pratt et al., 2018) study. Based on this, the higher laminar index we found in the restricted group than the control group may support the functional loading hypothesis. It could also be that the higher laminar index in the humerus than the femur is due to a lower growth rate in the humerus. Overall our results support

interpreting the orientation of vascular canals as responding to both growth rate and functional loading.

We used body weight as a proxy for bone growth as measuring bone growth directly is complex. Jepsen & Andawaris-Puri (2012) built a model of human bone apposition during aging and found that differences in cortical thickness and diameter affected the apposition rate of bone. In particular, through their simulation they found that slender bones needed to have a higher periosteal apposition rate than more robust bones to maintain stiffness during aging. This paper points out that bone growth and bone modeling are not constant or necessarily consistent. The result is that bone growth may not be linear and/or equivalent within each of our animal groups or bones. While this proxy is sufficient for our analysis, further studies could add new information by measuring bone growth directly. Potential methods to measure bone formation rate include flurochrome labeling, although it is invasive and not always reliable (de Margerie et al., 2004); using cross-sectional bone geometry data to produce general bone growth curves, which requires more animals; or using longitudinal *in vivo* micro-CT which can measure changes in cortical diameter.

Birds go through remodeling during life, so if the orientation of secondary canals produced after flight behaviour manifests differs from the orientation of the primary canals, that change could be shown using a longitudinal study and might reflect changes in locomotor behaviour or changes in growth rate in mature bone tissue. Along those lines Skedros & Hunt (2004) measured the laminar index in turkey ulnae and found that adults had a significantly higher laminar index than subadults. They proposed two possible interpretations: either a link to a mechanical/functional loading change in adulthood or a change in growth rate. Their mechanical hypothesis was based on either the primary vascular network being linked to a prevalent strain direction and primary bone laid down around it or the collagen fiber orientation being linked to the strain direction directly and mediating the orientation of the vascular canal network. Their second hypothesis is based on ontogenic changes in growth rate, following Lee et al. (2004) and Petrytyl et al. (1996) who propose that a greater longitudinal orientation of canals in primary bone aligns with a greater bone growth direction in that direction. They suggest that a prevalence of longitudinal canals is a consequence of longitudinal shifting of the periosteum against the bone surface.

Measuring laminar and other indices using histology underestimates the amount of longitudinal canals present in a bone section. The method popularized by de Margerie et al. (2002) uses the area of the canals to calculate the laminar index, and because most of the area of longitudinal canals is perpendicular to the cross-section, it is consistently underestimated. Our previous work (Pratt et al., 2018) using the same technique has shown that using an area-based index measurement underestimated the area of longitudinal canals by 20% and consequentially overestimate the laminar index by 7.7% in a comparative sample of birds and bats. The conventional criteria for assigning a canal as longitudinal is based on a measurement of how circular the cross section of the canal is in the plane of sectioning, which relies on the assumption that canals are circular (de

Margerie, 2002; de Boef & Larsson, 2007a). Our experience along with evidence from micro-CT suggests that this assumption is not consistently well supported (Hennig et al., 2015), and that osteons and canals are not always circular in cross section but are often oval in shape.

We believe that micro-CT is the ideal method for measuring canal orientation as it measures the complete cortical network in 3D, easily capturing data for a large proportion of a long bone's shaft. It does, however, have a lower resolution than histology and lab based micro-CT systems are typically unable to visualize some histological features of interest including canaliculi, lines of arrested growth (LAGs), and osteonal boundaries (Cooper et al., 2011). These resolution deficiencies can be remedied with advanced nano-CT (Peyrin et al., 2014) or phase contrast enhanced micro-CT systems (Arhatari et al., 2011; Cooper et al., 2011; Sanchez et al., 2012; Carter et al., 2013; Andronowski, Pratt & Cooper, 2017) that have higher resolutions better than 1-2 μm but these systems are rare and expensive.

Based on the quality of the micro-CT scans in this study we were unable to differentiate primary canals and secondary canals. For our animals because of their short lifespan we can assume that all the canals are from their current growth period/functional loading regime and will be predominantly primary, but distinguishing primary from secondary canals can be very important in longitudinal studies or studies of animals later in life. Using higher resolution phase contrast micro-CT with resolution around or better than 1-2 μm is able to visualize osteon boundaries and distinguish these canal types (Arhatari et al., 2011; Maggiano et al., 2016) and this level of resolution could add new information if used in future studies. Previous research has shown that *in vivo* micro-CT can be used to image cortical canals in live rats (Harrison & Cooper, 2015; Pratt et al., 2015), using phase contrast to overcome the necessity of low dose. This technique could be used for longitudinal experimental studies modifying the behaviour or growth rate of an animal.

4.6. Conclusion

We found a higher growth rate, a higher radial index, and a lower laminar index in the control group than in the restricted group. These results support the hypothesis that vascular canal orientation is connected to growth rate, with radial canals linked to faster growth, and circumferential canals (and laminar index) linked to slower growth. We also found a higher laminar index in the humerus than in the femur, supporting the hypothesis that canal orientation is linked to functional loading – specifically that a high laminar index is linked to torsional loading. Overall our results indicate a complex interplay of growth rate and functional loading determines the predominant orientation of the cortical canal network. Experimental studies on animal models are a useful tool for investigating cortical bone microstructure. Further experiments should look to do longitudinal studies using *in vivo* scanning to investigate the time period around the transition to adulthood. This period often includes changes to locomotor behaviour such as the acquisition of flight in birds or changes in growth rate due to the acquisition of adult body weight. Mechanical testing of

specific bone sections with different canal types could also add information about potential differences in directional bone strength.

Chapter 5. Conclusions

5.1. Overview

Chapter 1 started the thesis with an introduction to bone and cortical microstructure, and followed with background material on bone imaging methods including histology and micro-CT. This chapter established the rationale for and specific goals of the thesis, and established that micro-CT is the best method to use for imaging bone microstructure because of the 3D nature of canal orientation.

Chapter 2 demonstrated a new method for measuring the orientation of vascular canals. This method starts by imaging cortical bone porosity in 3D using micro-CT. It described a series of custom written scripts used to convert the canal network morphology into a series of line segments while preserving the shape, orientation, and length of the canal network. Laminar, radial, and longitudinal orientation indices based on previous histological methods are introduced and adapted for the 3D measurements. This chapter formulated the equations for the orientation measurement script, and illustrated the use of the technique with examples of a rat tibia and a red tailed hawk humerus. Chapter 2 was published in *Micron* in 2017 (Pratt & Cooper, 2017).

Chapter 3 presented a comparative study between a diverse set of large birds and bats. This chapter described how we used micro-CT to scan the humerus and femur of each individual, and used the method from Chapter 2 to measure the orientation of the canal network in the scanned bones. Compared to Chapter 1, Chapter 2 developed the measurement method further to weight the orientation indices by the length of the line segments. It also added a pseudo-2D orientation index measurement system we used to compare our 3D orientation measurements with previously reported 2D histology-based orientation measurements. In it we compared the orientation of canals between the humerus and the femur in each group, and between the bird and bat groups in the humerus and the femur. It found highly vascularized cortices in the birds and poorly vascularized cortices in the bats. The results showed that birds have a significantly higher laminarity index than bats, and counter to expectation, the birds had a significantly higher laminarity index in the femur than in the humerus. The psueudo-2D method significantly underestimated the longitudinal index by an average of 20% and significantly overestimated the laminarity index by an average of 7.7%, which indicated that histology methods are not reliable indicators of canal orientation. Overall, the results in this study did not support the hypothesis that the bones of flight are more laminar. This study was the first cross-sectional study to evaluate the full 3D orientation of vascular canals, and was published in the *Journal of Anatomy* in 2018 (Pratt et al., 2018).

After finding no relationship between laminar index and functional loading in the different bones of Chapter 3, Chapter 4 described our next study, where we aimed to examine the effect of growth rate on canal orientation. In this chapter we used feed restriction to

control the growth rate of broiler chickens separated into two groups, one with high growth rate and one with low growth rate. Our results showed that feed restriction was effective at controlling the growth rate, producing a fast growth group that ended up twice the size of the slow growing group. This chapter again used micro-CT to image the humerus and femur of each individual in each group, and used the script suite from Chapter 3 to measure the orientation indices in each scanned bone. It found that the humerus had higher laminar and longitudinal indices and a lower radial index than the femur, and the fast growth group had higher radial index and lower laminar and longitudinal indices than the slow growth group. The higher radial indices in our fast growth group pointed to a link between radial canals and faster growth, and laminar canals and slower growth, while the higher laminar indices in the humerus pointed to a link between circumferential canals and torsional loading. Overall the results in this chapter indicated that the orientation of the cortical canal network in a bone is the consequence of a complex interaction between that bone's growth rate and functional loading environment.

5.2. Future Directions

Our method using micro-CT to capture 3D vascular canal orientation in cortical bone opens up new opportunities for studies of canal orientation as a cortical bone parameter. Micro-CT has several key advantages over histology for experimental and cross sectional studies. It is less destructive than histology and can in some cases be completely non-destructive, depending on the size of the bone and the type and resolution of the micro-CT system used. A combination study of micro-CT and histology could be used to differentiate between primary and secondary canals and compare the orientation between them. Cortical bone scans can be performed on animal limbs that have not been processed at all, although x-ray contrast is better in defleshed bone scans. In small animals like rats, mice, and rabbits, micro-CT can image the cortical porosity *in-vivo* (Pratt et al., 2015). Scanning *in vivo* opens up the possibility of longitudinal studies which can directly detect changes in canal orientation in the same bone over time. Statistical power is inherently greater in longitudinal studies than cross-sectional studies which means fewer animals are required and the data produced is higher quality.

In order to further elucidate the relationships between orientation and functional loading, and between orientation and growth rate, more studies need to be done. While some studies have measured strains on live birds (Biewener, SWARTZ & Bertram, 1986; Biewener & Dial, 1995; Judex, Gross & Zernicke, 1997; Main & Biewener, 2007), no studies to date have correlated canal orientation with real strain measurements. There are several interesting possibilities for cross-sectional or longitudinal studies on canal orientation. Research at specific time points offers the ability to compare orientation between different conditions. Some key time points in the life of an animal where we would predict orientation to change are the time around acquisition of adult locomotor behaviour and time points surrounding changes in growth rate such as growth spurts and the time surrounding sexual maturation/puberty. In birds, the adult locomotion style is

flight while the juveniles are terrestrial and not very active. This presents a drastic shift in functional loading that the bones experience. If functional loading impacts the orientation of vascular canals, we would expect canals formed after flight is achieved would have different orientations to those formed before flying behaviour begins.

Our comparative study of birds and bats, presented in Chapter 3, followed the example of many studies in the literature by examining flying vertebrates (Skedros & Hunt, 2004; de Margerie et al., 2005). There are several straightforward potential avenues to expand this research going forward.

The first is to expand the sample size to include more species and more individuals and more bones from each examined species. Many of the species we looked at are represented by only a single individual. This limitation was the result of the difficulty of getting access to large collections with specimens. We attempted to overcome this limitation with multiple species that are closely related and use similar locomotor behaviours. For example, our sample of birds contained red-tailed hawks (*Buteo jamaicensis*), Rough-legged hawk (*Buteo lagopus*), and Swainson's hawk (*Buteo swainsoni*), which are all closely related species from the same genus. We looked at only the humerus and femur for each individual, which are the main and largest bones of the forelimb and hindlimb. This is important in small animals that may be inconsistently vascularized. In general in small animals (around and under the size of a rat) the larger bones will typically have more canals, with smaller bones sometimes being completely avascular(de Buffrénil, Houssaye & Böhme, 2008; Lee & Simons, 2015). Expanding the choice of bones scanned could help strengthen the comparison between the forelimb and hindlimb. In the forelimb, the ulna is another bone that is important in flight. In birds, the ulna is an attachment site for secondary flight feathers and has been used in several studies which have looked at canal orientation and generally been found to have a high laminar index (de Margerie, 2002; Skedros & Hunt, 2004). In the hindlimb, the tibia is the next largest bone. In the hindlimb of birds, the tibia is believed to experience mainly bending forces, and in previous histological studies has been found to have a low laminar index (de Margerie et al., 2005). These two bones would be the next logical targets to add for increasing the sample.

The second path to expand the research is to add more taxonomic groups. Birds and bats are the only two extant groups of flying vertebrates, but there are extinct groups of vertebrates that flew including most notably pterosaurs and the many extinct transitional groups between dinosaurs and modern birds. Micro-CT is an excellent technique for studying fossil remains as it is non-destructive, a real advantage when using fossil remains which are rare and access to specimens is limited. In addition to adding more groups of flying vertebrates, terrestrial and aquatic species remain unexplored. Very little is known about the orientation of vascular canals in mammals, fish, and reptiles, with only a few papers focused on reptiles (Lee, 2004; de Buffrénil, Houssaye & Böhme, 2008). In humans very little research has been done since the studies by Hert (1994) and Petrtyl (1996) and these studies were not able to fully quantify the orientation of canals. Similarly, the older classic studies in comparative histology (Enlow & Brown, 1958; de Ricqlès, 1968; 1969;

1972,a,b; 1975; 1981) provide a lot of information on canals in a broad range of species but rely on qualitative assessments of the orientation patterns from histology slices which can be unreliable. Quantifying the orientation of vascular canals in 3D in these underexplored groups, each with their own unique growth patterns and functional loading regimes, would add valuable information to the literature.

Chapter 4 presented an experimental study in broiler chickens, using a dietary restriction to attempt to experimentally modify the orientation of vascular canals from their naturally occurring state. Experimental studies that modify a characteristic of an animal have great potential to help determine how the orientation of the vascular canal network develops and changes over time. Studies modifying behaviour, growth rate, or diet can all have an impact on vascular canal orientation. Britz (2012) looked at the orientation of canals in rats that had been immobilized through sciatic neurectomy and found that the intervention had a significant effect on canal orientation. Modifications to locomotor behaviour will likely be very effective in producing differences in canal orientation.

5.3. Conclusions

This thesis was the first to demonstrate differences in vascular canal orientation in 3D. It showed a new method for measuring canal orientation in 3D using micro-CT and emphasized the importance of measuring orientation in 3D to avoid unreliable assumptions about canal geometry. It found conflicting results about a link between functional loading and canal orientation, with no correlation in the comparative sample and a strong correlation in the broiler chicken sample. It found a strong link between growth rate and functional loading in the broiler chicken sample, and supported a link between fast growth and radial index, and slow growth and laminar index. Overall the results in this thesis demonstrate that vascular canal orientation is a parameter with links to both loading environment and growth rate.

References

Ammann, P. & Rizzoli, R. 2003. Bone strength and its determinants. *Osteoporosis International*. 14(Suppl 3):S13–18. DOI: 10.1007/s00198-002-1345-4.

Amos, W.B. & White, J.G. 2003. How the confocal laser scanning microscope entered biological research. *Biology of the cell*. 95(6):335–342. DOI: 10.1016/S0248-4900(03)00078-9.

Andronowski, J.M., Pratt, I.V. & Cooper, D.M.L. 2017. Occurrence of osteon banding in adult human cortical bone. *Am J Phys Anthropol*. 28(3):211–642. DOI: 10.1002/ajpa.23297.

Arhatari, B.D., Cooper, D.M.L., Thomas, C.D.L., Clement, J.G. & Peele, A.G. 2011. Imaging the 3D structure of secondary osteons in human cortical bone using phase-retrieval tomography. *Phys Med Biol*. 56(16):5265–5274. DOI: 10.1088/0031-9155/56/16/012.

Ashique, A.M., Hart, L.S., Thomas, C.D.L., Clement, J.G., Pivonka, P., Carter, Y., Mousseau, D.D. & Cooper, D.M.L. 2017. Lacunar-canalicular network in femoral cortical bone is reduced in aged women and is predominantly due to a loss of canalicular porosity. *Bone reports*. 7:9–16. DOI: 10.1016/j.bonr.2017.06.002.

Augat, P. & Schorlemmer, S. 2006. The role of cortical bone and its microstructure in bone strength. *Age and ageing*. 35 Suppl 2(suppl_2):ii27–ii31. DOI: 10.1093/ageing/afl081.

Bennett, M. & Forwood, M. 2010. Histomorphometric changes in the wing bones of the fruit bat, Pteropus poliocephalus, (Megachiroptera: Pteropidae) in relation to increased bone strain and the failure of a good (?) hypothesis. *Australian Zoologist*. 35(2):341–348. DOI: 10.7882/AZ.2010.022.

Betz, O., Wegst, U., Weide, D., Heethoff, M., Helfen, L., Lee, W.K. & Cloetens, P. 2007. Imaging applications of synchrotron X-ray phase-contrast microtomography in biological morphology and biomaterials science. 1. General aspects of the technique and its advantages in the analysis of millimetre-sized arthropod structure. *J Microsc*. 227(1):51–71. DOI: 10.1111/J.1365-2818.2007.01785.X.

Biewener, A.A. & Dial, K.P. 1995. In vivo strain in the humerus of pigeons (Columba livia) during flight. *J Morphol*. 225(1):61–75. DOI: 10.1002/jmor.1052250106.

Biewener, A.A., SWARTZ, S.M. & Bertram, J.E. 1986. Bone modeling during growth: dynamic strain equilibrium in the chick tibiotarsus. *Calcif Tissue Int*. 39(6):390–395.

Blueweiss, L., Fox, H., Kudzma, V., Nakashima, D., Peters, R. & Sams, S. 1978. Relationships between body size and some life history parameters. *Oecologia*. 37(2):257–272. DOI: 10.1007/BF00344996.

Bouxsein, M.L., Boyd, S.K., Christiansen, B.A., Guldberg, R.E., Jepsen, K.J. & Müller, R. 2010. Guidelines for assessment of bone microstructure in rodents using micro-computed tomography. *Journal of bone and Mineral Research*. 25(7):1468–1486. DOI: 10.1002/jbmr.141.

Bravin, A., Coan, P. & Suortti, P. 2013. X-ray phase-contrast imaging: from pre-clinical applications towards clinics. *Phys Med Biol*. 58(1):R1–35. DOI: 10.1088/0031-9155/58/1/R1.

Britz, H.M., Jokihaara, J., Leppanen, O.V., Jarvinen, T. & Cooper, D.M.L. 2010. 3D visualization and quantification of rat cortical bone porosity using a desktop micro-CT system: a case study in the tibia. *J Microsc*. 240(1):32–37. DOI: 10.1111/j.1365-2818.2010.03381.x.

Britz, H.M., Carter, Y., Jokihaara, J., Leppänen, O.V., Järvinen, T.L.N., Belev, G. & Cooper, D.M.L. 2012. Prolonged unloading in growing rats reduces cortical osteocyte lacunar density and volume in the distal tibia. *Bone*. 51(5):913–919. DOI: 10.1016/j.bone.2012.08.112.

Britz, H.M., Jokihaara, J., Leppänen, O.V., Järvinen, T.L.N. & Cooper, D.M.L. 2012. The effects of immobilization on vascular canal orientation in rat cortical bone. *J Anat*. 220(1):67–76. DOI: 10.1111/j.1469-7580.2011.01450.x.

Buie, H.R., Campbell, G.M., Klinck, R.J., MacNeil, J.A. & Boyd, S.K. 2007. Automatic segmentation of cortical and trabecular compartments based on a dual threshold technique for in vivo micro-CT bone analysis. *Bone*. 41(4):505–515. DOI: 10.1016/j.bone.2007.07.007.

Burghardt, A.J., Buie, H.R., Laib, A., Majumdar, S. & Boyd, S.K. 2010. Reproducibility of direct quantitative measures of cortical bone microarchitecture of the distal radius and tibia by HR-pQCT. *Bone*. 47(3):519–528. DOI: 10.1016/j.bone.2010.05.034.

Burr, D.B., Martin, R.B., Schaffler, M.B. & Radin, E.L. 1985. Bone remodeling in response to in vivo fatigue microdamage. *J Biomech*. 18(3):189–200.

Carrano, M.T. 1998. Locomotion in non-avian dinosaurs: Integrating data from hindlimb kinematics, in vivo strains, and bone morphology. *Paleobiology*. 24(4):450–469. DOI: 10.1017/S0094837300020108.

Carrano, M.T. & Biewener, A.A. 1999. Experimental alteration of limb posture in the chicken (*Gallus gallus*) and its bearing on the use of birds as analogs for dinosaur locomotion. *J Morphol*. 240(3):237–249. DOI: 10.1002/(SICI)1097-4687(199906)240:3<237::AID-JMOR3>3.0.CO;2-N.

Carter, D.R. 1984. Mechanical loading histories and cortical bone remodeling. *Calcif Tissue Int*. 36(1):S19–S24. DOI: 10.1007/BF02406129.

Carter, Y., Thomas, C.D.L., Clement, J.G., Peele, A.G., Hannah, K. & Cooper, D.M.L. 2013. Variation in osteocyte lacunar morphology and density in the human femur--a synchrotron radiation micro-CT study. *Bone*. 52(1):126–132. DOI: 10.1016/j.bone.2012.09.010.

Castanet, J., Rogers, K.C., Cubo, J. & Boisard, J.J. 2000. Periosteal bone growth rates in extant ratites (ostriche and emu). Implications for assessing growth in dinosaurs. *Comptes rendus de l'Academie des sciences. Serie III, Sciences de la vie*. 323(6):543–550.

Chapman, D., Thomlinson, W., Johnston, R.E., Washburn, D., Pisano, E., Gmur, N., Zhong, Z., Menk, R., et al. 1997. Diffraction enhanced x-ray imaging. *Phys Med Biol*. 42(11):2015–2025.

Cho, H. 2012. The Histology Laboratory and Principles of Microscope Instrumentation. In *Bone Histology: An Anthropological Perspective*. CRC Press. 341–359. DOI: 10.1201/b11393-15.

Ciani, C., Doty, S.B. & Fritton, S.P. 2009. An effective histological staining process to visualize bone interstitial fluid space using confocal microscopy. *Bone*. 44(5):1015–1017. DOI: 10.1016/j.bone.2009.01.376.

Cohen, J. & Harris, W.H. 1958. The Three-Dimensional Anatomy of Haversian Systems. *Journal of Bone and Joint Surgery-American Volume*. 40(2):419.

Cooper, D., Turinsky, A., Sensen, C. & Hallgrímsson, B. 2007. Effect of voxel size on 3D micro-CT analysis of cortical bone porosity. *Calcif Tissue Int*. 80(3):211–219. DOI: 10.1007/s00223-005-0274-6.

Cooper, D.M.L., Erickson, B., Peele, A.G., Hannah, K., Thomas, C.D.L. & Clement, J.G. 2011. Visualization of 3D osteon morphology by synchrotron radiation micro-CT. *J Anat*. 219(4):481–489. DOI: 10.1111/j.1469-7580.2011.01398.x.

Cooper, D.M.L., Kawalilak, C.E., Harrison, K., Johnston, B.D. & Johnston, J.D. 2016. Cortical Bone Porosity: What Is It, Why Is It Important, and How Can We Detect It? *Curr Osteoporos Rep*. 14(5):187–198. DOI: 10.1007/s11914-016-0319-y.

Cooper, D.M.L., Turinsky, A.L., Sensen, C.W. & Hallgrimsson, B. 2003. Quantitative 3D analysis of the canal network in cortical bone by micro-computed tomography. *Anat Rec B New Anat*. 274(1):169–179. DOI: 10.1002/ar.b.10024.

Cosman, M.N., Sparrow, L.M. & Rolian, C. (in press). Changes in shape and cross-sectional geometry in the tibia of mice selectively bred for increases in relative bone length. *J Anat*. (March, 22):n/a–n/a. DOI: 10.1111/joa.12459.

Cox, P.G. & Jeffery, N. 2011. Reviewing the morphology of the jaw-closing musculature in squirrels, rats, and guinea pigs with contrast-enhanced microCT. *Anat Rec (Hoboken)*. 294(6):915–928. DOI: 10.1002/ar.21381.

Crowder, C. & Stout, S. 2012. *Bone Histology: An Anthropological Perspective*. CRC Press.

Cubo, J., Ponton, F., Laurin, M., de Margerie, E. & Castanet, J. 2005. Phylogenetic signal in bone microstructure of sauropsids. *Syst Biol*. 54(4):562–574. DOI: 10.1080/10635150591003461.

Cubo, J., Legendre, P., de Ricqlès, A., Montes, L., de Margerie, E., Castanet, J. & Desdevises, Y. 2008. Phylogenetic, functional, and structural components of variation in bone growth rate of amniotes. *Evolution & ….* 10(2):217–227. DOI: 10.1111/j.1525-142X.2008.00229.x.

Currey, J.D. 2002. *Bones : structure and mechanics*. Princeton, NJ: Princeton University Press.

Currey, J.D. & Alexander, R.M. 1985. The Thickness of the Walls of Tubular Bones. *Journal of Zoology*. 206(AUG):453–468.

de Boef, M. 2008. Signatures of Flight and Running in bone microstructure: An experimental study in helmeted Guineafowl (Numida meleagris) and applications in the study of the dinosaur-bird transition. V. 28. (no.). JOURNAL OF VERTEBRATE …. 70A. DOI: 10.2307/20490998.

de Boef, M. & Larsson, H.C.E. 2007a. Bone microstructure: quantifying bone vascular orientation. *Canadian Journal of Zoology*. 85(1):63–70. DOI: 10.1139/z06-195.

de Boef, M. & Larsson, H.E. 2007b. Objective Techniques for Measuring Differences in Bone Vascular Orientation and Osteocyte Density. *Microscopy and Microanalysis*. 13(S02). DOI: 10.1017/S1431927607078245.
de Boef, M., Larsson, H. & Horner, J. 2007. Measurements of vasculature in *Tyrannosaurus rex* show a relationship between growth rate and vasculature orientation. V. 27. (no.). 67A.
de Buffrénil, V., Houssaye, A. & Böhme, W. 2008. Bone vascular supply in monitor lizards (Squamata: Varanidae): influence of size, growth, and phylogeny. *J Morphol*. 269(5):533–543. DOI: 10.1002/jmor.10604.
de Margerie, E. 2002. Laminar bone as an adaptation to torsional loads in flapping flight. *J Anat*. 201(6):521–526.
de Margerie, E. & Rakotomanana, L. 2007. In silico adaptation of bone vascular microstructure to biomechanical loading mode. *J Morphol*. 268(12):1065–1065.
de Margerie, E., Robin, J.P., Verrier, D., Cubo, J., Groscolas, R. & Castanet, J. 2004. Assessing a relationship between bone microstructure and growth rate: a fluorescent labelling study in the king penguin chick (*Aptenodytes patagonicus*). *J Exp Biol*. 207:869–879.
de Margerie, E., Sanchez, S., Cubo, J. & Castanet, J. 2005. Torsional resistance as a principal component of the structural design of long bones: comparative multivariate evidence in birds. *Anat Rec*. 282A(1):49–66. DOI: 10.1002/ar.a.20141.
de Margerie, E., Cubo, J. & Castanet, J. 2002. Bone typology and growth rate: testing and quantifying 'Amprino's rule' in the mallard (*Anas platyrhynchos*). *C R Biol*. 325(3):221–230.
de Margerie, E., Tafforeau, P. & Rakotomanana, L. 2006. In silico evolution of functional morphology: A test on bone tissue biomechanics. *J R Soc Interface*. 3(10):679–687. DOI: 10.1098/rsif.2006.0128.
de Ricqlès, A. 1968. Recherches paléohistologiques sur les os longs des tétrapodes I. – Origine du tissu osseux plexiforme des dinosauriens sauropodes. *Annales de paleontologie*. 54:133–145.
de Ricqlès, A. 1969. Recherches paléohistologiques sur les os longs des Tétrapodes II. - Quelques observations sur la structure des os longs des Thériodontes. *Annales de paleontologie*. 55:3–52.
de Ricqlès, A. 1972. Recherches paléohistologiques sur les os longs des tétrapodes III. – Titanosuchiens, dinocéphales et dicynodontes. *Annales de paleontologie*. 58:17–60.
de Ricqlès, A. 1974a. Recherches paléohistologiques sur les os longs des tétrapodes IV. – Eothériodontes et pélycosaures. *Annales de paleontologie*. 60:1–39.
de Ricqlès, A. 1974b. Recherches paléohistologiques sur les os longs des tétrapodes V. – Cotylosaures et mésosaures. *Annales de paleontologie*. 60:171–216.
de Ricqlès, A. 1975. Recherches paléohistologiques sur les os longs des tétrapodes VII. – Sur la classification, la signification fonctionnelle et l'histoire des tissus oseux des tétrapodes. Première partie, structures. *Annales de paleontologie*. 61:51–129.
de Ricqlès, A. 1981. Recherches paléohistologiques sur les os longs des tétrapodes. VI.– Stégocéphales. *Annales de paleontologie*. 67:141–160.

de Ricqlès, A.J., Meunier, F., Castanet, J. & Francillon-Vieillot, H. 1991. Comparative Microstructure of Bone. In *Bone*. V. 3. 1–78.
de Ricqlès, A.J., Padian, K., Horner, J.R. & Francillon-Vieillot, H. 2000. Paleohistology of the bones of pterosaurs (Reptilia: Archosauria): anatomy, ontogeny, and biomechanical implications. *Zoological Journal of the Linnean Society*. 129(3):349–385. DOI: 10.1006/zjls.1999.0239.
Dechow, P.C., Chung, D.H. & Bolouri, M. 2008. Relationship Between Three-Dimensional Microstructure and Elastic Properties of Cortical Bone in the Human Mandible and Femur. In *Primate Craniofacial Function and Biology*. (no.). Boston, MA: Springer US. 265–292. DOI: 10.1007/978-0-387-76585-3_13.
Dehoff, R.T. 1983a. Quantitative Serial Sectioning Analysis - Preview. *J Microsc*. 131(Sep):259–263.
Dehoff, R.T. 1983b. Quantitative serial sectioning analysis: preview. *J Microsc*. 131(3):259–263. DOI: 10.1111/j.1365-2818.1983.tb04254.x.
Enlow, D.H. & Brown, S.O. 1958. A comparative histological study of fossil and recent bone tissues. Part III. *The Texas Journal of Science*.
Erickson, G.M., Rogers, K.C. & Yerby, S.A. 2001. Dinosaurian growth patterns and rapid avian growth rates. *Nature*. 412(6845):429–433. DOI: 10.1038/35086558.
Feldkamp, L.A., Goldstein, S.A., Parfitt, A.M., Jesion, G. & Kleerekoper, M. 1989. The Direct Examination of 3-Dimensional Bone Architecture Invitro by Computed-Tomography. *Journal of bone and Mineral Research*. 4(1):3–11.
Foote, J.S. & Hrdlicka, A. 1916. *A contribution to the comparative histology of the femur*. DOI: 10.5962/bhl.title.83960.
Frost, H.M. 1963. *Bone remodelling dynamics*. Springfield: Thomas.
Gocha, T.P. & Agnew, A.M. (in press). Spatial variation in osteon population density at the human femoral midshaft: histomorphometric adaptations to habitual load environment. *J Anat*. (December, 28):n/a–n/a. DOI: 10.1111/joa.12433.
Hall, B.K. 2005. *Bones and cartilage: developmental and evolutionary skeletal biology*. Academic Press.
Harrison, K.D. & Cooper, D.M.L. 2015. Modalities for Visualization of Cortical Bone Remodeling: The Past, Present, and Future. *Frontiers in endocrinology*. 6(122):109. DOI: 10.3389/fendo.2015.00122.
Hennig, C., Thomas, C.D.L., Clement, J.G. & Cooper, D.M.L. 2015. Does 3D orientation account for variation in osteon morphology assessed by 2D histology? *J Anat*. 227(4):497–505. DOI: 10.1111/joa.12357.
Hert, J., Fiala, P. & Petrtyl, M. 1994. Osteon orientation of the diaphysis of the long bones in man. *Bone*. 15(3):269–277.
Holdsworth, D.W. & Thornton, M.M. 2002. Micro-CT in small animal and specimen imaging. *Trends in Biotechnology*. 20(8):S34–S39. DOI: 10.1016/S0167-7799(02)02004-8.
Hounsfield, G.N. 1973. Computerized transverse axial scanning (tomography). 1. Description of system. *Br J Radiol*. 46(552):1016–1022.
Hunter, J.D. 2007. Matplotlib: A 2D graphics environment. *Computing in Science & Engineering*. 9(3):90–95.

Jast, J. & Jasiuk, I. 2013. Age-related changes in the 3D hierarchical structure of rat tibia cortical bone characterized by high-resolution micro-CT. *J Appl Physiol*. 114(7):923–933. DOI: 10.1152/japplphysiol.00948.2011.

Jepsen, K.J. & Andarawis-Puri, N. 2012. The amount of periosteal apposition required to maintain bone strength during aging depends on adult bone morphology and tissue-modulus degradation rate. *Journal of bone and Mineral Research*. 27(9):1916–1926. DOI: 10.1002/jbmr.1643.

Johnston, J.D., Liao, L., Dolovich, A.T., Leswick, D.A. & Kontulainen, S.A. 2014. Magnetic resonance imaging of bone and muscle traits at the hip: an in vivo precision study. *Journal of musculoskeletal & neuronal interactions*. 14(1):104–110.

Judex, S., Gross, T.S. & Zernicke, R.F. 1997. Strain gradients correlate with sites of exercise-induced bone-forming surfaces in the adult skeleton. *Journal of bone and Mineral Research*. 12(10):1737–1745. DOI: 10.1359/jbmr.1997.12.10.1737.

Kawalilak, C.E., Johnston, J.D., Cooper, D.M.L., Olszynski, W.P. & Kontulainen, S.A. 2016. Role of endocortical contouring methods on precision of HR-pQCT-derived cortical micro-architecture in postmenopausal women and young adults. *Osteoporos Int*. 27(2):789–796. DOI: 10.1007/s00198-015-3262-3.

Kinney, J.H. & Ladd, A.J. 1998. The relationship between three-dimensional connectivity and the elastic properties of trabecular bone. *Journal of bone and Mineral Research*. 13(5):839–845. DOI: 10.1359/jbmr.1998.13.5.839.

Kinney, J.H. & Nichols, M.C. 1992. X-Ray Tomographic Microscopy (Xtm) Using Synchrotron Radiation. *Annual Review of Materials Science*. 22:121–152. DOI: 10.1146/Annurev.Ms.22.080192.001005.

Knowles, T.G., Kestin, S.C., Haslam, S.M., Brown, S.N., Green, L.E., Butterworth, A., Pope, S.J., Pfeiffer, D., et al. 2008. Leg Disorders in Broiler Chickens: Prevalence, Risk Factors and Prevention. *PLoS One*. 3(2). DOI: 10.1371/journal.pone.0001545.

Kuehn, A., Simons, E.L.R., Lee, A.H. & Main, R.P. 2017. The Effect of Growth Rate and Biomechanical Loading on Bone Laminarity in the Emu Hindlimb. *Faseb Journal*. 31(1 Supplement):577.14–577.14. DOI: 10.1096/fj.1530-6860.

Kunz, T.H. & Stern, A.A. 1995. *Maternal investment and post-natal growth in bats*. Symposia of the zoological ….

Lee, A.H. 2004. Histological organization and its relationship to function in the femur of *Alligator mississippiensis*. *J Anat*. 204(3):197–207. DOI: 10.1111/j.0021-8782.2004.00275.x.

Lee, A.H. & Simons, E.L.R. 2015. Wing bone laminarity is not an adaptation for torsional resistance in bats. *PeerJ*. 2015(3):e823. DOI: 10.7717/peerj.823.

Lee, A.H., Huttenlocker, A.K., Padian, K. & Woodward, H.N. 2013. Analysis of Growth Rates. In *Bone Histology of Fossil Tetrapods*. University of California Press. 216–251. DOI: 10.1525/california/9780520273528.003.0008.

Lee, E.J., Luedtke, J.G., Allison, J.L., Arber, C.E., Merriwether, D.A. & Steadman, D.W. 2010. The effects of different maceration techniques on nuclear DNA amplification using human bone. *Journal of Forensic Sciences*. 55(4):1032–1038. DOI: 10.1111/j.1556-4029.2010.01387.x.

Leterrier, C. & Nys, Y. 1992. Composition, cortical structure and mechanical properties of chicken tibiotarsi: Effect of growth rate. *Br Poult Sci*. 33(5):925–939. DOI: 10.1080/00071669208417536.
Lewis, R.A. 2004. Medical phase contrast x-ray imaging: current status and future prospects. *Phys Med Biol*. 49(16):3573–3583.
Lieberman, D.E., Polk, J.D. & Demes, B. 2004. Predicting long bone loading from cross-sectional geometry. *Am J Phys Anthropol*. 123(2):156–171. DOI: 10.1002/ajpa.10316.
Maggiano, C.M. 2012. Making the mold: a microstructural perspective on bone modeling during growth and mechanical adaptation. In *Bone Histology: An Anthropological Perspective*. C. Crowder & S. Stout, Eds. CRC Press. 45–90.
Maggiano, I., Clement, J., Thomas, D., Carter, Y. & Cooper, D. 2015. Synchrotronic three-dimensional reconstruction of cortical bone for analysis of osteonal branching and interconnectivity across age. *Am J Phys Anthropol*. 156:210–211.
Maggiano, I.S., Maggiano, C.M., Clement, J.G., Thomas, C.D.L., Carter, Y. & Cooper, D.M.L. 2016. Three-dimensional reconstruction of Haversian systems in human cortical bone using synchrotron radiation-based micro-CT: morphology and quantification of branching and transverse connections across age. *J Anat*. 228(5):719–732. DOI: 10.1111/joa.12430.
Main, R.P. & Biewener, A.A. 2007. Skeletal strain patterns and growth in the emu hindlimb during ontogeny. *J Exp Biol*. 210(15):2676–2690. DOI: 10.1242/jeb.004580.
Marelli, C.A. & Simons, E.L.R. 2014. Microstructure and Cross-Sectional Shape of Limb Bones in Great Horned Owls and Red-Tailed Hawks: How Do These Features Relate to Differences in Flight and Hunting Behavior? *PLoS One*. 9(8). DOI: 10.1371/journal.pone.0106094.
Martin, R.B. 2007. Targeted bone remodeling involves BMU steering as well as activation. *Bone*. 40(6):1574–1580. DOI: 10.1016/j.bone.2007.02.023.
Matsumoto, T., Yoshino, M., Asano, T., Uesugi, K., Todoh, M. & Tanaka, M. 2006. Monochromatic synchrotron radiation muCT reveals disuse-mediated canal network rarefaction in cortical bone of growing rat tibiae. *Journal of Applied Physiology*. 100(1):274–280. DOI: 10.1152/japplphysiol.00495.2005.
Metscher, B.D. 2009a. MicroCT for comparative morphology: simple staining methods allow high-contrast 3D imaging of diverse non-mineralized animal tissues. *BMC physiology*. 9(1):11. DOI: 10.1186/1472-6793-9-11.
Metscher, B.D. 2009b. MicroCT for developmental biology: a versatile tool for high-contrast 3D imaging at histological resolutions. *Developmental dynamics : an official publication of the American Association of Anatomists*. 238(3):632–640. DOI: 10.1002/dvdy.21857.
Mitchell, J. & van Heteren, A.H. 2015. A literature review of the spatial organization of lamellar bone. *Comptes Rendus Palevol*. DOI: 10.1016/j.crpv.2015.04.007.
Momose, A., Takeda, T. & Itai, Y. 2000. Blood vessels: depiction at phase-contrast X-ray imaging without contrast agents in the mouse and rat-feasibility study. *Radiology*. 217(2):593–596.
Nishiyama, K.K., Macdonald, H.M., Buie, H.R., Hanley, D.A. & Boyd, S.K. 2010. Postmenopausal Women With Osteopenia Have Higher Cortical Porosity and Thinner

Cortices at the Distal Radius and Tibia Than Women With Normal aBMD: An In Vivo HR-pQCT Study. *Journal of bone and Mineral Research*. 25(4):882–890. DOI: 10.1359/jbmr.091020.
Odgaard, A., Andersen, K., Melsen, F. & Gundersen, H.J. 1990. A direct method for fast three-dimensional serial reconstruction. *J Microsc*. 159(Pt 3):335–342.
Paddock, S.W. 2000. Principles and practices of laser scanning confocal microscopy. *Molecular biotechnology*. 16(2):127–149. DOI: 10.1385/MB:16:2:127.
Padian, K. Ed. 2013. *Bone Histology of Fossil Tetrapods*. University of California Press.
Padian, K., Werning, S. & Horner, J.R. 2016. A hypothesis of differential secondary bone formation in dinosaurs. *Comptes Rendus Palevol*. 15(1-2):41–49. DOI: 10.1016/j.crpv.2015.03.002.
Palacio-Mancheno, P.E., Larriera, A.I., Doty, S.B., Cardoso, L. & Fritton, S.P. 2013. 3D Assessment of Cortical Bone Porosity and Tissue Mineral Density Using High-Resolution μCT: Effects of Resolution and Threshold Method. *Journal of bone and Mineral Research*. 29(1):142–150. DOI: 10.1002/jbmr.2012.
Pauwels, E., Van Loo, D., Cornillie, P., Brabant, L. & Van Hoorebeke, L. 2013. An exploratory study of contrast agents for soft tissue visualization by means of high resolution X-ray computed tomography imaging. *J Microsc*. 250(1):21–31. DOI: 10.1111/jmi.12013.
Pearson, O.M. & Lieberman, D.E. 2004. The aging of Wolff's 'law': ontogeny and responses to mechanical loading in cortical bone. *Am J Phys Anthropol*. Suppl 39:63–99. DOI: 10.1002/ajpa.20155.
Pennycuick, C.J. 1967. The strength of the pigeon's wing bones in relation to their function. *Journal of Experimental Biology*.
Petrtyl, M., Hert, J. & Fiala, P. 1996. Spatial organization of the haversian bone in man. *J Biomech*. 29(2):161–169.
Peyrin, F., Salome, M., Cloetens, P., Laval-Jeantet, A.M., Ritman, E. & Ruegsegger, P. 1998. Micro-CT examinations of trabecular bone samples at different resolutions: 14, 7 and 2 micron level. *Technol Health Care*. 6(5-6):391–401.
Peyrin, F., Dong, P., Pacureanu, A. & Langer, M. 2014. Micro- and nano-CT for the study of bone ultrastructure. *Curr Osteoporos Rep*. 12(4):465–474. DOI: 10.1007/s11914-014-0233-0.
Pines, M. & Reshef, R. 2014. Poultry Bone Development and Bone Disorders. In *Sturkie's Avian Physiology: Sixth Edition*. Elsevier. 367–377. DOI: 10.1016/B978-0-12-407160-5.00015-4.
Pratt, I. 2013. In vivo imaging of cortical porosity by synchrotron phase contrast micro computed tomography.
Pratt, I.V. & Cooper, D.M.L. 2017. A method for measuring the three-dimensional orientation of cortical canals with implications for comparative analysis of bone microstructure in vertebrates. *Micron*. 92:32–38. DOI: 10.1016/j.micron.2016.10.006.
Pratt, I.V., Belev, G., Zhu, N., Chapman, L.D. & Cooper, D.M.L. 2015. In vivo imaging of rat cortical bone porosity by synchrotron phase contrast micro computed tomography. *Phys Med Biol*. 60(1):211–232. DOI: 10.1088/0031-9155/60/1/211.

Pratt, I.V., Johnston, J.D., Walker, E. & Cooper, D.M.L. 2018. Interpreting the three-dimensional orientation of vascular canals and cross-sectional geometry of cortical bone in birds and bats. *J Anat*. 14(Pt 5):S13–942. DOI: 10.1111/joa.12803.

Raj, M.T., Prusinkiewicz, M., Cooper, D.M.L., George, B., Webb, M.A. & Boughner, J.C. 2014. Technique: Imaging Earliest Tooth Development in 3D Using a Silver-Based Tissue Contrast Agent. *Anat Rec (Hoboken)*. 297(2):222–233. DOI: 10.1002/ar.22845.

Rawlinson, S.C.F., Murray, D.H., Mosley, J.R., Wright, C.D.P., Bredl, J.C., Saxon, L.K., Loveridge, N., Leterrier, C., et al. 2009. Genetic selection for fast growth generates bone architecture characterised by enhanced periosteal expansion and limited consolidation of the cortices but a diminution in the early responses to mechanical loading. *Bone*. 45(2):357–366. DOI: 10.1016/j.bone.2009.04.243.

Rensberger, J.M. & Watabe, M. 2000. Fine structure of bone in dinosaurs, birds and mammals. *Nature*. 406(6796):619–622. DOI: 10.1038/35020550.

Robling, A.G., Castillo, A.B. & Turner, C.H. 2006. Biomechanical and molecular regulation of bone remodeling. *Annu Rev Biomed Eng*. 8:455–498. DOI: 10.1146/annurev.bioeng.8.061505.095721.

Rothschild, B.M. & Panza, R.K. 2007. Lack of bone stiffness/strength contribution to osteoarthritis—evidence for primary role of cartilage damage. *Rheumatology*. 46(2):246–249. DOI: 10.1093/rheumatology/kel263.

Sanchez, S., Ahlberg, P.E., Trinajstic, K.M., Mirone, A. & Tafforeau, P. 2012. Three-Dimensional Synchrotron Virtual Paleohistology: A New Insight into the World of Fossil Bone Microstructures. *Microscopy and Microanalysis*. 18(5):1095.

Schneider, P., Stauber, M., Voide, R., Stampanoni, M., Donahue, L.R. & Müller, R. 2007. Ultrastructural properties in cortical bone vary greatly in two inbred strains of mice as assessed by synchrotron light based micro- and nano-CT. *Journal of bone and Mineral Research*. 22(10):1557–1570. DOI: 10.1359/jbmr.070703.

Schwean-Lardner, K., Fancher, B.I. & Classen, H.L. 2012. Impact of daylength on the productivity of two commercial broiler strains. *Br Poult Sci*. 53(1):7–18. DOI: 10.1080/00071668.2012.659652.

Seymour, R.S., Smith, S.L., White, C.R., Henderson, D.M. & Schwarz-Wings, D. 2012. Blood flow to long bones indicates activity metabolism in mammals, reptiles and dinosaurs. *Proceedings of the Royal Society B-Biological Sciences*. 279(1728):451–456. DOI: 10.1098/rspb.2011.0968.

Shaw, C.N. & Stock, J.T. 2009. Habitual throwing and swimming correspond with upper limb diaphyseal strength and shape in modern human athletes. *Am J Phys Anthropol*. 140(1):160–172.

Shim, M.Y., Karnuah, A.B., Mitchell, A.D., Anthony, N.B., Pesti, G.M. & Aggrey, S.E. 2012. The effects of growth rate on leg morphology and tibia breaking strength, mineral density, mineral content, and bone ash in broilers. *Poultry Science*. 91(8):1790–1795. DOI: 10.3382/ps.2011-01968.

Sievänen, H., Karstila, T., Apuli, P. & Kannus, P. 2016. Magnetic resonance imaging of the femoral neck cortex. *Acta Radiologica*. 48(3):308–314. DOI: 10.1080/02841850601182147.

Simons, E.L.R. & O'Connor, P.M. 2012. Bone laminarity in the avian forelimb skeleton and its relationship to flight mode: testing functional interpretations. *Anat Rec (Hoboken)*. 295(3):386–396. DOI: 10.1002/ar.22402.

Skedros, J.G. & Hunt, K.J. 2004. Does the degree of laminarity correlate with site-specific differences in collagen fibre orientation in primary bone? An evaluation in the turkey ulna diaphysis. *J Anat*. 205(2):121–134. DOI: 10.1111/j.0021-8782.2004.00318.x.

Snigirev, A., Snigireva, I., Kohn, V., Kuznetsov, S. & Schelokov, I. 1995. On the possibilities of x-ray phase contrast microimaging by coherent high-energy synchrotron radiation. *Review of Scientific Instruments*. 66(12):5486–5492.

Starck, J.M. & Chinsamy, A. 2002. Bone microstructure and developmental plasticity in birds and other dinosaurs. *J Morphol*. 254(3):232–246. DOI: 10.1002/jmor.10029.

Steadman, D.W., DiAntonio, L.L., Wilson, J.J., Sheridan, K.E. & Tammariello, S.P. 2006. The effects of chemical and heat maceration techniques on the recovery of nuclear and mitochondrial DNA from bone. *Journal of Forensic Sciences*. 51(1):11–17. DOI: 10.1111/j.1556-4029.2005.00001.x.

Stout, S.D., Brunsden, B.S., Hildebolt, C.F., Commean, P.K., Smith, K.E. & Tappen, N.C. 1999. Computer-assisted 3D reconstruction of serial sections of cortical bone to determine the 3D structure of osteons. *Calcif Tissue Int*. 65(4):280–284. DOI: 10.1007/s002239900699.

Swartz, S.M., Bennett, M.B. & Carrier, D.R. 1992. Wing bone stresses in free flying bats and the evolution of skeletal design for flight.

Tafforeau, P., Boistel, R., Boller, E., Bravin, A., Brunet, M., Chaimanee, Y., Cloetens, P., Feist, M., et al. 2006. Applications of X-ray synchrotron microtomography for non-destructive 3D studies of paleontological specimens. *Applied Physics a-Materials Science & Processing*. 83(2):195–202. DOI: 10.1007/S00339-006-3507-2.

Tappen, N.C. 1977. Three-dimensional studies on resorption spaces and developing osteons. *The American journal of anatomy*. 149(3):301–317. DOI: 10.1002/aja.1001490302.

Turner, C.H. & Burr, D.B. 1993. Basic biomechanical measurements of bone: a tutorial. *Bone*. 14(4):595–608.

van Hove, R.P., Nolte, P.A., Vatsa, A., Semeins, C.M., Salmon, P.L., Smit, T.H. & Klein-Nulend, J. 2009. Osteocyte morphology in human tibiae of different bone pathologies with different bone mineral density - Is there a role for mechanosensing? *Bone*. 45(2):321–329. DOI: 10.1016/j.bone.2009.04.238.

Vilayphiou, N., Boutroy, S., Sornay-Rendu, E., Van Rietbergen, B. & Chapurlat, R. 2016. Age-related changes in bone strength from HR-pQCT derived microarchitectural parameters with an emphasis on the role of cortical porosity. *Bone*. 83:233–240. DOI: 10.1016/j.bone.2015.10.012.

Weinstein, R.S., Jilka, R.L., Almeida, M., Roberson, P.K. & Manolagas, S.C. 2011. Intermittent Parathyroid Hormone Administration Counteracts the Adverse Effects of Glucocorticoids on Osteoblast and Osteocyte Viability, Bone Formation, and Strength in Mice. *Endocrinology*. 151(6):2641–2649. DOI: 10.1210/en.2009-1488.

Wilkins, S.W., Gureyev, T.E., Gao, D., Pogany, A. & Stevenson, A.W. 1996. Phase-contrast imaging using polychromatic hard X-rays. *Nature*. 384(6607):335–338.

Williams, B., Solomon, S., Waddington, D., Thorp, B. & Farquharson, C. 2000. Skeletal development in the meat-type chicken. *Br Poult Sci*. 41(2):141–149. DOI: 10.1080/713654918.

Williams, B., Waddington, D., Murray, D.H. & Farquharson, C. 2004. Bone strength during growth: influence of growth rate on cortical porosity and mineralization. *Calcif Tissue Int*. 74(3):236–245. DOI: 10.1007/s00223-002-2124-0.

Witten, P.E. & Huysseune, A. 2009. A comparative view on mechanisms and functions of skeletal remodelling in teleost fish, with special emphasis on osteoclasts and their function. *Biological Reviews*. 84(2):315–346. DOI: 10.1111/j.1469-185X.2009.00077.x.

Wysokinski, T.W., Chapman, D., Adams, G., Renier, M., Suortti, P. & Thomlinson, W. 2007. Beamlines of the biomedical imaging and therapy facility at the Canadian light source—Part 1. *Nuclear Instruments & Methods in Physics Research Section a-Accelerators Spectrometers Detectors and Associated Equipment*. 582(1):73–76. DOI: 10.1016/j.nima.2007.08.087.

Wysokinski, T.W., Chapman, D., Adams, G., Renier, M., Suortti, P. & Thomlinson, W. 2015. Beamlines of the biomedical imaging and therapy facility at the Canadian light source – part 3. *Nuclear Instruments & Methods in Physics Research Section a-Accelerators Spectrometers Detectors and Associated Equipment*. 775:1–4. DOI: 10.1016/j.nima.2014.11.088.

Yeni, Y.N. & Norman, T.L. 2000. Fracture toughness of human femoral neck: effect of microstructure, composition, and age. *Bone*. 26(5):499–504. DOI: 10.1016/S8756-3282(00)00258-1.

Zebaze, R., Ghasem-Zadeh, A., Mbala, A. & Seeman, E. 2013. A new method of segmentation of compact-appearing, transitional and trabecular compartments and quantification of cortical porosity from high resolution peripheral quantitative computed tomographic images. *Bone*. 54(1):8–20. DOI: 10.1016/j.bone.2013.01.007.

Zebaze, R.M.D., Ghasem-Zadeh, A., Bohte, A., Iuliano-Burns, S., Mirams, M., Price, R.I., Mackie, E.J. & Seeman, E. 2010. Intracortical remodelling and porosity in the distal radius and post-mortem femurs of women: a cross-sectional study. *The Lancet*. 375(9727):1729–1736. DOI: 10.1016/S0140-6736(10)60320-0.

Zebaze, R.M.D., Jones, A., Welsh, F., Knackstedt, M. & Seeman, E. 2005. Femoral neck shape and the spatial distribution of its mineral mass varies with its size: Clinical and biomechanical implications. *Bone*. 37(2):243–252. DOI: 10.1016/j.bone.2005.03.019.

Zhou, S.A. & Brahme, A. 2008. Development of phase-contrast X-ray imaging techniques and potential medical applications. *Phys Med*. 24(3):129–148. DOI: 10.1016/j.ejmp.2008.05.006.

Appendix

Permission for Chapter 2, reprinted from: Pratt, I.V. & Cooper, D.M.L., 2017. A method for measuring the three-dimensional orientation of cortical canals with implications for comparative analysis of bone microstructure in vertebrates. Micron, 92, pp.32–38.

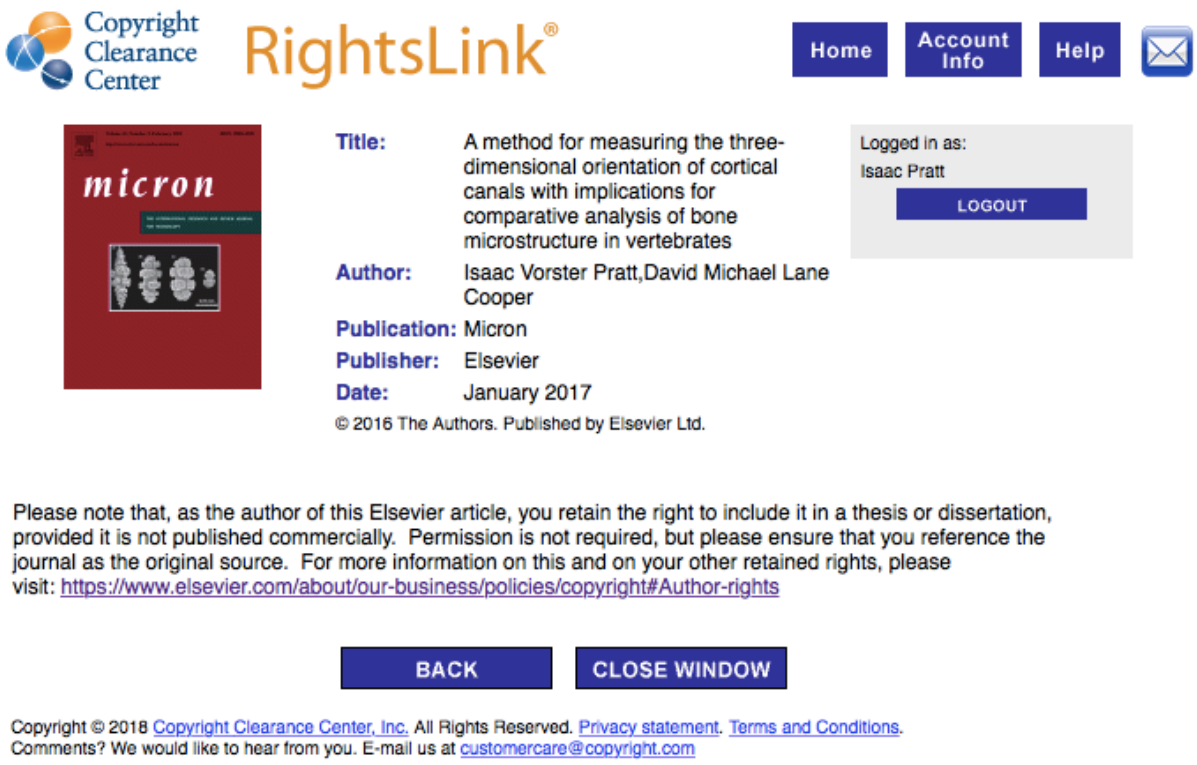

Copyright Clearance Center RightsLink®

Home | Account Info | Help

Title: A method for measuring the three-dimensional orientation of cortical canals with implications for comparative analysis of bone microstructure in vertebrates

Author: Isaac Vorster Pratt,David Michael Lane Cooper

Publication: Micron

Publisher: Elsevier

Date: January 2017

Logged in as:
Isaac Pratt
LOGOUT

BACK | CLOSE WINDOW

Permission for Chapter 3, reprinted from: Pratt, I.V. et al., 2018. Interpreting the three-dimensional orientation of vascular canals and cross-sectional geometry of cortical bone in birds and bats. J Anat, 14(Pt 5), p.S13.

JOHN WILEY AND SONS LICENSE TERMS AND CONDITIONS

Jun 11, 2018

This Agreement between Mr. Isaac Pratt ("You") and John Wiley and Sons ("John Wiley and Sons") consists of your license details and the terms and conditions provided by John Wiley and Sons and Copyright Clearance Center.

License Number	4366031390558
License date	Jun 11, 2018
Licensed Content Publisher	John Wiley and Sons
Licensed Content Publication	Journal of Anatomy
Licensed Content Title	Interpreting the three-dimensional orientation of vascular canals and cross-sectional geometry of cortical bone in birds and bats
Licensed Content Author	Isaac V. Pratt, James D. Johnston, Ernie Walker, et al
Licensed Content Date	Mar 8, 2018
Licensed Content Volume	232
Licensed Content Issue	6
Licensed Content Pages	12
Type of use	Dissertation/Thesis
Requestor type	Author of this Wiley article
Format	Print and electronic
Portion	Full article
Will you be translating?	No
Title of your thesis / dissertation	Interpreting the 3D orientation of vascular canals in cortical bone in birds and bats
Expected completion date	Jul 2018
Expected size (number of pages)	150
Requestor Location	Mr. Isaac Pratt Health Sciences Building 107 Wiggins Road Sasakatoon, SK S7N5E5 Canada Attn: Mr. Isaac Pratt
Publisher Tax ID	EU826007151
Total	0.00 CAD
Terms and Conditions	

TERMS AND CONDITIONS

This copyrighted material is owned by or exclusively licensed to John Wiley & Sons, Inc. or one of its group companies (each a"Wiley Company") or handled on behalf of a society with which a Wiley Company has exclusive publishing rights in relation to a particular work (collectively "WILEY"). By clicking "accept" in connection with completing this licensing

Permission for Chapter 4, reprinted from: Pratt, I.V. and Cooper, D.M.L., 2018. The effect of growth rate on the three-dimensional orientation of vascular canals in the cortical bone of broiler chickens. J Anat. doi:10.1111/joa.12847

Copyright Clearance Center RightsLink®

Home | Account Info | Help

Title: The effect of growth rate on the three-dimensional orientation of vascular canals in the cortical bone of broiler chickens

Author: Isaac V. Pratt, David M. L. Cooper

Publication: Journal of Anatomy

Publisher: John Wiley and Sons

Date: Jul 18, 2018

Copyright © 2018, John Wiley and Sons

Logged in as:
Isaac Pratt
Account #:

LOGOUT

Open Access Article

This article is available under the terms of the Creative Commons Attribution Non-Commercial No Derivatives License CC BY-NC-ND (which may be updated from time to time) and permits **non-commercial** use, distribution, and reproduction in any medium, without alteration, provided the original work is properly cited and it is reproduced verbatim.

For an understanding of what is meant by the terms of the Creative Commons License, please refer to Wiley's Open Access Terms and Conditions.

Permission is not required for **non-commercial** reuse. For **commercial** reuse, please hit the "back" button and select the most appropriate **commercial** requestor type before completing your order.

If you wish to adapt, alter, translate or create any other derivative work from this article, permission must be sought from the Publisher. Please email your requirements to RightsLink@wiley.com.